Mineralogy, Petrography and Gold Distribution at the Twin Hills, Epithermal Deposit North-Central Queensland, Australia

Adam Jones

A1215041

Supervisor: Dr. Nigel Cook

Co-supervisor: Dr. Cristiana Ciobanu

CONTENTS

ABSTRACT

The Twin Hills epithermal system is located 250 km south of Charters Towers, Central North Queensland within the Drummond Basin. Mineralisation is hosted within a half graben, filled with hydrothermal vent breccia containing lithological clasts from multiple sources, which have undergone silicification and pyritisation. The deposit features characteristic sub-low temperature, low-sulphidation mineralisation, classified as adularia-sericite type. Chalcedony quartz and later comb quartz/fluorite veins host the precious metal mineralisation. Textures within the quartz suggest that boiling was the main mechanism for the co-precipitation of gold with pyrite. The latter is a key mineral in tracing precious metal distribution in the deposit.

Scanning electron microscope (SEM), electron microprobe analysis (EPMA) and laser ablation-inductively coupled mass spectrometry (LA-ICPMS) have been used to identify three main morphological-geochemical groups of pyrite at Twin Hills. Each can be linked to one of three distinct genetic stages: (1) early, largely biogenic pyrite formed in an euxinic sinter environment overlying the main ore system, and which carries high amounts of Au, Ag, As, Sb, Mo and Tl; (2) main-stage pyrite, characterised by milling, resorbtion and overgrowth in which two sub-stages-each representing distinct fluid pulses are recognised [(a) enrichment in Au-(As) and (b) enrichment in Ag-(Se)]; and (3) late-stage pyrite containing low contents of most trace elements formed in a phreatic phase after collapse of the sub-basin and which involved fluid mixing.

Twin Hills pyrite hosts significant amounts of refractory ‘invisible’ gold, both as lattice-bound gold and as gold nanoparticles. Concentrations of several tens of ppm Au were measured in early- and main-stage pyrite. Electrum is, however, the main gold mineral in the deposit; it may, however, be Ag-rich and thus slow-leaching. High-grade *‘ginguro’* mineralisation at Twin Hills is characterised by abundant naumannite (Ag_2Se), which may contribute, alongside electrum and invisible silver in pyrite, to the overall silver balance.

The presence of enhanced concentrations of Sb, As, Tl and Mo in the pyrite formed in a euxinic sinter environments suggests that these may be viable pathfinder elements in future exploration for other possible hydrothermal outflow zones in areas of shallow cover.

1. INTRODUCTION

The Twin Hills (309) Au-Ag epithermal deposit lies against the far western boundary of the Drummond Basin in central northern Queensland, Australia. The Drummond Basin hosts a number of small-to medium-sized Au-Ag epithermal deposits. Twin Hills (309) is no exception in that it consists of typical epithermal Au-Ag ores in which gold occurs principally as electrum. The deposit is, however, substantially different to the other epithermal deposits in the belt with respect to its host lithology. The Twin Hill deposit is hosted within a phreatic/phreomagmatic hydrothermal breccia situated in a small extensional sub-basin setting (Sennit 1991, Dale 2009). Other Drummond Basin deposits are situated within local andesites (Pajingo) or within strike slip displacements, (Wirralee, Yandon). The nature of the host breccia has led to specific epithermal quartz textures showing mineralisation to be characterised by low sulfidation adularia-sericitic type (Corbett 2006a).

The sinters at the Twin Hills 309 deposit, along with those in the nearby Lone Sister deposit, were originally discovered and drilled by the company Metana in 1987. Procurement of the discovery by private investors scaled up the resource and it was sold to Battle Mountain Australia (BMA) in 2004. In 2006 BMA developed the deposit by access via a decline. Subsequent small-scale mining produced 22,000 ozs Au during 2006 (Goode 2009), after which mining ceased. The current tenement holder North Queensland Metals (NGM), in a 60-40% share arrangement with Heemskirk, took over the Twin Hills venture in mid-2009. NQM has recently undertaken an exploration drilling program to expand the resource and to prove the reinterpreted ramp and vertical veining mineralisation. The possibility of mining the 309 orebody as an open cut is currently being evaluated.

Grades from the Twin Hills 309 ore zones are highly variable. Some metallurgical tests (Harrison 2009) have shown that possible variations in grades and precious metal recoveries may be due to fine gold in silicates, slow leaching caused by silver-rich electrum, minor refractory sulphides and carbonaceous content within the ore (Harrison 2009). Variations in the recovery have direct influence on the feasibility of economical returns for the proposed operations.

The present study investigates ores and the host sequence to determine the mineralogical and geochemical character of the mineralisation and the associated alteration. Emphasis has been placed on the speciation, textures and distribution of precious metals at Twin Hills, with particular attention given to pyrite as both an indicator for the genetic conditions, and as a potentially significant gold carrier. In an epithermal system, gold can be carried as nanoparticles or as invisible gold within the pyrite (Pals *et al.* 2003, Müller *et al.* 2001). Invisible gold is defined as the refractory, 'locked up' gold present within the sulphides developed in an ore-precipitating environment, and may lead to losses in recovery, and thus revenue when exploiting the deposit. Invisible gold can only be detected by microanalysis. In comparable deposits, invisible gold has been demonstrated to contribute considerably to the gold balance (Harris 1990; Ashley *et al*. 2000). The possible implications which invisible gold has for gold recovery warrant the investigation of this problem prior to a resumption of exploitation at the Twin Hills 309 mine. Furthermore, Twin Hills is a relatively Ag-rich deposit, yet little is previously known about the mineralogical speciation of silver in the deposit. In the present contribution, a combination of SEM, EPMA and LAICPMS techniques were used to elucidate an ore-forming model for the Twin Hills 309 epithermal system, establishing any differences with other deposits in the Drummond Basin, and also contributing to a spatial-genetic model for the deposit.

2. GEOLOGY OF THE TWIN HILLS 309 DEPOSIT

2.1 Regional Geology

The Twin Hills 309 epithermal deposit is located within the North West-trending upper Devonian to lower Carboniferous Drummond Basin (Fig. 1). The sediments that make up the Drummond Basin have been subdivided into three cycles of sedimentation (Olgers 1972).

Cycle One consists of coarse intermediate to felsic volcanics and intrusive rocks with a possible mix of coarse terrestrial sediments. These are locally derived from ancient volcanic eruptive centres, producing small localised sub-basins. Formations within the cycle one sedimentation include the Silver Hills Formation, St. Annes Formation, Mount Wyatt Formation and the Bimurra Volcanics.

Cycle Two is associated with basin subsidence resulted in the deposition of related fluvial sandstone and conglomerate facies.

During **Cycle Three**, the basin was eventually filled with mature fluvial sediments. Late Carboniferous ignimbrite sheets covered these fluvial sediments as the basin shallowed upwards.

Felsic to intermediate igneous dykes of Permian age intrude these Drummond Basin sequences.

Most of the precious metal epithermal deposits lying within the Drummond Basin are hosted by cycle one lithologies. (Fig. 1). Pajingo, also operated by NQM is the most significant epithermal deposit in the Drummond Basin. Pajingo is hosted within local andesites, with ginguro style mineralised veining similar in style to Hishikari, Japan (Izawa *et al.* 1990). Current resources for Pajingo stand at 320,000 ozs of gold (Goode 2009). Smaller epithermal deposits which have amounted to some historical production within the Drummond Basin include Yandon and Mount Coolan (Vigar 2007). These deposits are situated within jogs and offsets at reactivated east-west to east-north east transfer faults.

2.2 **Deposit Geology**

Mapping and interpretation of the surrounding surface geology and lithology (Fig. 3) of the 309 deposit has been established by Sennit (Sennit 1991). Subsequent geological reports have been adding on this data ever since. The 309 deposit is essentially hosted within a hydrothermal vent breccia that has been interpreted to be sitting within a local pull-apart basin (Fig. 2). The basin has formed as a result of movement within a sinstral wrenching of two fault-bounding structures (Dale 2009). Evidence for subsidence in the basin has been taken from lithological marker beds below and adjacent to the basin. The breccia host within the basin covers an area at least 300 x 300 metres. Clasts within the breccia vary from clast-supported angular clasts to well-rounded matrix-supported clasts. The clasts represent multiple phases of adjacent sedimentary sequences to the basin and clasts of previous breccias. It is common to see at least two previous breccias within the host breccia. Milling of the breccia is thought to represent proximity to gaseous vents (Dale 2009).

Sennit (1991) recognized 3 main local faults, F1 which forms the western margin of the Twin Hills sub-basin dipping 70° East. F2 is a reverse fault dipping 70°NW and terminates at the intersection with F1. F2 is believed to be the major structurally controlling factor in the genesis of the 309 epithermal deposit. F3 is inferred to trend NNW with a dip of 70°SW. The Twin Hills deposit is hosted within a local antiform. The deposit has been currently divided into three main areas (Fig 2, inset), based on resource calculations and mineralisation controls interpreted by BMA geologists (Dale 2009). NQM has recently reviewed these areas and modified them accordingly. **Area 1** is interpreted as a high-grade SW-dipping flat lode. Vertical feeder vein structures have overprinted and redistributed ore fluids and are thought to be responsible for the bonanza high grade

Au-Ag values in upper zones of area 1. This vertical feeder vein feature is believed to be structurally represented by a pipe-like corridor that is being feed by mineralisation from area 3 below. It was the basis of this hypothesis that the drill holes used for sampling for this present study were to confirm. The drilling concluded that mineralisation was dominated by structurally-flat veins. The superimposed steep veins upon these flat veins were found to be not consistent in redistributing Au-Ag mineralisation throughout the flat veins. It is has been further hypothesised that later dissolutional events may have remobilised the Au-Ag. **Area 2** consists of a series of ramp/relay silica veins rarely exceeding 15 cm in width. Local dilational sites have formed anastomosing quartz veins and stockworks with hydrothermal breccias not exceeding 20 cm in size. These ramp vein sets are orientated in an east to west strike. **Area 3** is also a series of flat, moderate to high grade veins within a broader vertical stockwork pipe. Vertical veinlets are believed to dip towards some feeder zone for this mineralisation.

Ore formation models for the Twin Hills (309) epithermal system have been proposed by Sennit (1991), Bird (2003) and Corbett (2006a, 2006b). All these authors have agreed that the driving force behind the epithermal fluids responsible for mineralisation was a deep magmatic source, which developed subsequent to development of the Twin Hills sub-basin. This sub-basin is believed to have allowed small pulses of felsic magmatic fluids to rise along faults in a half-graben setting. The rising fluids have silicified the hydrothermal vent breccia host, causing it to become structurally brittle, thus providing the perfect dilational site for the following epithermal fluids. Sennit (1991) used fluid inclusion studies to conclude that these epithermal fluids were dominantly meteoric, low salinity fluids and developed in an environment less than 350 °C.

The intriguing factor in the Twin Hills deposit is the development of its mineralisation and the associated factors contributing to electrum deposition. It has been noted that Au-Ag grade has been associated with the following textures (Corbett 2006a, 2006b, Dale 2009).

1) Crystalline quartz with Au-Ag at its margins.
2) Au-Ag precipitation at the centres of comb quartz infills.
3) Au-Ag at the intersection of veins and styolites.
4) Au-Ag precipitation at the vein wall contact with carbonaceous sediments.
5) Au-Ag present in distinct black styolitic bands, known as ‘*ginguro*’.

Possible suggestions in response to the above have been:

1) Internal vein pressure, leading to Au-Ag separation to the margins of veins.

2) Fluid chemistry and temperature variables. Rapid changes in pH by the mixing of two different acidic and alkaline fluids can cause gold to drop out of solution (Spycher & Reed 1989)
3) Fluid interaction at vein contacts, rapid changes in pH and temperature, again causing local precipitation of gold to drop out of solution.
4) Chemical reaction with hosting lithologies, where wall rock geochemistry or geochemistry of clasts within the hydrothermal breccia cause fluctuations to the pH conditions of the Au-Ag charged fluids (Bierlein *et al.* 1998).

The mineralisation at Twin Hills is hosted within a range of quartz/chalcedonic silica veins. (Sennit 1991, 1999) stated a distinct range for different quartz textures relative to depth below the sinter level at near surface. Bladed calcite replacement textures with comb quartz are present between 50 and 130 metres below the sinter. Fluorite, with comb quartz, is found at levels between 50 and 150 metres below the sinter. Veins, as packages up 70-100 meters in thickness, dip 35° SW to the N of the F2 fault which they may feed. Dale (2009, 2010) has interpreted these vein packages as flat vein sets (Fig. 5g). The flat vein sets gently dip to the S-SW and are commonly up to 20cm in thickness. They generally consist of an upper cap, underneath which is a quartz matrix breccia with hydrostatic/dissolution textures underneath with steep anastomosing veinlets. A lower cap of quartz is joined to the upper cap by local stress tension release veins. These packages are said to be up to 3 metres thick. A common theme with these mineralised veins is the controlling factor of F2 upon them, which is thought to be acting as a feeder zone to the upper areas of the Twin Hills 309 deposit. Drill cores used for sampling for this thesis were related to testing the gap between these areas and the feeder zone.

Mineralisation at the drill core level was undertaken by Sennit (1991). He proposed a five-stage paragenesis of mineralisation based on core observations and SEM analysis (Fig. 4). His fluid inclusion data confirmed the paragenetic relationship of these features.

Stage one: Styolites that wrap around clast contacts, commonly aligned with bedding planes if present. Organic matter and sulphides are seen to be dissolved by this type of stylolites. The fluid chemistry with these stylolites is believed to be alkaline, sourced from local carbonate rich waters, and thus is in equilibrium with calcite.

Stage two: Carbonate veins commonly forming bladed textures in local dilational sites. Platy calcite often forms in the restricted upflow zones and precipitates with the exsolution of CO_2 gases (Simmons and Christenson 1994).

Stage three: Chalcedonic silica veining which replaces local bladed calcite from stage II. The chalcedony is saturated in silica and is believed to be chemically neutralised by the previous precipitated carbonate resulting in rapid pH changes in the ore fluid. CO_2 and CH_4 inclusions within the comb quartz confirm decarbonation (Sennit 1991).

Stage four: Comb quartz veins and breccias, these commonly fill as vughs within the chalcedonic silica of stage three. Fluorite mineralisation is associated with this stage as infills at selected sites. (Sennit 1991) found fluid inclusion evidence to show fluorite infills with comb quartz were deposited under the highest temperatures recorded at Twin Hills (350 °C), which are not technically in a classical epithermal model. Sennit concluded the fluorine was precipitated following interaction with alkaline waters.

Stage five: Late styolites crosscut all previous four stages. They commonly connect the comb quartz cavities and veins. (Sennit 1991) suggests these late stylolites to be undersaturated in silica and hence have a strong ability to dissolve quartz. With dissolution of quartz demonstrated by de Boer *et al.* (1977) at temperatures around 340 °C, Sennit (1991) concluded that Stage V stylolites closely followed precipitation of fluorite and comb quartz.

Sennit (1991) attributed transport of gold in the Twin Hills hydrothermal system to a deep-sourced fluid, with gold present as chloride- and/or thio-complexes. Early carbonate alteration provided the necessary conditions for silica-saturated fluids to be neutralised causing a change in pH and thus allowing electrum, silver and chalcopyrite to be precipitated. Fluorite fluids derived from deep in the system precipitated with interaction of near surface alkaline waters. Late stage V stylolites formed in response to increasing pressures with the advance of upwelling hydrothermal fluids. The consequent under saturated conditions allowed quartz to be locally dissolved under pressure solution fronts. The resultant pressure release and pH change allowed electrum and sulphides to precipitate. Previously reported ore minerals from the 309 deposit include chalcopyrite, sphalerite, covellite, bornite, native silver and electrum (Sennit 1991).

3. SAMPLING AND ANALYTICAL METHODOLOGY

3.1 Sampling

Drill cores THRCD 917, THRCD 919, THRCD 920, THRCD 921, THRCD 925 and THRCD 926 were logged and sampled during a visit to Twin Hills in April 2010. Field notes and photographs were taken of alteration and mineralisation features within all drill cores. Sampling was particularly focussed on intervals containing visible sulphides as well as on elevated Au grades as determined by NQM assays.

Fifteen samples were taken for whole rock geochemistry and 24 samples were prepared as one-inch polished blocks for microscopic study. Initial reflected light microscopy of the 24 polished blocks identified the main and accessory ore minerals, as well as their relationships with gangue minerals and ore textures. Subsequent to this, scanning electron microscopy in back-scattered image mode (BSE) was used to verify identifications made optically. Pyrite grains were also examined for compositional zonation caused by variation in the content of As or other elements. The study placed emphasis on the precious metals, including compositional trends and size variation among grains of native gold, electrum and Ag-bearing minerals. The study also aimed to identify whether other Au- and Ag-bearing minerals such as Au-(Ag)-tellurides or -sulphosalts might be present, as had been postulated earlier. Selected, well-characterized samples were then analysed further by electron probe microanalyser (EPMA) to quantitatively determine mineral compositions, including varying As content in pyrite. Laser-ablation ICP mass-spectroscopy (LAICPMS) was used to determine the concentrations of trace elements within pyrite of different textural and morphological types. All samples investigated in this study are listed in Table 1 and are indexed with photographs and accompanying schematic drillhole sections in Appendices I and II.

3.2 **Analytical Methodology**

3.2.1 ASSAY

A selection of 15 samples of drillcore were sent for assay (Genanalysis, Adelaide). The following suite of elements were determined: Au, Ag, As, Bi, Co, Cu, Mo, Ni, Pb, Sb, Se, Te and Zn.

3.2.2 OPTICAL MICROSCOPY

A Leitz Laborlux-12-Pol polarizing microscope, operating in reflected light mode and equipped with a digital camera, was used to examine the polished blocks.

3.2.3 SCANNING ELECTRON MICROSCOPY

The Philips XL30 scanning electron microscope (SEM) with energy dispersive X-ray spectrometry (EDAX) and back-scattered electron (BSE) imaging at Adelaide Microscopy was used, operating at 20 eV. Back-scatter imaging coupled with semi-quantitative EDAX facilities allowed rapid identification of trace minerals, resolution of the smallest Au- and Ag-bearing grains (down to 1-2 micron) and identification of the alteration silicates.

3.2.4 ELECTRON MICROPROBE ANALYSIS

The CAMECA SX-51 electron microprobe (EMP) with wavelength dispersion spectrometers at Adelaide Microscopy Centre, University of Adelaide, Australia was used. This provided quantitative compositional data on pyrite (particularly the As content) and various minor minerals including native gold/electrum. Operating conditions were an accelerating voltage of 20 kV and beam current of 19.5 nA. The following X-ray lines and standards were used: Au (Au Mα), Bi_2Se_3 (Bi Mα, Se Lα), PbS (Pb Mα), Ag_2Te (Ag Lα, Te Lα), Sb_2S_3 (Sb Lα), CoAsS (Co Kα, As Lα), Ni (Ni Kα), $CuFeS_2$ (Cu Kα), HgS (Hg Mα) and FeS_2 (Fe Kα, S Kα).

3.2.5 LASER-ABLATION ICP MASS-SPECTROSCOPY

Laser-ablation ICP mass-spectroscopy (LA-ICPMS) analysis of pyrite was made using the Agilent HP7700 Quadripole ICPMS instrument at CODES (University of Tasmania, Hobart, Australia). This instrument is equipped with a high-performance New Wave UP-213 Nd:YAG Q-switched laser-ablation system equipped with MeoLaser 213 software. The laser microprobe was equipped with an in-house small volume (<2.5 cm^3) ablation cell characterized by <1 s response time and <2 s wash-out time. Ablation was performed in an atmosphere of pure He (0.7 l/min). The He gas carrying the ablated aerosol was mixed with Ar (1.23 l/min) immediately after the ablation cell and the mix is passed through a pulse homogenizing device prior to direct introduction into the torch. The ICPMS was optimized daily to maximize sensitivity on mid- to high-mass isotopes (in the range 130–240 a.m.u.). Production of molecular oxide species (i.e., $^{232}Th^{16}O/^{232}Th$) and doubly-charges ion species (i.e., $^{140}Ce^{++}/^{140}Ce^{+}$) was maintained at <0.2%. Due to the low level of molecular oxide and doubly charged ion production, no correction was introduced to the analyte signal intensities for such potential interfering species.

Each analysis was performed in the time-resolved mode, which involves sequential peak hopping through the mass spectrum. The laser system was operated at constant 5 or 10 Hz pulse rate; laser energy was typically 1.5-2.5 J cm^{-2}. At these conditions each pulse removes ~0.3 µm of the samples, resulting in ablation rates of 1.5 µm/s and 3.0 µm/s for 5 and 10 Hz, respectively. Pre-defined areas of the polished blocks were ablated; spot sizes of the analyses were 5 µm in diameter and 10 µm for standards. The following isotopes were monitored: ^{49}Ti, ^{51}V, ^{53}Cr, ^{55}Mn, ^{57}Fe, ^{59}Co, ^{60}Ni, ^{65}Cu, ^{66}Zn, ^{69}Ga, ^{72}Ge, ^{75}As, ^{77}Se, ^{93}Nb, ^{95}Mo, ^{107}Ag, ^{111}Cd, ^{115}In, ^{118}Sn, ^{121}Sb, ^{125}Te, ^{182}W, ^{185}Re, ^{197}Au, ^{205}Tl, ^{208}Pb, ^{209}Bi and ^{238}U. Results are reported in elemental ppm.

Analysis time for each sample was 90 s, comprising a 30-s measurement of background (laser off) and a 70-s analysis with laser-on. Acquisition time for all masses was set to 0.02 s, with a total sweep time of 0.6 s. Data reduction was undertaken according to standard methods, using Fe as the internal standard for pyrite. Calibration was performed using an in-house standard (STDGL2b-2), comprising powdered sulphides doped with certified element solutions and fused to a lithium borate glass disk. This standard is suitable for quantitative analyses in different sulphide matrixes (Danyushevsky *et al*. 2003, in press).

Element mapping was performed using the New Wave UP-213 Laser, coupled to an Agilent HP 4500 Quadropole ICP-MS at CODES. Trace element maps were generated by ablating sets of parallel lines in a grid across the sample. The lines were ablated at a frequency of 10 Hz, with a beam size of 10 ìm, rastering at 10ìm/s. See (Large *et al*. 2009) for further details of the methodology.

4. RESULTS

The deposit description of the Twin Hills 309 ore body was interpreted from the logging results of the six sampled drill cores, in combination with previous consultancy geological reports that exist from previous company reports.

Deposit description is best described from the combination of macroscopic scale descriptions at the drill hole scale, and at the micro-scale by the descriptions made whilst analysing by SEM (EDAX)

4.1 **Mineralogy and Petrography**

A brief outline of lithology and mineralisation with associated veining types from the six sampled diamond drill cores is given below. Representative mineralisation and veining used in discussion is given in (Figs. 5 & 6). Full sample descriptions are given in Appendix I.

THRCD 917

The most prominent lithology making up diamond drill hole THRCD 917 is a matrix-supported pebble hydrothermal vent breccia, dominant between 126-151 metres and again from 155 to 186 metres, which marks the end of the hole (EOH). The two zones of hydrothermal vent breccia are separated by coarse-grained arenites. Pyritisation is disseminated throughout the core. Argillic alteration is present adjacent to comb quartz veining. Samples AJ 52, AJ 54, AJ 55, AJ 56, AJ 59, AJ 60, AJ 61, AJ 62, AJ 63, AJ 64, AJ 65 and AJ 66 are representative from this hole.

THRCD 919

The drill hole lithology of THRCD 919 consists of pebble-sized hydrothermal vent breccia topped by fluidised breccias and fine-grained mudstones. Fine pyrite mineralisation is associated with areas of silicic alteration. Fluorite veins infill anastomosing comb quartz veins. Stylolite veins are also present. These comb quartz veins have steep contacts with each other. The fluorite veins appear as flat vein sets. Samples taken from this hole include AJ 67, AJ 68, AJ 69 and AJ 70.

THRCD 920

Diamond drill hole THRCD 920 consists essentially of three main lithologies. The majority of the drill hole consists of medium to coarse-grained matrix supported hydrothermal vent breccias. Bedded, very fine-grained mudstone is interbedded in packages with the vent breccia throughout the hole, and probably indicates part of the offshore Drummond Basin cycles. The top of this diamond drill hole consist of a phreomagmatic vent breccia. Silicic alteration is pervasive and gives drill core a 'drusy', cloudy appearance. This alteration has had some influence with reacting with the clast edges of the pebbles within the hydrothermal vent breccia. Veining includes hydrothermal crackle quartz infills, mosaic quartz and anastomosing quartz veinlets. Spider veinlets are associated with high molybdenum values. Samples AJ 71, AJ 72, AJ 74, AJ 75 and AJ 76 are from THRCD 920.

THRCD 921

This was the longest drill hole sampled with EOH at 222.53 meters The main mineralisation is hosted in the hydrothermal vent breccia. Intervals of mudstones, fine-grained siltstones and minor airfall volcanics are dominant at the top of the drill hole. Interesting dykes, made up of pebbled breccias, are present, suggesting a proximity to gaseous escape vents within the epithermal system. Chloritic alteration is more prolific in the mudstone units due to the strong aluminous silicate nature of these sediments. Veining is present as comb quartz and hydrothermal crackle breccia infill. Sampling was limited to two samples (AJ 19 and AJ 21).

THRCD 925

The lithology in drill hole THRCD 925 has more variation compared to the other cores, with an approximately 50:50 ratio of hydrothermal vent breccia to mudstones and siltstones. The last section of the drill hole is dominated by hydrothermal vent breccia. Quartz/silica textures are also most variable in this drill hole. Chalcedonic silica, spider veinlets and anastomosing veinlets all being present. Fluorite is a dominate feature with the anastomosing veins. Silica veins are controlled by fractures and bedding, where the fluorite seems to have been the last infill post the silica. Samples from this hole for analysis included AJ 1, AJ 2, AJ 4, AJ 5 AJ 6, AJ 8, AJ 10, AJ 16 and AJ 17.

THRCD 926

Hydrothermal vent breccias once again dominate the majority of the THRCD 926 diamond drill core. Clasts in the breccia range in size up to sub-rounded cobbles. Minor intervening mudstone beds are present. Veining styles are present as anastomosing veins and high-tensile fissure veins with quartz and fluorite infilling fractures in veins with carbonate. High tensile veinlets are noted to be a later event, often faulting the anastomosing veins. The infilling Comb quartz textures with fluorite in dilation sites are suggesting fluorite mineralisation is syn- to post-comb quartz deposition. Samples taken from THRCD 926 include AJ 32, AJ 36a, AJ 36b, AJ 38, AJ 40 and AJ 47.

4.2 Sample petrography

4.2.1 GANGUE MINERALS

Samples analysed have undergone extensive alteration by silicification. Most of the clasts supported within the hydrothermal vent breccia have undergone adularisation to some degree, dependant on their lithology. Fine sandstones, mudstones and tuffs are more prone to fine crystal development throughout. Images have shown that there is a tendency for silicification to proceed after adularia (Fig.7b). Vughs within silica and at clast boundaries have turned to clay minerals (Fig.7e). These are probably illite clays reported to be extensive with minor kaolinite (Brigdon 2006, Corbett 2006a). Apatite has been introduced during the hydrothermal event and is present in veins and as overprinting spots on the host breccia (Fig.7a). Apatite clasts are also shown to be present in the hydrothermal vent breccia, derived from previously brecciated apatite mineralised veins (Fig.7d). Fluorite is commonly associated with hydrothermal crackle breccia infill. There does seem to be a possible connection between fluorite mineralisation and cockscomb quartz infill textures. Pyrite +/- electrum stylolites often overprints fluorite indicating these stylolites to be post-fluorite mineralisation (Fig.7c).

4.2.2 STYLOLITES AND DISTRIBUTION OF ORE TEXTURES

Two subtypes of stylolites have been observed within the representative samples, mineralogy being the common factor for the division of the two sub-types. One stylolite is associated with pyrite +/- electrum mineralisation, whereas the other is associated with carbonaceous matter and TiO_2 minerals.

Samples AJ69, AJ71 and AJ74 show distinct stylolitic bands that are associated with carbonaceous matter and TiO_2 (Fig. 9) Sphalerite was observed to be present in some cases (Fig. 9f). These stylolite bands commonly host very fine-grained pyrite (ranging from 5 µm up to very rare 200 µm in size). The pyrites also often display euhedral faces. Minor chemical zonation was seen in the centre of some of the fine pyrite (Fig. 9g); SEM study reveals this zonation is due to variation in manganese content. The pyrite within these stylolites show brecciation textures (Fig. 9b), and frequently makes up granular aggregates at 'hair-pin' points in the course of the stylolites. Quite often this surrounds the clast margins of occurs parallel to quartz/silica veins.

Stylolites consisting of pyrite and electrum (Fig. 8) were seen in a number of samples, usually with corresponding high Au-grades (Table 1). These stylolites were often seen to overprint all other mineralisation stages and represent some of the last stages in the paragenetic evolution of the 309 deposit. The hydrothermal vent breccia host was seen to have limited control on the course these stylolites followed; clasts were often overprinted. Silica veins do exhibit some control, where different competent lithologies in the silica have altered the course of the stylolites to run parallel to veins. Pyrites ranged in size from 5 to 120 µm in size; and showed no signs of major brecciation. Minor fracturing was noted with porous centres on occasion. Minor arsenopyrite was observed within these stylolites, but was rare. Fluorite mineralisation showed to be pre deposited to stylolites, often in this case the stylolite appears to 'push through and apart' fluorite. (Fig. 8e). Apatite mineralisation seems to have some temporal connection to these stylolites (Fig. 8d) These types of stylolites are best represented in samples AJ6, AJ64 and AJ55.

4.2.3 PYRITE MORPHOLOGY

The morphology of the pyrite within the 309 deposits depends on its location, textural setting and which minerals it is hosted within. Pyrite has precipitated in the hydrothermal vent breccia, often pyritising the portions of certain clasts (Fig 11a). This pyrite is often present as very fine euhedral crystals. It can be said that the majority of the pyrite can be found growing wherever silicic fluids have altered the host rock; this includes the source of the fluids (anastomosing veins, comb quartz veins etc.). The largest pyrites observed occur as granular aggregates, usually along margins of overprinting high-tensile stringer veinlets and anastomosing veinlets (in, for example, sample AJ72). Aggregates were also observed to achieve masses up to 5 mm in size. The smallest pyrite observed were present in the carbonaceous/stylolites and as framboids and 'twins 'in adjacent sediments to veins (sample AJ 1 for example). Pyrite has often replaced organic matter and clasts.

Samples AJ 71, AJ 5 and AJ 72 all show remnants of organic matter. Forms in the shapes of tree seeds and algal matter are preserved by overprinting pyrite (Figs. 10a, b, c). Framboidal clusters are also common with the organic matter. Carbonaceous matter often behaves as nuclei for new pyrite with overgrowth rings (Fig. 10c). The organic matter is probably left over from the collapse of an early-formed sinter. Subsequent milling/brecciation has dispersed the fragments throughout the host rock. 'Bitumen' like looking carbonaceous matter overprints, as a later stage event throughout some samples (AJ 1, AJ 60),(Figs. 10d, e). This material is most likely connected to the disseminated organic matter.

Unique 'twinned 'pyrite crystals are disseminated throughout the sediments adjacent to veins (Figs. 10e, f) in samples AJ 1 and AJ 65. This pyrite is believed to pseudomorph crystals of feldspar in tuffaceous sediments, or adularia.

Two samples (AJ 2 and AJ 4) show pyritisation in two distinct lamellar shapes, sometimes up to 1.5 mm in length (Fig. 11b. The laminated pyrites are associated with haematite, chalcopyrite and tetrahedrite (Fig.11d) The laminations are formed from subeuhedral aggregates of fine-grained pyrite built into long lamellar fibres. The lamellar shapes are probably related to an organic substrate and may have been initially deposited as marcasite, a common feature in brown coal mines (Temple & Delchamps 1953). In the case of AJ 4, the textures look organic-derived (Fig. 10g). The lamellar textures in AJ 2 may be attributed to pyritisation within a mud ball clast that has perhaps slumped into the sediment upon subsidence of the Twin Hills sub-basin.

Most of the pyrite is granular/subhedral in shape. That is to say that some faces of the pyrite display overgrowths of euhedral faces associated with new growth fronts, whereas the outer edges in other parts of the same pyrite grain show no euhedral growth faces. Concentric compositional zonation is common within the subhedral overgrowths. Zonation is most pronounced in pyrite within pyrite +/- electrum stylolites (Fig. 11e, f)and as overgrowths on organic matter. The zonation is caused by variation in arsenic content within each growth stage of the pyrite.

Minor zonation is expressed as cores of Mn-rich pyrite within fine euhedral pyrite of carbonaceous stylolites. Haematite and new subeuhedral pyrite commonly overgrow marcasite fibres, and display elongate, lamellar elongated shapes. Samples AJ 2 and AJ 4 display these characteristics.

4.2.4 GOLD ASSOCIATIONS

The textural habit of gold is present within the 309 deposit is of outmost importance for economical recovery. In the studied samples, three main gold associations were recognised (Fig. 12): combined grains of pyrite and electrum, electrum within the silica gangue, and a characteristic electrum on the rims of naumannite-centred pyrite. Size distribution data are summarised in Table 2.

Pyrite and electrum with minor free arsenopyrite is found to be distributed throughout the stylolitic textures. At the hand-specimen scale, these stylolites seem to coincide to the weak ginguro mineralisation and the late-stage overprinting black stylolitic seams. The electrum is relatively coarse, with a size range from 2 to 50 µm. The gold present in the stylolitic seams is moderately Au-rich electrum, averaging $Au_{0.65-0.68}$ $Ag_{0.32-0.35}$ (see also analytical EPMA data presented below). In most cases, gold is present as free electrum on the rims of granular/subhedral pyrite; electrum enclosed in pyrite was only seen in a few cases.

Electrum is present within a variety of quartz and silica textures. The electrum also displays a wide variety in composition. Electrum associated with chalcedonic silica, often displaying calcite silica replacement textures (Fig. 12d), averages $Au_{0.57-0.65}Ag_{0.35-0.43}$. Quartz infill of secondary breccias and hydrothermal crackle breccias seem to contain electrum with the highest Au content (averaging $Au_{0.68-0.76}Ag_{0.24-0.32}$. The electrum ranges from fine, 5 µm-sized grains to relatively coarse (60 µm) grains (Fig. 12h). Electrum often forms elongated shapes (Fig. 12). Rare sphalerite and fluorite occur within the silica host with some of the free electrum grains.

Naumannite-centred pyrite with electrum rims is associated with the weak *ginguro* mineralisation, especially where chalcedonic silica is present. As a rule, the electrum is present as grains either attached to the rims of the pyrite or in overgrowth phases on the porous naumannite-centred pyrite (Figs. 12a, b, c). The pyrite grains themselves are usually large (up to 200 µm in size) and the electrum is also relatively coarse, ranging from 5 to 60 µm in size. Compositions of electrum in this textural habit are similar to those in the chalcedonic silica bladed calcite-replacement veins.

4.2.5 OTHER SULPHIDES

Sphalerite is the most common base metal sulphides seen in the sample suite. Sphalerite may display a close association with comb quartz textures and apatite (Fig. 13d). It is associated on occasions with pyrite that has been rimmed by electrum. Sphalerite is thus probably related syn-post to the same mineralisation stage as the electrum. (Sennit 1991) indicates that apatite and sphalerite belong to stage IV and stage V mineralisation.

Rare **tetrahedrite** and **chalcopyrite** were found during analysis. The chalcopyrite occurs as very fine grains in sample AJ 2 and AJ 65. These grains are from 5 µm to 120 µm in size (Fig.13g). The chalcopyrite is expressed paragenetically in sample AJ 2 by later sphalerite and tetrahedrite which overprint and rim the chalcopyrite(Figs. 13g,h & Fig. 14a). Interesting bright spots of sub-micron size are seen at the chalcopyrite-tetrahedrite phase boundary(Fig. 13h). These may be inclusions of gold, but this cannot yet be confirmed. Analytical data for tetrahedrite by EPMA is shown below.

Two samples were taken where high molybdenum assays were noted. **Molybdenite** was seen to be situated in the stylolites themselves, often 'flooding' around the pyrite present within them (Fig. 14g). The molybdenite has a 'dirty' appearance; individual fine crystals cannot be recognised and it is assumed that the mineral is microcrystalline. Apatite was observed to be associated with molybdenite in stylolites in sample AJ 16 (Fig. 14c). Molybdenum mineral geochemistry is given below in the section dealing with LA-ICPMS data.

4.2.6 'EXOTIC' MINERAL PHASES

Naumannite, Ag_2Se, is present within samples AJ 55 and AJ 64 (Fig. 5d). As a rule, naumannite is present as blebs and inclusions only with the porous portions of certain pyrite grains. Pyrite hosting the naumannite is quite coarse, sizes up to 200 µm being common in some samples. The porous centre of this pyrite is commonly overgrown by subeuhdral growth faces, associated with As zonation, and with rims of electrum.

Grains of **argyrodite,** ideally Ag_8GeS_6, ranging in size from 10 to 25 µm in size, appear in sample AJ 60. The grains are situated adjacent to the hydrothermal vent breccia footwall within the silica vein (Fig. 13e). Rare grains are associated with pyrite that is less than 10µm in size. SEM imagery and EDAX quantitative data has shown the Ge content varies within the argyrodite and a distinct compositional zonation is recognised in the back-scattered electron images (Fig. 13f)(see below). Rare sphalerite was found to be associated with argyrodite.

4.3 **Whole rock geochemistry**

Original core assays had been taken at regular metre-length intervals by NQM. Sections of drill core showing discernable features were subjected to further assaying. By assaying smaller segments of core which contains major changes in the veining and mineralisation style over the metre interval, it was expected that more subtle geochemical trends could be recognised and if so, they could be correlated with macroscopic features. Reported assays are displayed in Table 3.

Assays showing the highest Au concentrations can be correlated with macroscopic features such as hydrothermal crackle breccias, calcite replacement by chalcedonic silca and stylolites (samples AJ 40, AJ 52, AJ 56 and AJ 63). These samples can be considered as high grade ore, with Au concentrations ranging from 12-20 ppm Au. Macroscopic features such as the hydrothermal vent breccia, stylolites and secondary breccia textures with minimal amounts of quartz contained the lowest Au concentrations, usually <1.5 ppm Au. Interestingly, high As concentrations do not correlate well with high Au values. The most steady and moderate As concentrations seem to be linked to hydrothermal vent breccia host rocks and secondary breccia textures. Selenium is well below detection limit in all samples, except for samples AJ 54 and AJ 56 (2 and 3 ppm Se, respectively). These samples are associated with replacement of bladed calcite by chalcedony and hydrothermal crackle breccias and stylolites. Te was not detected in any samples, coincident with the lack of observed tellurides.

4.4 **Electron Probe Microanalysis**

Quantitative electron probe microanalysis was carried out on grains that had been preselected during the SEM work. Interest was focused on establishing the composition of electrum (Au:Ag ratio), pyrite (range of As values, possible measurable differences in Mn, Co and Ni), tetrahedrite (identifying if this is as a potential Ag-carrier, establishing the Sb/As ratio) and naumannite (potential evidence for Ag_2S-Ag_2Se solid solution). The respective analytical results for pyrite are given in Table 4, for sphalerite/tetrahedrite in Table 5, and for electrum in Table 6.

4.4.1 PYRITE

Arsenic concentration in pyrite is commonly associated with higher concentrations of invisible gold (Cook & Chryssoulis 1990). The EPMA dataset shows that As is present in all analysed pyrite (213 spot analyses). Concentrations range from <0.02 to 3.4 wt.%. The data are summarised in (Table 4) and as histograms in (Fig. 15a, b). The full EPMA dataset is given in Appendix III. There is considerable variation in As content between spots, but the majority of grains have concentrations below 0.02 a.p.f.u. As. On the histograms, there is an interesting small 'spike' of As between 0.05 and 0.06 a.p.f.u. This is more likely due to the analytical bias towards As-rich parts of the pyrite (especially within overgrowth of granular/sub-euhedral pyrite) in the dataset. The data showing variations in As content within pyrite are presented in (Fig. 15b), divided by drill hole in an attempt to understand if there is any systematic variation with lithology. Samples taken from drill hole THRCD 920 show the best spread of As values around the centre of the population. The drill hole showing the lowest As content within pyrite is THRCD 919. This drill hole is, however, only represented by one sample (AJ 69), and thus the data may not be entirely representative of the full range of As content in pyrite throughout the drill hole. Most analytical spots were concentrated within a carbonaceous, rutile-bearing stylolite, suggesting that low As content is a feature of pyrite associated with this type of stylolite. Drill hole THRCD 917 shows a broad range of As content in pyrite. Pyrite analysed from this drill hole is associated with samples that contain free electrum. The largest number of analytical spots in drill hole THRCD 917 was obtained from sample AJ 65. Rare free arsenopyrite grains in AJ 65 were found to be situated about the clusters of pyrite. The full EPMA dataset for sample AJ 65, shows low concentrations of As in the majority of pyrite grains within the clusters (<0.02 wt.% up to 1.1 wt.%).

All pyrite analysed by EPMA have been calculated to 3 atomic proportions per formula unit (FeS_2). We are interested in how the As content influences pyrite stoichiometry. Plotting As against

S (Fig. 15c), showing variations by sample I.D, there is a systematic trend in which S decreases as As content increases. This is seen well in samples AJ 64 and AJ 1 where As approaches 0.1 a.p.f.u.

The analysed pyrite grains contain substantial concentrations of **antimony** with averages of <0.01-0.24 wt.% within individual analysis. In sample AJ 72, Sb reaches 0.5 wt %. Such concentrations are relatively high in comparison with published data. Samples from drill hole THRCD 920 show the highest mean Sb content (Fig. 16e). The correlation between Sb and S (Fig. 16e), suggests that at least a part of this Sb is present in solid solution within pyrite. It can be speculated that Sb enters pyrite in a similar manner to As, which is resembles in terms of ionic state.

The variation in **selenium** content among the analysed pyrite grains is shown in (Fig. 15d, e and Fig. 16a). Pyrite from sample AJ 65 (THRCD 917) contains the most Se-rich pyrite; this drillhole dominates the upper range of concentrations in Fig. 13e. Selenium concentrations in pyrite in AJ 65 are believed to be contributed by the presence of inclusions of naumannite (Ag_2Se), identified in the SEM work (Fig. 12a, b, c). Other samples (AJ 69, AJ 71, AJ 72, AJ 74, AJ 75, AJ 1, AJ 2, AJ 4 and AJ 6, from THRCD 919, THRCD 920 and THRCD 925) contain no detectable Se.

No significant trends are seen in the **copper** content of pyrite over the sampled population (Fig. 16b). Neither was any strong indication of enhanced **manganese** content established, despite the recognition of clear compositional zonation with respect to that element (Fig. 16c).

4.4.2 SPHALERITE AND TETRAHEDRITE

Analytical data for tetrahedrite are restricted to two analytical points from sample AJ 2 (Fig. 13g). These are reported in Table 5. Due to the intergrown nature and size of other tetrahedrite grains, reliable analytical results could not be obtained for them. Formulae calculated for the ideal tetrahedrite $(Cu,Ag)_{10}(Fe,Zn)_2(Sb,As)_4S_{13}$, i.e., based on 29 atoms per formula unit, are also given. Results show the composition $(Cu_{8.60},Ag_{0.01})_{8.61}(Fe_{0.47},Zn_{3.20}Pb_{0.03}Cd_{0.01})_{3.71}(Sb_{2.70},As_{0.71})_{3.41}S_{13}$.

A total of eight sphalerite analytical points are reported in Table 5. Sphalerite occurs as an accessory phase with tetrahedrite which it may postdate (Fig. 13h), and within apatite mineralisation (Fig. 13d). EPMA data gave stoichiometric compositions for the majority of sphalerite: $Zn_{0.90-0.93}Fe_{0.04-0.08}S$, based on 2 a.p.f.u., with only minor Cd present.

4.4.3 GOLD

Analysed compositions of native gold and electrum, as measured by EPMA are summarised in Table 6. A total of twelve analyses over nine different samples and three different drill cores are given. Gold is present as electrum with compositions ranging between 58.0-76.2 wt.% Au and 29.13-43.68 wt % Ag). Copper, Hg, Bi and Te are present, but at very low concentrations around the detection limits. The low Te concentrations are reflected in the whole rock geochemical analysis (Table 3), where Te is below detection limits for assay. The Au/Ag ratio in electrum may increase with depth in that the deepest samples from 168.5 m to 182.3 m in drillhole THRCD 920 show the Au-content of electrum up to 76 wt.% Au. The composition of electrum hosted within chalcedonic silica and associated weak *ginguro* mineralisation (Fig. 5d), however, is closer to $Au_{50}Ag_{50}$ (58.02-64.99 wt.% Au, 35.01-43.68 wt.% Ag). In general, the electrum containing the highest Au/(Ag+Au) ratios are observed in electrum associated with hydrothermal crackle infill breccias and associated stylolites.

4.4.4 ARGYRODITE

A total of 12 semi-quantitative EDAX analyses were made on the argyrodite grains shown in (Fig. 13e) and described above. Element signals for Ge, Se, S, Ag, Sn and Te were measured for a minimum of 55 seconds on the Lα lines (Kα for S). The presence of widespread inclusions and intergrowths with other minerals (sphalerite, Cu-minerals, selenides?) presented difficulties, but four good analyses were nevertheless obtained Table 7. These data shows the presence of both argyrodite and canfieldite, the Ge- and Sn-end-members of the Ag_8GeS_6-Ag_8SnS_6 solid solution series.

4.5 Laser-ablation inductively-coupled mass spectrometry

A total of 127 spot analyses were made on pyrite. Results for elements of interest are summarised in Table 8. In addition, 15 analytical spots were made on molybdenite from a single sample Table 10.

4.5.1 PYRITE

In the majority of most of the samples, the mean **gold** concentration within pyrite is rather constant, typically averaging less than 30 ppm Table 8. The range of concentrations within each sample does, however, show considerable variation from minimum Au concentrations of generally <1 ppm Au up to maximum concentrations that exceed 200 ppm Au. Broadly speaking, there is a positive correlation between the As and Au content of pyrite (Fig. 17a), with samples from drillcores THRCD 920 and THRCD 921 showing this trend clearly. The strong influence of As on Au concentration is seen especially well in the sub-population of pyrite from sample AJ 19.

The As vs. Au plot (Fig. 17a) shows that the majority of data points plot below the gold solubility line of Reich *et al*. (2005), indicating that the gold is likely to reside in solid solution. Pyrite from sample AJ 55, however, as well as some analytical spots from sample AJ 64 plot above the line. These samples contain visible gold as seen under the SEM (Fig. 12c, h) and it can be reasonably assumed that these higher concentrations can be accounted for by nanoparticulate gold. Size variation of gold inclusions probably has a normal distribution, extending down from 1-20 micron range seen under the SEM to the nanoscale.

Silver concentrations, as a whole, range from <1 ppm to > 100,000 ppm. Two sub-populations exist, the lower population ranges from <1ppm to 100 ppm where AJ 72 forms the peak concentration of Ag. The higher population is dominated by samples AJ 55 and AJ 64 with a range from 100-100,000 ppm Ag. (Fig 17b, c) shows the variation in As composition as a function of Ag composition in pyrite. No trends exists to suggest that higher concentrations of As in pyrite correlate with higher Ag values. When divided by sample, (Fig. 17b) it can be clearly seen the higher concentrations of Ag are dominated by samples AJ 55 and AJ 64 which contain naumannite; thus these analytical points have a bias affect on the population.

When Au concentrations in pyrite are plotted against those of Ag (Fig. 18b), two distinct populations can be recognised - characterised by either high or low Ag content. The two elements do not show a good correlation (as is commonly seen in comparable studies). This demonstrates a degree of decoupling between the two elements. This is also evident from the lack of correlation between As and Ag (Fig. 17b). Pyrite from samples AJ 55 and AJ 64 fall into the high Ag-Au category, as might be expected by the presence of naumannite inclusions. A steep linear trend exists within the low-Ag sub-population, showing a greater increase in Au with a relatively much smaller increase in Ag concentration.

Antimony concentrations within the pyrite are high in certain samples (Fig. 17d), in particular sample AJ 72. Concentrations of Sb in pyrite range from <1ppm up to 8,309 ppm or 0.83 wt.%. High Sb ranges like this have been rarely published, although Huston *et al.* (1995) mention concentrations up to 8.6 wt.% Sb. Although Sb concentrations are high in the analysed pyrite, there is no apparent correlation between the As and Sb in the whole dataset. (Fig. 17d, e). Some individual pyrite sub-populations, however, display some positive correlation between the two elements. The time-resolved depth profile for one spot from sample AJ 72 (Fig. 19d) shows the high steady concentrations of Sb may be in solid solution, like As. There is, however, no clear correlation between Sb and Au (Fig. 18c).

Previous SEM imagery has revealed molybdenite to occur within stylolites with associated apatite (Fig. 14c). Apatite is recorded by Sennit (1991) to be one of the last mineralisation events along with electrum, pyrite and sphalerite (Fig. 4). A weak correlation trend exist between Mo and Au (Fig. 18d) if samples AJ 55 and AJ 64 are taken out of the bias. Most concentrations of Mo are low except in sample AJ 72 and AJ 76 where it is present in hundreds ppm. The trend in Mo and As are present. There is, however, a weak positive correlation between Mo and Zn (Fig. 18a) and between Mo and Ag (Fig. 18e). The correlation trend between Mo and Ag becomes more clear if samples AJ 55 and AJ 64 are eliminated; these bias the Ag distribution because of the abundant naumannite inclusions.

Silver and selenium correlate well (Fig. 18g), indicating the role of naumannite inclusions in governing part of the Ag distribution, notably in samples AJ 55 and AJ 64. However, there is marked lack of correlation between Ag and Se for many of the sub-populations for other samples, supporting the conclusion that there are several, independent mechanisms governing Ag distribution within the Twin Hills 309 epithermal system.

Nickel to cobalt range within pyrite in (Fig. 18f) shows all samples have equal concentrations of Ni and Co throughout. Sample AJ 72 has the highest values with 100> ppm. AJ 38 is situated at the bottom end of the trend with only ~10 ppm. High nickel to cobalt concentrations can indicate magmatic influences on the ore fluid (Loftus-Hills & Solomon 1967).

4.5.2 LA-ICPMS SPECTRUM TRENDS

Selected LA-ICPMS time-resolved depth profiles for pyrite are presented in Figs. 19 and 20. The profiles represent a quasi-three-dimensional view of variation in the elements of interest with depth (a few microns). The profiles illustrate certain features within pyrite with respect to ore texture, host and mineralogy.

Two depth profiles representative of pyrite from late stylolites are shown as (Fig. 19a and b). Relatively flat signals for As, Ag and Pb can be seen. The small ‘bumps’ on the profile for As probably correspond to micron-scale As-zonation, a feature characteristic of the pyrite in these stylolites (see Fig. 11e and f). The larger peaks on the As profile may either represent zones of particularly As-rich pyrite, or nanoinclusions of arsenopyrite (Fig. 19b). Gold is present in moderate concentrations within these pyrites. The peaks on the depth profile suggest that at least part of the Au is present as nanoparticles rather than in solid solution.

Lead, Ag, Cu and Sb levels are moderate within this type of pyrite and the small peaks also suggest that these elements are present as mineral inclusions rather than bound in the sulphide lattice. An increase in the line for uranium on (Fig. 19a) may also be attributable to nanoscale mineral inclusions (*marked as U).* Although significant amounts of Se can readily enter the pyrite structure, variation in the Se pattern in pyrite from the stylolites suggests that this element may also be present as mineral inclusions, possibly linked to the marked porosity (Fig. 19a). More homogenous pyrite in the stylolites, i.e., with a less obvious porosity (Fig. 19b) shows Se levels to be present as inclusions.

Zinc also occurs as inclusions (presumably of sphalerite, see (Figs.13a and b) in pyrite of different textural types (e.g., Fig. 19c). Pyrite characteristically carries low concentrations of Zn and is generally a poor host for this element; Zn typically forming sphalerite inclusions.

Silver concentrations are generally like those of Au. Ag is dominantly present as micron-sized and nanoparticles, especially in naumannite-centred pyrite (Fig.20a, b) as would be expected. There is an excellent correlation between the profile pattern for Se and Ag in this type of pyrite.

LA-ICPMS depth profiles from pyrite in sample AJ 72 shows that Sb, Au and Ag are most probably in solid solution. The profiles are flat without peaks to indicate the presence of nanoinclusions (Fig. 19c, d and Fig 20c, d).

4.5.3 LA-ICPMS ELEMENT MAPPING

LA-ICPMS element maps were made of a selected area within sample AJ 72 containing distinctly contrasting pyrite textures. The SEM image of the area reveals two texturally-distinct types of pyrite to be present. One pyrite type is characterised by distinct laminations. Within these laminations there are fibres resembling possible relict marcasite with subsequent overgrowth of subhedral pyrite. The second type of pyrite occurs in the form of the edge of a large mass and exhibits zones marked out by porosity. Both types of pyrite are brecciated to some extent.

Element maps are shown in (Fig. 21) and stress the role that textures play upon element distributions at the grain-scale. There is a good correlation between Ag and Sb throughout both types of pyrite. Gold closely follows suit, but there is a distinct difference, in that Au distribution is enhanced in the porous parts of the large mass of pyrite whereas Ag and Se are not. Even if absolute concentrations are rather low, the higher concentrations of Se, Bi, Hg and to some extent also Cu, are generally restricted to lamellar zones within the laminated pyrite. Arsenic concentrations are greatest within the laminated pyrite; again the maximum concentrations seem to be present in the lamellar zones. Lower As concentrations are noted within the larger pyrite mass. Manganese and Hg concentrations are quite low, reflecting the low values found during spot analysis. Nickel and Co are present throughout both pyrite textures; higher Ni values are restricted to the edge of the large pyrite mass. For these elements too, porosity in the large pyrite mass appears to have some control on the element distributions.

4.5.4 MOLYBDENITE

Fifteen LA-ICPMS spot analyses of molybdenite were made on two grains in sample AJ 16. Results are summarised in Table 9 and given in full in Appendix VI. A feature of the dataset is the significant enrichment in Ag, Sb, Tl, As and Pb (all several thousand ppm in all spots) and more modest enrichment in a range of other elements, including Cu and Se. Although these elements, except Ag, give smooth time-resolved depth profiles (Fig. 22), the enrichments are best interpreted as sub-microscopic inclusions of discrete minerals or, more likely, ultra-fine-grained phases making up the matrix between the individual particles making up the microcrystalline aggregate. Similar 'dirty' molybdenite, often spectacularly enriched in a wide variety of trace elements, has been observed in a number of other deposits of different types (Cook, pers. comm. 2010). The elements W and Re have mean concentrations of 759 and 15 ppm, respectively. These elements are generally considered to be lattice-hosted within molybdenite. Rhenium can be a valuable by-product of molybdenite mining, but concentrations of around 15 ppm are relatively low.

5. DISCUSSION

The present study has focused on understanding the mineralogy, association and distribution of Au and Ag throughout the vent breccia in the Twin Hills deposit. Although rarely exceeding a couple of vol.% in the ore, pyrite is a ubiquitous component of the breccia, as well as in the silica veining. It varies not only with respect to morphology but also in abundance, size and textural relationship with other minerals. By emphasizing how pyrite textures can help understand the architecture of the epithermal system, and correlating these textures with the trace element contents of the pyrite, it is possible to deduce a model for the deposit which also considers deposition mechanisms for the precious metals, the behaviour of related elements such as Se, Sb and As, and also the fluid evolution of the system.

5.1 Pyrite origin: textural and geochemical signatures

The present study has identified various morphological types of pyrite, e.g., framboidal, atoll-like, fine-grained and 'dirty', lamellar, idiomorphic, sub-idiomorphic, etc. (Figs. 10 & 11). These categories are also broadly different in terms of their trace element signatures and relationships with Au mineralisation.

5.1.1 SINTER PYRITE

The organic-like textures (Fig. 10a, b, c) observed in the framboidal/atoll-like pyrite, are clearly indicative of a specific origin/location with respect to the brecciation event(s). The dark cores in the atoll aggregates feature ring-like textures (Fig. 10b) and have been attributed by Sennit (1991), to growth of pyrite around algae nuclei. The latter is characteristic of life form in a shallow hot spring sinter. The framboidal/atoll pyrite also has a pronounced homogeneity in terms of Au concentration (tens of ppm Au) and a distinct character of associated trace elements (Fig. 20d). In particular, it is enriched in Sb (Fig. 17d) and Tl (thousands of ppm). These two elements are commonly associated with crystallisation of pyrite in an euxinic environment. High levels of Sb and As in pyrite are also known to occur around shallow epithermal outflow zones with algal matter (Krupp & Seward 1987).

The dirty, fine-grained pyrite, sometimes with rhythmic/banding textures, is also present in abundance in the same sample as the framboids/atoll-like pyrite. The former has similar geochemistry with that of the framboidal/atoll pyrite and this is clearly apparent in terms of its Au, Ag and Sb content (Fig. 20c). The only marked difference is noted from the results obtained by LA-ICPMS elemental mapping of an area comprising both banded and massive textures. This shows enrichment of As and Se in the banded pyrite (Fig. 21), but a good overlap between Au, Ag and Sb across the two types of pyrite morphology. Both the framboidal and dirty pyrite also represent best examples of pyrite in which trace elements are incorporated in solid solution, as seen from the outstanding flat signals of these elements across the LA-ICPMS depth profiles (Fig. 19d. Fig. 20c, d).

Surprisingly, Mo, commonly considered as a granitophile element, is high (hundreds of ppm) in both the framboidal/atoll-like pyrite and the dirty pyrite throughout the sample, suggesting that this element might of been abundant in the euxinic environment. Such a presumption is backed-up by the fact that the same elements discussed here (Sb, Tl, Ag), are seen in very-high to high concentrations (up to several wt.% for Sb, and hundreds of ppm for Tl and Ag) in the analysed molybdenite. The latter is situated in an adjacent drillcore and at comparable depth with the framboidal pyrite. Strong enrichment of Mo, Sb, Tl, Se, Ag etc. in pyrite is known from black shale deposits formed biogenically in euxinic envinronments (e.g. Orberger *et al.* 2003). Geochemical work on sinters associated with epithermal systems (e.g. Pope *et al*. 2005, Vikre 2007) have shown high to very high concentrations of all these elements, with Tl characteristically present at concentrations of thousands of ppm in bulk samples.

Corroborating all the aspects above, it can be inferred that fragments of the sinter have collapsed and have been incorporated within the black breccia such that the breccia carries a pyrite not only with peculiar morphological aspects but also with a distinct trace element signature. Although the framboidal and atoll-like character is most prominent in such sinter fragments, it is, however, not entirely restricted to them.

A final type of pyrite in the sinter is small (10-15 micron), idiomorphic pyrite with negligible Au (<1 ppm). This texturally-distinct variety is best considered as resulting from the incipient stage of breccia venting.

5.1.2 HYDROTHERMAL AU-BEARING PYRITE OF THE MAIN BRECCIATION STAGES

The pyrite that carries measurable ‘invisible’ Au (from a few ppm up to tens of ppm) and is also seen in direct association with electrum, is typically granular, idiomorphic to sub-idiomorphic in shape and is zoned with respect to As (up to 1 wt.%). Such pyrite is mostly found along stylolites/seams and in the *ginguro*-style mineralisation, as well as in the silica veins. Some of the latter are more complex with respect to crosscutting relationships between silica and fluorite. The sinter pyrites discussed above also contain comparable concentrations of Au.

The *ginguro* pyrite contains some tens of ppm Au. Samples from the same drillcore, 20 m apart, have similar mean values, but the LAICPMS depth profiles for spots in the upper sample (AJ55) showed that Au is present as inclusions (Fig.20b), whereas the corresponding profiles for the lower sample (AJ64) features flat profiles indicating Au in solid solution (Fig. 20a). Some of the highest measured Au concentrations (sample AJ36b) are from stylolitic/seam pyrite, where Au is in solid solution.

The pyrite with the most modest Au content (a few ppm) is from crackle breccia defined by seams of pyrite, electrum, fluorite in a silica matrix. Such masses of silica with crackle appearance are typical of the joints between the vertical and ramp veins (Fig. 5g).

In all samples that contain Au-bearing pyrite (except the sinter), electrum is observed as small inclusions in pyrite and along the same seams that host the pyrite. The relative abundance of the inclusions varies, however, from sample to sample. There is, in general, a greater abundance of inclusions the higher the gold concentration in pyrite. Inclusion density also correlates with the degree of porosity and brecciation. The excellent correlation between Ag and Se (Fig. 18g) reflects an abundance of naumannite inclusions in the chalcedony-hosted *ginguro* mineralisation, in which marginal electrum is also a prominent component. However, there is no overall correlation between Au and Se and the characteristic naumannite-centred pyrite is not especially Au-rich. On the Au-Ag plot (Fig. 18b), the naumannite-centred pyrite forms a distinct cluster. The straightforward inference is that the naumannite-centred pyrite suffered interaction with two generations of Ag-bearing fluids, one producing naumannite inside the pyrite, and the second forming electrum on the pyrite rims.

The fact that high-As does not necessarily imply high Au in the pyrite, e.g. in the crackle breccia (AJ38), is backed up by the lack of direct correlation between Au and As in individual zones. Instead, porosity seems to control gold distribution by creating a mechanism for release of Au from the sulphide and which is re-precipitated as electrum on the pyrite rims. The lack of any systematic relationship between Ag and As (Fig. 17c) further emphasizes that the two elements were likely precipitated from distinct fluids belonging to different stages of ore formation. Abundant electrum is also seen along seams with pyrite that co-exists with arsenopyrite.

The notion of multiple fluids is supported by overgrowth textures in ‘mature’ pyrite. Specifically, initial small, idiomorphic grains of pyrite appear to have grown and interacted with later fluids causing development of porosity, marked compositional zonation, development of overgrowth rims and local brecciation. Development of porosity can also create a mechanism to release gold from the pyrite lattice to be subsequently precipitated on the pyrite rim or at a short distance away in the same seam.

The fine-grained Au-free pyrite in the sinter considered as resulting from incipient breccia venting is a hydrothermal pyrite as much as the others in the paragraphs above, but can be considered as an immature equivalent of the overgrown pyrites in the vent breccia. This hypothesis could be tested by in situ S-isotope analysis to identify magmatic vs. sedimentary/diaganetic/ biogenic fluid signatures.

5.1.3 LATE-STAGE HYDROTHERMAL PYRITE

Some of the larger accumulations of pyrite are seen in hand specimen as mm- to cm-sized lenses and/or thin veinlets crosscutting or weaving along sets of silica stringers in the rock (Fig. 5f). At the microscopic level, this appear as, lamellar, bladed and radial aggregates occurring in a matrix that has a pervasive, fine-grained silica-adularia alteration, probably formed from initial volcanics. The larger masses of pyrite are connected by thin seams with a stylolitic appearance. The presence of Fe-oxides/hydroxides in the adjacent areas may be suggestive of the origin of this pyrite by pseudomorphic replacement of hematite, even though other replacement scenarios might also be possible. The lamellar aggregates have marginal overgrowths of granular pyrite (Fig. 11b). Accumulations of such granular pyrite, alone, are seen along the same vein/seam direction; zonation patterns with respect to As, as well as areas with high porosity are characteristic. Despite the differences in the morphologies, however, both lamellae and granular pyrite are tied together by their location along the same veinlet/seam and are low in As (mean 0.25 wt.%). Similarly, granular pyrites from other samples show weak zonation patterns and variable degrees of porosity and they are also characterised by low As contents (<0.4 wt.%). In some cases, although compositional zonation is observed (Fig. 9g), this is not due to the As content but rather to small and varying concentrations of Mn in the pyrite (<1 wt.%). None of these pyrites were considered for analysis by LA-ICMS because the lack of premise for Au scavenging into pyrite via As incorporation, the paradigm of 'invisible' Au in pyrite (Cook & Chryssoulis, 1990). It is reasonable to presume nonetheless that the Au contents would be negligible or low.

These low-As pyrites are also found along seams containing a dark carbonaceous material, possible bitumen (?). In one of the samples from the top of the system (AJ1), this material is seen infilling grain boundaries instead of seams, suggesting infiltration of bitumen from the top of the basin. This breccia also preserves textures indicating an early pyritisation, as seen from partially-replaced phenocrysts of plagioclase. Adding to the assemblage typifying such pyrites are minerals such as fluorite and apatite, as well as the presence of base metals, i.e., sphalerite, tetrahedrite-tennantite, chalcopyrite and phases from the argyrodite-canfieldite series.

Despite their eclectic character in terms of mineralogical association and textural features, the (i) inferred lack of Au in pyrite, (ii) presence of base-metals, and (iii) direct observation of crosscutting relationships with silica veinlets, are all arguments to consider that this type of pyrite formed during the late (waning) stages of the hydrothermal system.

5.2 **Genetic model**

The Twin Hills epithermal system developed in a half-graben sub-basin bounded by two main faults; F1 (Western Fault) and F2 (Southern Fault). F2 played an important role in controlling the direction of the rising fluids, forming the ramp vein sets described by Dale (2009). The ascending mineralizing fluids were possibly sourced in felsic intrusive, such as the rhyolite in the nearby Lone Sister deposit (6 km to the south) and intruding the St. Annes Formation according to Sennit (1991). Alteration accompanied mineralisation changing the hydrothermal vent breccia host rock to a black mass. The breccia features smaller clasts of intensely-altered volcanic rocks and larger sedimentary clasts from the basin margin within a fluidised matrix. The sinter at the basin paleosurface is also recognised in fragments within the breccia. The dominant alteration is a pervasive silica-adularia assemblage, which is vuggy in places, with bladed calcite replaced by pyrite. A local argillic alteration is also recognised in pockets within the breccia. The contact between the clasts and the matrix is characterised by pressure solution along stylolitic boundaries reflecting inward corrosion of the clasts. The role of stylolites has had little previous recognition in ore genesis. Stylolites are known to form through dissolution of fluid through the porosity of the rock during diagenesis. Reactions between at least two chemical fluids, in disequilibrium with one another, occur at the boundary of two dissimilar lithologies (Park & Schot 1968). Similar processes have surely occurred during late-stage deformation events at Twin Hills. Photography in the field supports evidence for pressure-solution reactions involving clasts and high-tensile veining leading to reduction of host rock material (Figs. 5f and 6b).

High-grade intersections are characterised by massive silica, as veins and pockets, some of which are located at the junctions between the vertical and ramp veins. Crackle breccias occur with these junctions. High-grade ores are also marked by irregular, often weak, black *ginguro* intervals throughout the mass of chalcedonic quartz. *Ginguro* mineralisation is widely described in the literature (e.g., from Pajingo; Corbett 2006a; 2006b) and although definitions vary, the term is applied to dark bands within chalcedonic silica with a characteristic flow pattern and which contain pyrite (± other sulphides), electrum and a range of Ag-minerals, including sulphosalts and, notably naumannite. Exceptionally, *ginguro* at Twin Hills contains mm-scale rims of electrum at the contact between the dark bands and the chalcedony Corbett 2006a). Some authors have explained the textures in *ginguro* in terms of colloidal gold transport within the silica (Saunders 1994). At Twin Hills, fluorite is also an abundant component of the chalcedony-dominated parts of the breccia. Fluid inclusion studies of chalcedony (Sennit 1991) showed evidence of mixing between magmatic-derived and basinal fluids.

Based on results from the present study, several constraints can be made o the evolution of the epithermal system. The sinter was the first expression of the hydrothermal system (note the distinct geochemical signature and morphology of sinter pyrite). Sinter development was partially coeval with vent brecciation underneath, which led to milling, sealing and reworking of the clasts. The evolving history of this hydrothermal venting is recorded in the textural complexity of the 'mature' pyrites along seams and in the *ginguro*. This was coeval with the man phase of mineralisation. Nevertheless, the pyrite records discrete pulses of (i) a Au-As-rich mineralising fluid, and (ii) a later Ag-Se-rich overprinting fluid. The textural and geochemical similarities between the pyrite along the seams in the breccia and in the *ginguro* show that their formation must have been broadly coeval. Differences are due to local lithological inhomogeneities and structural control.

The end-stage of the epithermal system is marked by deposition of barren pyrite, base metal sulphides and of bitumen interstitially within silica-adularia assemblages. It can be inferred that this stage was phreatic in style, involving collapse of the basin and associated flushing of the hydrothermal system by basinal waters. Bitumen infiltration, sinter fragmentation and the aforementioned fluid inclusion data showing mixing are all evidence in support of a phreatic style at the end of the genetic cycle.

Although some genetic relationship between the 309 deposit at Twin Hills and the Lone Sister deposit might be invoked on the basis of their geochemistry, in which the Ag-rich 309 is a distal member of the same mineralising system and the As-rich Lone Sister deposit is proximal, the large distance between them (6 km) makes a direct relationship unlikely. It is perhaps more plausible that an intrusive source is located at depth below 309.

5.3 **Metallurgical considerations for the Twin Hills (309) Deposit**

Various metallurgical tests have previously been undertaken on ores from Twin Hills. Results indicated that oxidised ores provide the best metal recoveries. The presence of organic carbon within the primary ore presents possible preg-robbing issues for CIP leaching methods. Ores containing high silica content also required a minimum grinding size to release free electrum. Refractory ores, such as gold in pyrite and electrum with high silver content, cause slow leaching rates (Harrison 2009). The present study has contributed three sets of new information that have implications for ore processing.

Firstly, refractory sulphides are present within the Twin Hills ore. Microanalysis has shown that both Au and Ag occur within pyrite, both lattice-bound and as discrete particles with sizes of a few microns down to the nanoscale. A good part of the electrum occurring within silica and on the rims of pyrite is likely to be available to common leaching processes, but the size distribution of gold as inclusions will be more problematic. Pre-treatment of these ores would be necessary to achieve a satisfactory recovery of Au. Electrum is observed on the rims of pyrite in late-stage stylolites, on the rims of naummanite-centred pyrite, within weak *ginguro* mineralisation and as free grains in chalcedonic silica. A nugget effect can be expected.

Secondly, although electrum present within late-stage stylolites and as free grains in the chalcedonic silica is notably richer in Au (around $Au_{70-75}Ag_{25-30}$), the electrum in weak *ginguro* mineralisation is Ag-rich (typically $Au_{50}Ag_{50}$). Slower leaching rates would therefore be expected for ores containing chalcedony with *ginguro* mineralisation.

Thirdly, organic carbon is confirmed to be present in at least two situations: disseminated throughout stylolites containing carbonaceous matter and rutile; and also as random microparticles throughout the hydrothermal vent breccia host rock. The source of the carbon within the breccia is believed to be organic matter introduced during collapse of the paleo-sinter. Further reworking of the breccia by localised faulting and late pervasive alteration has disseminated the carbonaceous material within the ore.

6. CONCLUSIONS

- Silicification is the main expression of alteration at Twin Hills, with subordinate adularisation. Intensity of alteration alone only gives a partial indication of high gold grade.

Evidence of fluid boiling is widespread and was probably the main mechanism of gold precipitation.

- Pyrite is an abundant mineral throughout the investigated drill cores from Twin Hills and contains 'invisible gold'. Although pyrite grains are small (rarely exceeding 200 microns), and the mineral rarely exceeds more than a couple of vol.% of any given intersection, the measured Au concentrations of up to several tens of ppm, suggest that this refractory gold must make a significant contribution to the overall gold balance in the deposit.

- Visible gold is essentially electrum, with variable Au:Ag ratio. Some of the electrum grains analysed had compositions towards $Au_{50}Ag_{50}$, confirming earlier work.

- Silver is present as (i) Ag-rich electrum, (ii) in solid solution and as nanoparticles within pyrite, and (iii) as the Ag-selenide naumannite (the latter principally in the *ginguro* mineralisation). The apparent decoupling of Au and Ag in pyrite suggests that there may have been distinct Au-(As) and Ag-(Se) fluid pulses during (the main stage of) ore formation.

- Pyrite is present in a variety of different textures that span the duration of the epithermal system. Comparison of morphologies and trace element concentrations assists construction of a genetic model for the Twin Hills deposit. Three main stages are recognised: early sinter development in an anoxic sub-basin; a main mineralising stage that was coeval with vent breccia development; and a concluding, phreatic stage upon collapse of the sub-basin, causing fluid mixing.

- The pyrite formed under anoxic conditions in the sinter has a characteristic geochemical signature (enriched in Ag, Sb, Tl and Mo), opening up new opportunities for exploration for other paleo-sinters in the area.

Acknowledgements

Angus Netting, Benjamin Wade, Ken Neubauer and John Terlet of Adelaide Microscopy are gratefully acknowledged for their assistance with the analytical work. Leonid Danyshevsky, Sarah Gilbert and Ian Little (CODES, University of Tasmania) are thanked for their helpful assistance with the LA-ICP-MS study. Peter Browne and Brentan Grant (North Queensland Metals) generously contributed ideas, practical assistance and expertise to the project. I thank North Queensland Metals for the opportunity to carry out this project, for their partial sponsorship of the analytical work, logistical support during the site visit, and for the friendly cooperation and interest of NQM personnel. CODES staff will be co-authors in eventual publication of the LA-ICPMS data and element maps. The South Australian Museum (SAM) is gratefully acknowledged for access to microscope facilities.

REFERENCES

ASHLEY P. M. CREAGH & C. J. RYAN C. G. 2000. Invisible gold in ore and mineral concentrates from the Hillgrove gold-antimony deposits, NSW, Australia. *Mineralium Deposita* **35**, 285-301.

BIERLEIN F. P, FULLER T, STÜNE K, ARNE D. C, & KEAYS R. R. 1998. Wallrock alteration associated with turbidite-hosted gold deposits. Examples from the Palaeozoic Lachlan Fold Belt in Central Victoria, Australia. *Ore Geology Reviews* **13**, 345-380.

BIRD M. 2003. 309 Prospect Geological Interpretation, *BMA consultant report* (unpubl).

BRIGDON J. 2006. Hydrothermal Alteration Mineralogy and Trace Element Geochemistry associated with Gold Mineralisation at 309, *BMA consultant report* (unpubl).

COOK N. J & CHRYSSOULIS S. L. 1990. Concentrations of “invisible gold” in the common sulphides. *Canadian Mineralogist* **28**, 1-16.

CORBETT G. 2006a. Comments on Geology and Exploration of the Twin Hills Gold Project, Queensland, Australia, April, *Corbett Geological Services Pty. Ltd* (unpubl).

CORBETT G. 2006b. Comments on Geology and Exploration of the Twin Hills Gold Project, Queensland, Australia, November, *Corbett Geological Services Pty. Ltd* (unpubl).

DALE P. 2009. Geological Report Twin Hills 309 Deposit- submitted in support of resource estimation. *Conglomerate Project Management Pty. Ltd consultant report* (unpubl).

DALE P. 2010. Drilling Report, Twin Hills 309 Deposit, January-March 2010. *Conglomerate Project Management Pty. Ltd consultant report* (unpubl).

DANYUSHEVSKY L. V, ROBINSON P, MCGOLDRICK P, LARGE R. R, & GILBERT S. 2003. LA-ICPMS of Sulphides: evaluation of an XRF glass disc standard for analysis of different sulphide matrixes. *Geochimica et Cosmochimica Acta* **67**, 23.

DANYUSHEVSKY, L.V, ROBINSON P, GILBERT, S, NORMAN, M, LARGE, R, MC-GOLDRICK, P, & SHELLEY, J.M.G., A technique for routine quantitative multi-element analysis of sulphide minerals by laser ablation ICP-MS: *Geochemistry: Exploration, Environment, Analysis* (in press).

DE BOER R. B, NAGTEEGAL P. J. C, & DUYVIS E. M. 1977. Pressure solution experiments on quartz sand. *Geochimica et Cosmochimica Acta* **41**, 257.

GOODE K. 2009. NQM Limited (NQM)- Aiming to Increase Pajingo's Gold operations to >100,000oz pa. *Eagle Research consultant report* (unpubl).

HARRIS D. C. 1990. The Mineralogy of gold and its relevance to gold recoveries. *Mineralium Deposit* **25,** supplement S3-S7.

HARRISON G. 2009. Review of Twin Hills Metallurgical file. Interim report, *NQM consultant report*.

HUSTON D, SIE S. H, SUTER G. F, COOKE D. R, & BOTH R. A. 1995. Trace elements in sulfide minerals from eastern Australian volcanic-hosted massive sulfide deposits; Part I, Proton microprobe analyses of pyrite, chalcopyrite, and sphalerite, and Part II, Selenium levels in pyrite; comparison with delta ^{34} S values and implications for the source of sulfur in volcanogenic hydrothermal systems. *Economic Geology* **90**, 1167-1196.

IZAWA E, URASHIMA Y, IBARAKI K, SUZUKI R, YOKOYAMA T, KAWASAKI K, KOGA A, & TAGUCHI S. 1990. The Hishikari gold deposit: high- grade epithermal veins in Quarternary volcanics of southern Kyushu, Japan. *Journal of Geochemical Exploration* **36**, 1-56.

KRUPP R. E, & SEWARD T. M. 1987. The Rotokawa Geothermal System, New Zealand: An Active Epithermal Gold-Depositing Environment. *Economic Geology* **82**, 1109-1129.

LARGE, R.R., DANYUSHEVSKY, L., HOLLIT, C., MASLENNIKOV, V., MEFFRE, S., GILBERT, S., BULL, S., SCOTT, R., EMSBO, P., THOMAS, H., SINGH, B., FOSTER, J.(2009) Gold and Trace Element

Zonation in Pyrite Using a Laser Imaging Technique: Implications for the Timing of Gold in Orogenic and Carlin-Style Sediment-Hosted Deposits. *Economic Geology* **104**,635-668.

LOFTUS-HILLS G & SOLOMON M. 1967. Cobalt, Nickel and Selenium in Sulphides as Indicatorsof ore Genesis. *Mineralium Deposita* **2**, 228-242.

MÜLLER D, KAMINSKI K, UHLIG S, GRAUPNER T, HERZIG P. M., & HUNT S. 2001. The transition fom porphyry-to epithermal-style gold mineralization at Ladolam, Lihir Island, Papua New Guinea: a reconnaissance study. *Mineralium Deposita* **37**, 61-74.

OLGERS F. 1972. Geology of the Drummond Basin, Queensland. *Bureau of Mineral Resources Bulletin* **130**.

ORBERGER B, PASAVA J, GALLIEN J. P, DAUDIN L., & TROCELLIER P. 2003. Se, As, Mo, Ag, Cd, In, Sd, Pt, Au, Tl, Re traces in biogenic and abiogenic sulphides from Black Shales (Selwyn Basin, Yukon territories, Canada): A nuclear microprobe study. *Nuclear Instruments and Methods in Physics Research* **B 210**, 441-448.

PALS, D. W, SPRY P. G & CHRYSSOULIS S. 2003. Invisible Gold and Tellurium in Arsenic-Rich Pyrite from the Emperor Gold Deposit, Fiji: Implications for Gold Distribution and Deposition. *Economic Geology* **98**, 479-493.

PARK C. W & SCHOT E. H. 1968. Stylolites: Their nature and origin. *Journal of Sedimentary Research* **38**, 175-191.

POPE J. G, BROWN K. L, & MCCONCHIE D. M. 2005. Gold Concentrations in Springs at Waiotapu, New Zealand: Implications for Precious Metal Deposition in Geothermal Systems. *Economic Geology* **100**, 677-687.

REICH M, KESLER S. E, UTSUNOMIYA S, PALENIK C. S, CHRYSSOULIS S. L., & EWING R. C. 2005. Solubility of gold in arsenian pyrite. *Geochimica et Cosmochimica Acta* **69**, 2781-2796.

SAUNDERS J. A. 1990. Colloidal transport of gold and silica in epithermal precious-metal systems: Evidence from the Sleeper deposit, Nevada. *Geology* **18**, 757-760.

SAUNDERS J. A. 1994. Silica and gold textures in bonanza ores of the Sleeper Deposit, Humboldt County, Nevada: Evidence for colloids and implications for epithermal ore-forming processes. *Economic Geology* **89**, 628-638.

SAUNDERS J. A & SCHOENLY P. A. 1995. Boiling colloid nucleation and aggregation, and the genesis of bonanza Au-Ag ores of the Sleeper deposit, Nevada. *MIneralium Deposita* **30**, 199-210.

SENNIT C. M. 1991. Aspects of Epithermal Gold Mineralisation, Twin Hills, Queensland. MSc thesis, James Cook University (unpubl.).

SENNIT C. M. 1999. Structural Controls on Gold Mineralisation at the Twin Hills Project, Drummond Basin, Queensland. *Solid Geology consultant report to Homestake.*

SIMMONS S. F & CHRISTENSON B. W. 1994. Origins of Calcite in a Boiling Geothermal System. *American Journal of Science* **294**, 361-300.

SPYCHER N. F & REED M. H. 1989. Evolution of a broadlands-type epithermal ore fluid along alternative P-T paths; implications for the transport and deposition of base, precious, and volatile metals. *Economic Geology* **84**, 328-359.

TEMPLE K. L & DELCHAMPS E. W. 1953. Autotrophic bacteria and the Formation of Acid in Bituminous Coal Mines. *Applied Microbiology* **1**, 255-258.

VIGAR A. 2007. *Drummond Basin Gold Deposits*. Presentation for Australian Institute of Mining and Metallurgy, Brisbane, Australia.

VIKRE P. G. 2007. Sinter-Vein Correlations at Buckskin Mountain, National District, Humboldt County, Nevada. *Economic Geology* **102**, 193-224.

FIGURES

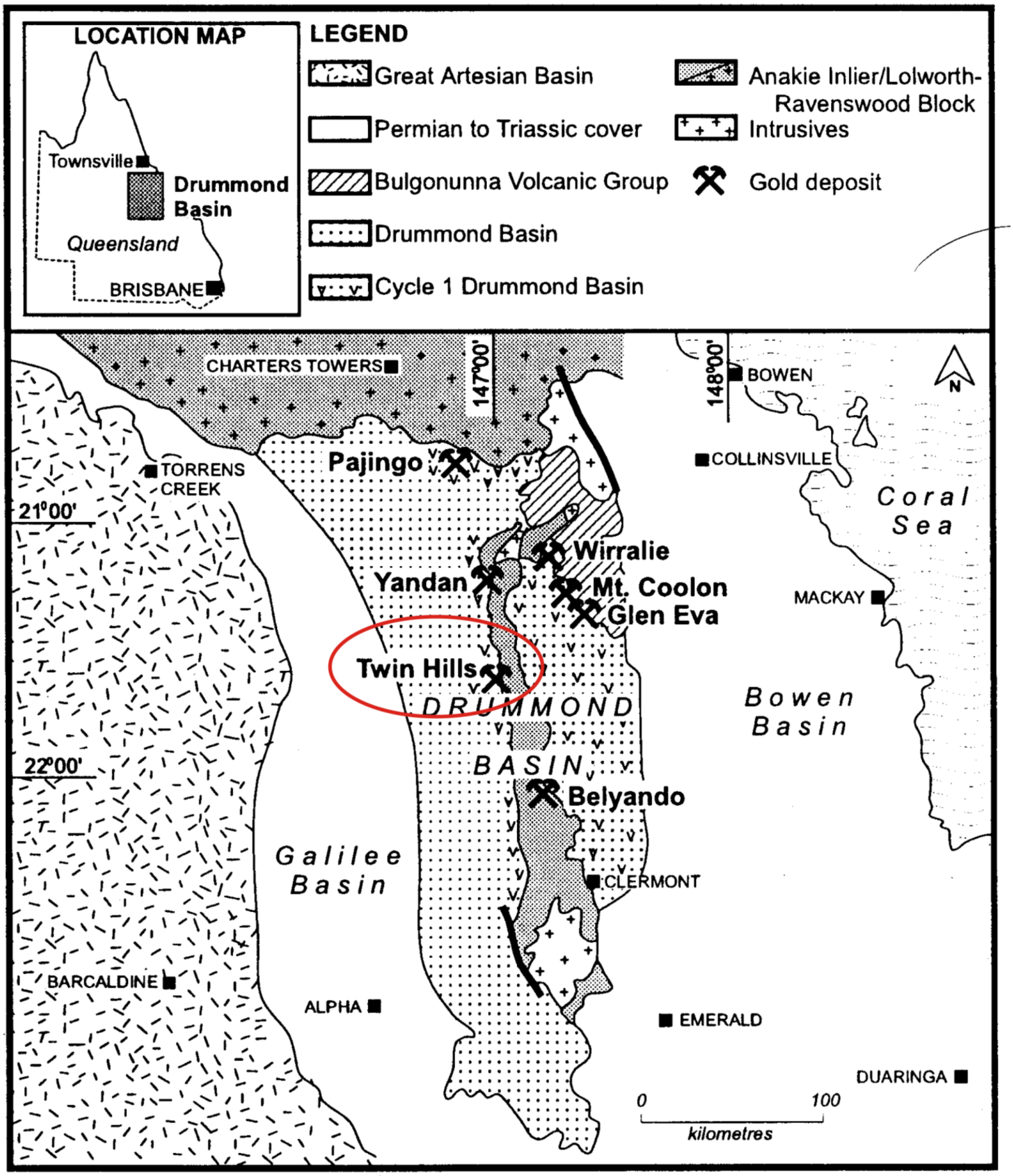

LOCATION MAP
Townsville
Drummond Basin
Queensland
BRISBANE
LEGEND
Great Artesian Basin
Permian to Triassic cover
Bulgonunna Volcanic Group
Drummond Basin
Cycle 1 Drummond Basin
Anakie Inlier/Lolworth-Ravenswood Block
Intrusives
Gold deposit
CHARTERS TOWERS
147°00'
148°00'
BOWEN
COLLINSVILLE
Coral Sea
TORRENS CREEK
21°00'
Pajingo
Wirralie
Yandan
Mt. Coolon
Glen Eva
MACKAY
Twin Hills
DRUMMOND BASIN
Bowen Basin
22°00'
Belyando
Galilee Basin
CLERMONT
BARCALDINE
ALPHA
EMERALD
DUARINGA
0
100
kilometres

Figure One

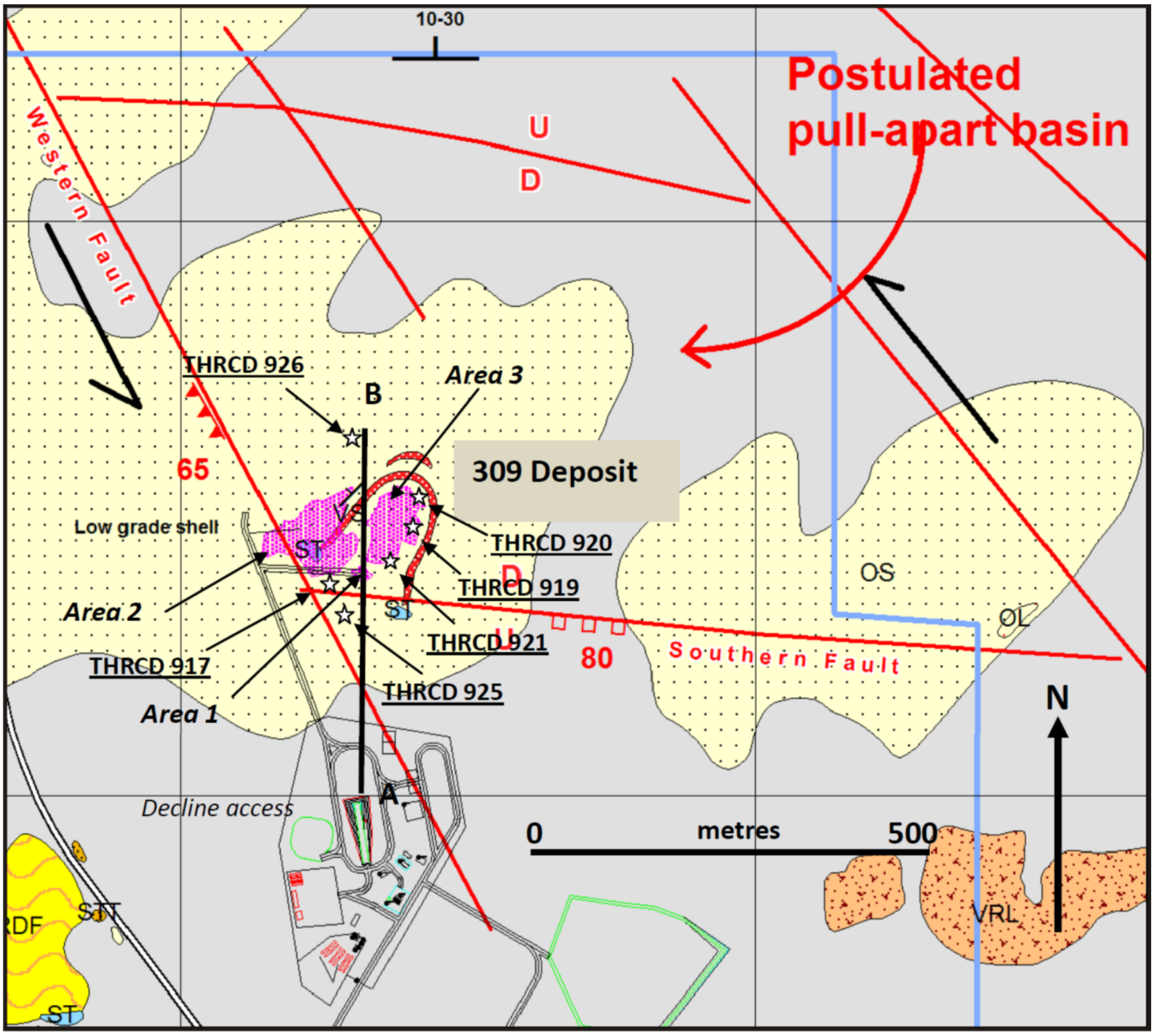
10-30
Postulated
pull-apart basin
U
D
Western Fault
THRCD 926
B
Area 3
309 Deposit
65
Low grade shell
ST
THRCD 920
THRCD 919
OS
OL
Area 2
D
THRCD 921
80
Southern Fault
THRCD 917
THRCD 925
Area 1
N
Decline access
A
0
metres
500
RDF
ST
ST
VRL

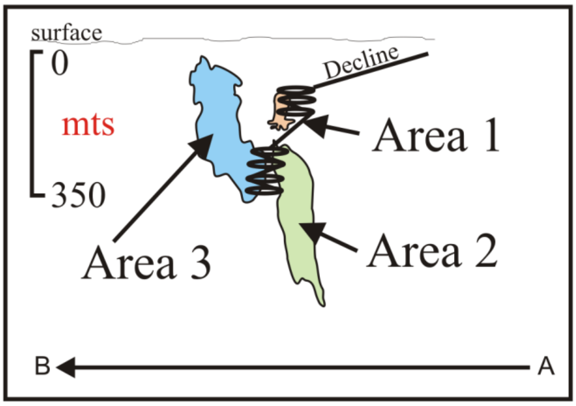
surface
0
mts
350
Decline
Area 1
Area 3
Area 2
B
A

Figure Two

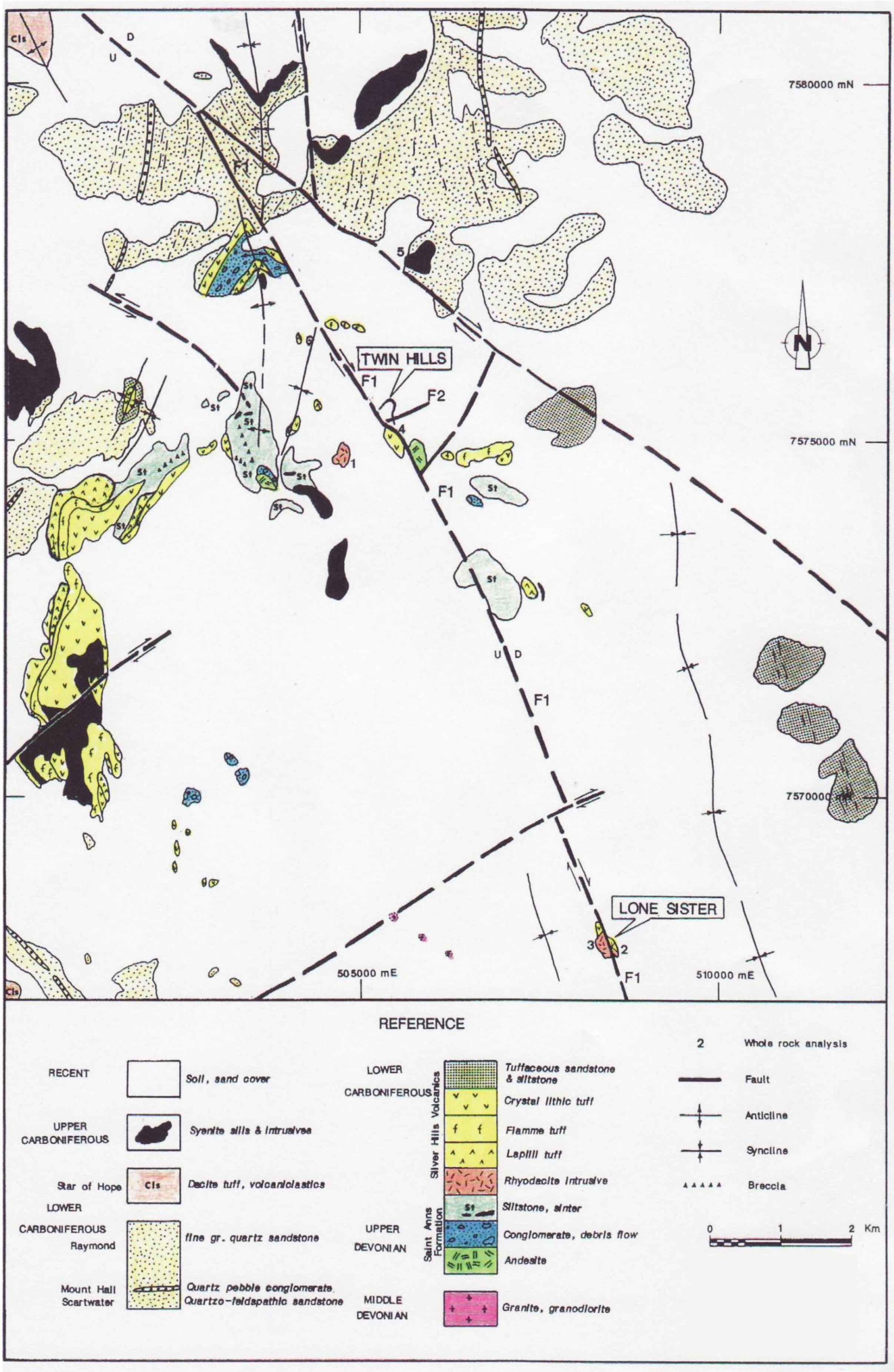

Figure Three

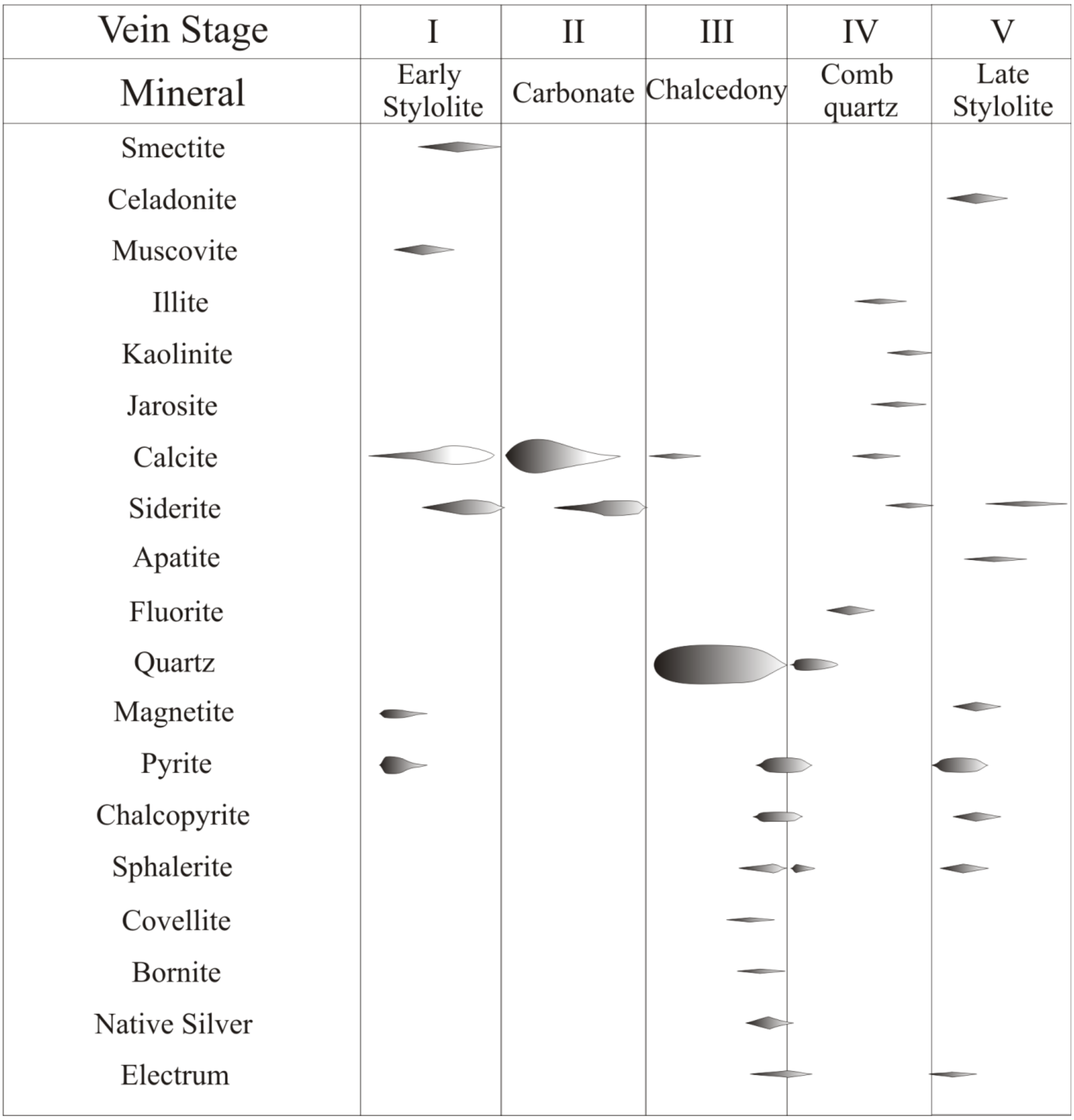
Vein Stage
I
II
III
IV
V
Mineral
Early Stylolite
Carbonate
Chalcedony
Comb quartz
Late Stylolite
Smectite
Celadonite
Muscovite
Illite
Kaolinite
Jarosite
Calcite
Siderite
Apatite
Fluorite
Quartz
Magnetite
Pyrite
Chalcopyrite
Sphalerite
Covellite
Bornite
Native Silver
Electrum

Figure Four

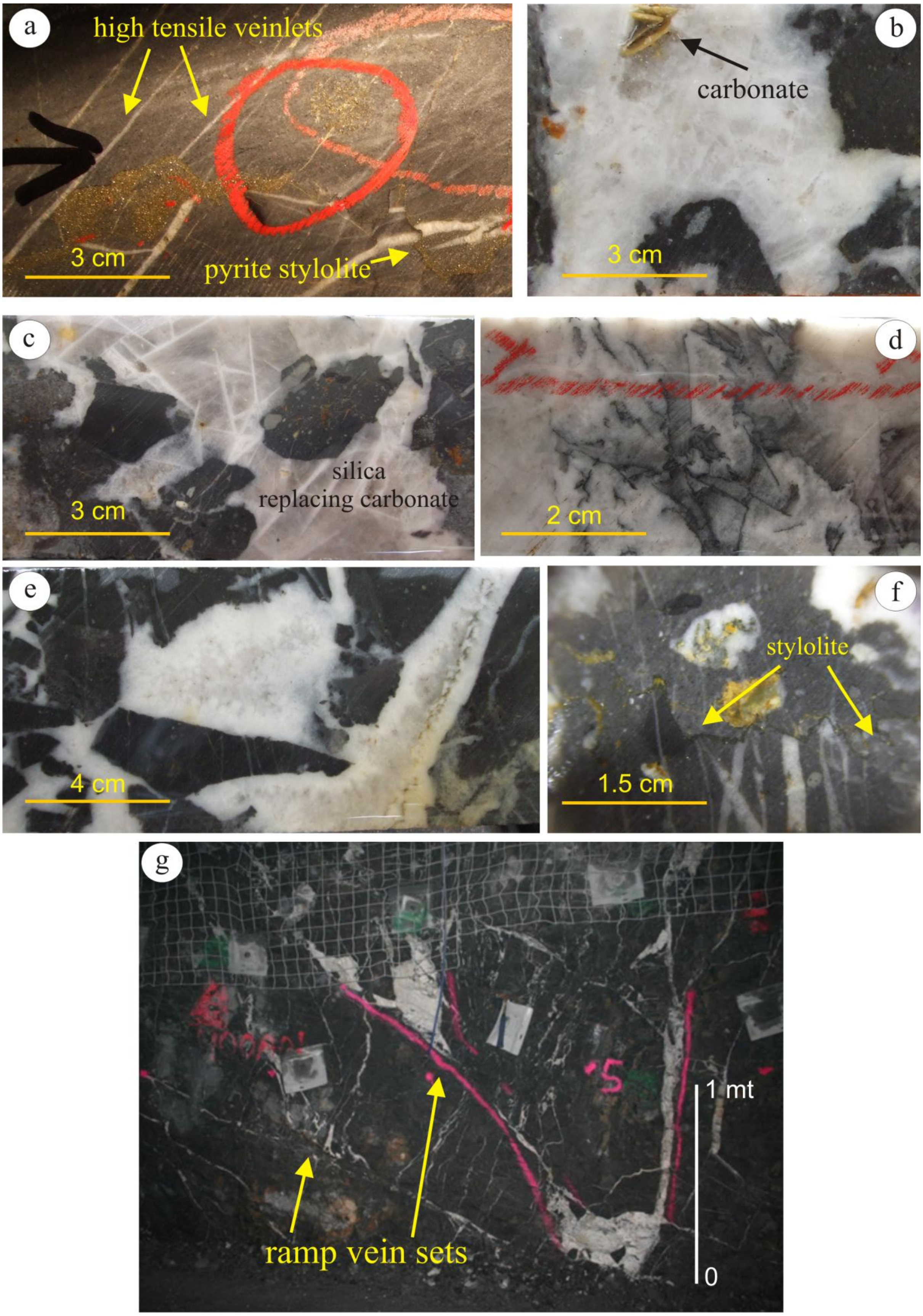
a
high tensile veinlets
3 cm
pyrite stylolite
b
carbonate
3 cm
c
silica
replacing carbonate
3 cm
d
2 cm
e
4 cm
f
stylolite
1.5 cm
g
1 mt
0
ramp vein sets

Figure Five

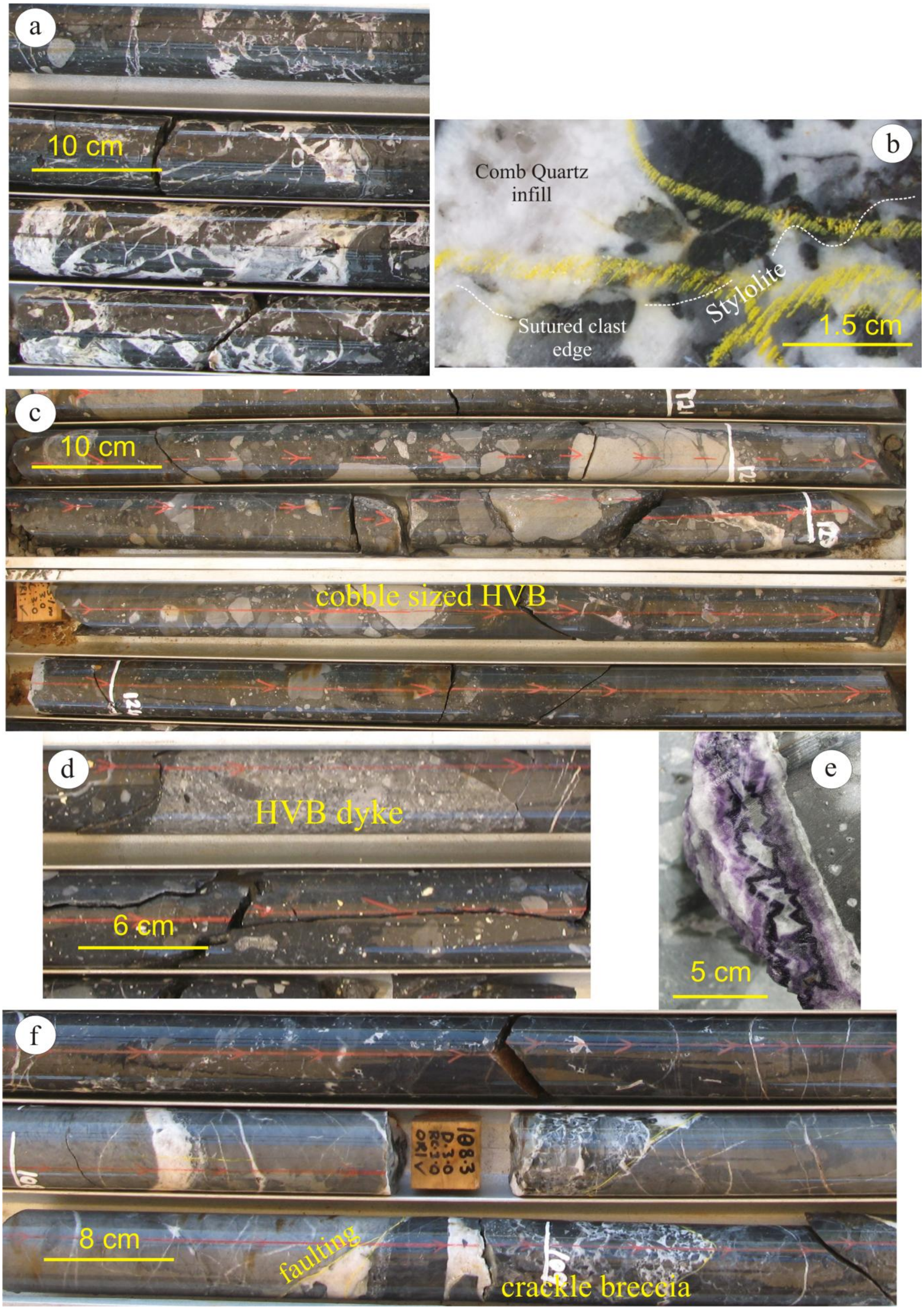
a
10 cm
b
Comb Quartz infill
Sutured clast edge
Stylolite
1.5 cm
c
10 cm
cobble sized HVB
d
HVB dyke
6 cm
e
5 cm
f
8 cm
faulting
crackle breccia

Figure Six

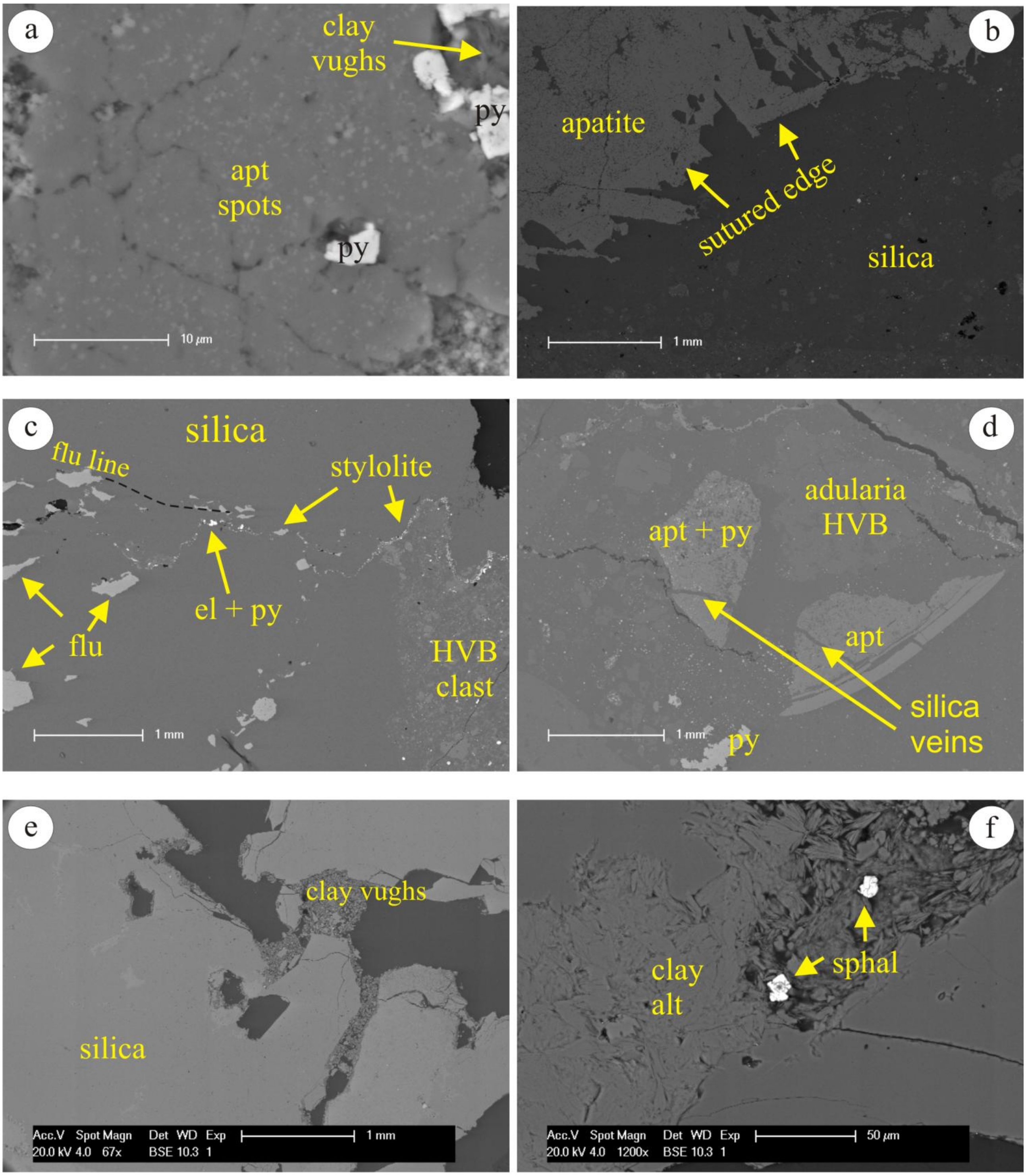

Figure Seven

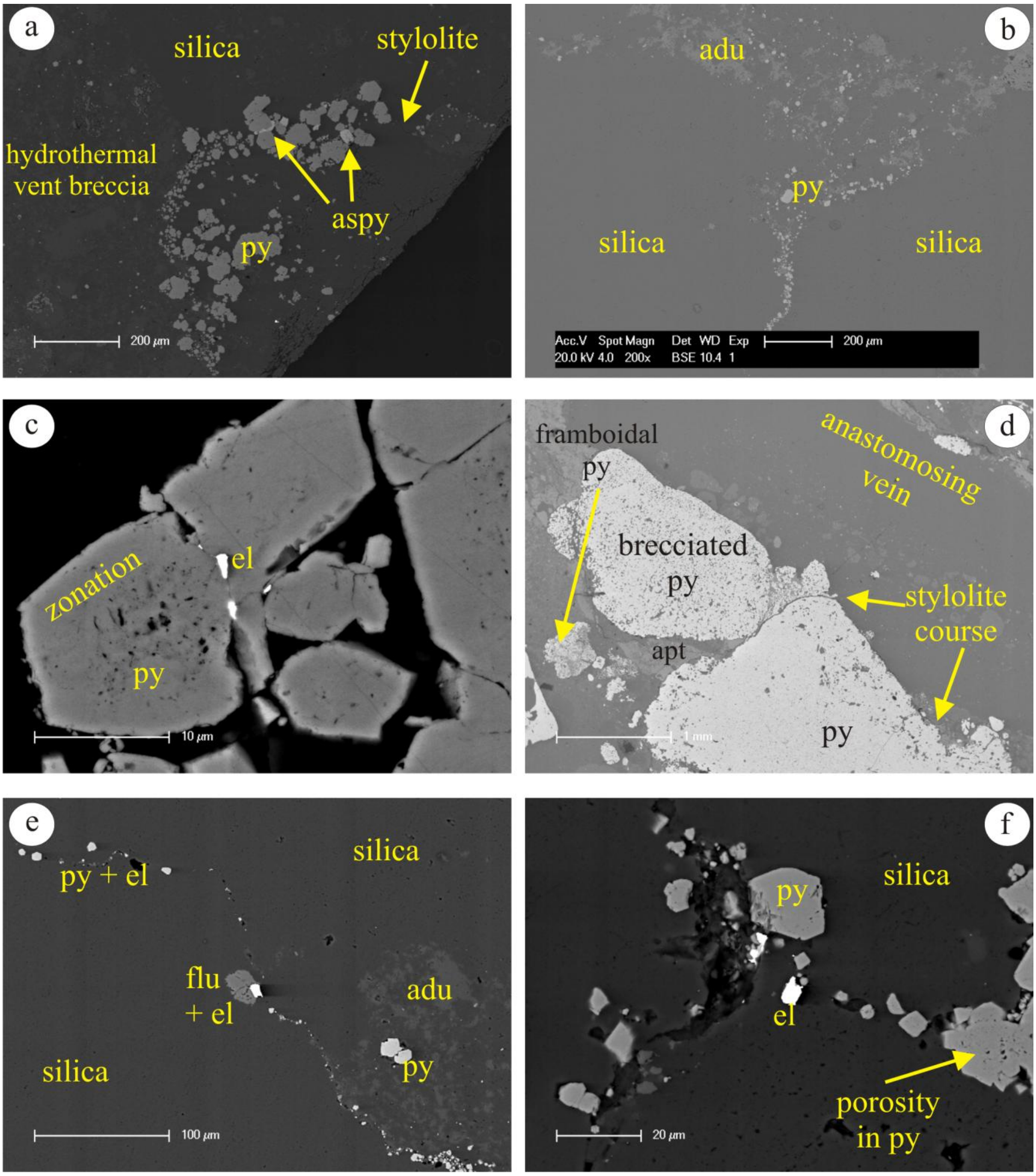

Figure Eight

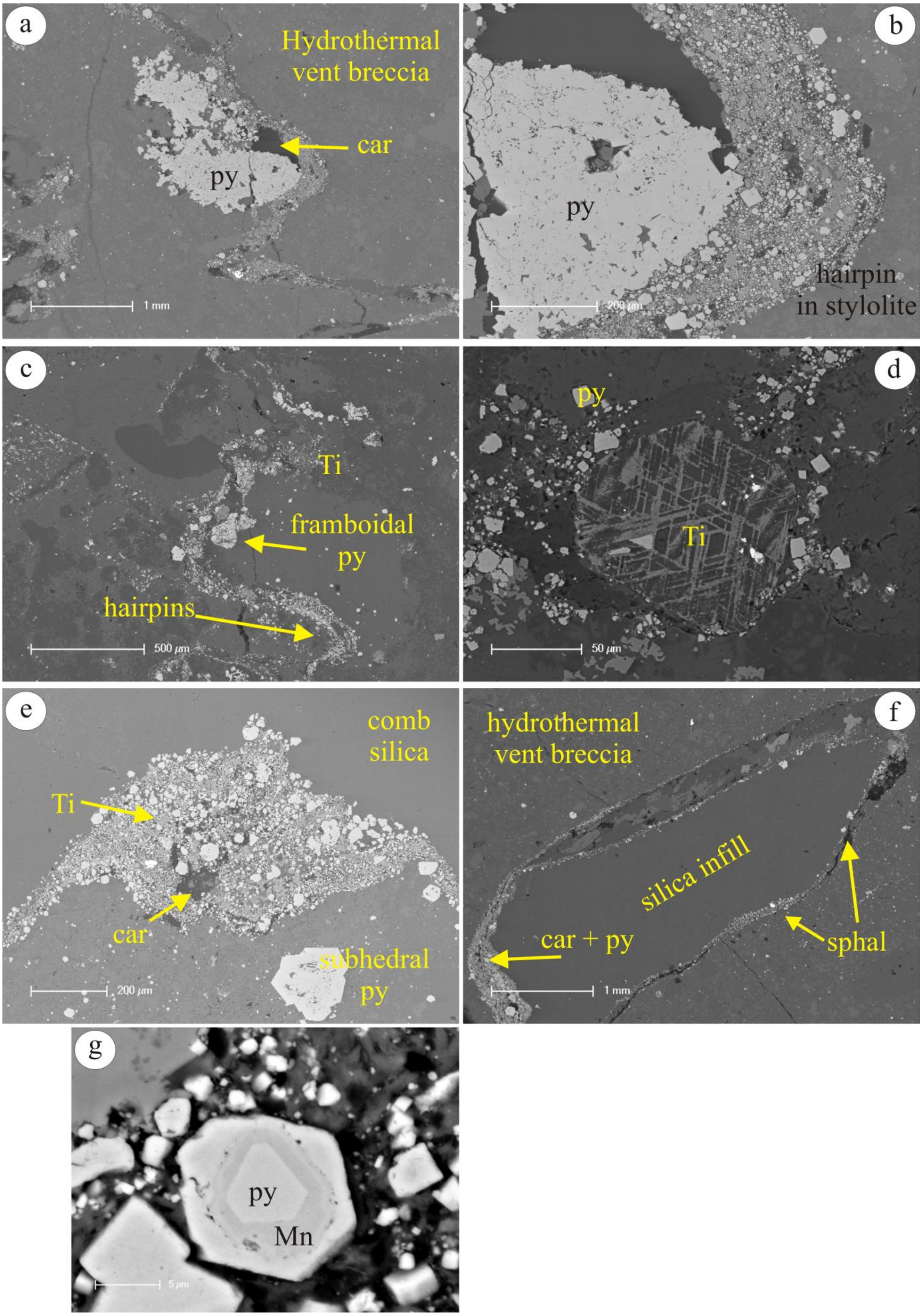
a
Hydrothermal vent breccia
car
py
1 mm
b
py
200 µm
hairpin in stylolite
c
Ti
framboidal py
hairpins
500 µm
d
py
Ti
50 µm
e
comb silica
Ti
car
subhedral py
200 µm
f
hydrothermal vent breccia
silica infill
car + py
sphal
1 mm
g
py
Mn
5 µm

Figure Nine

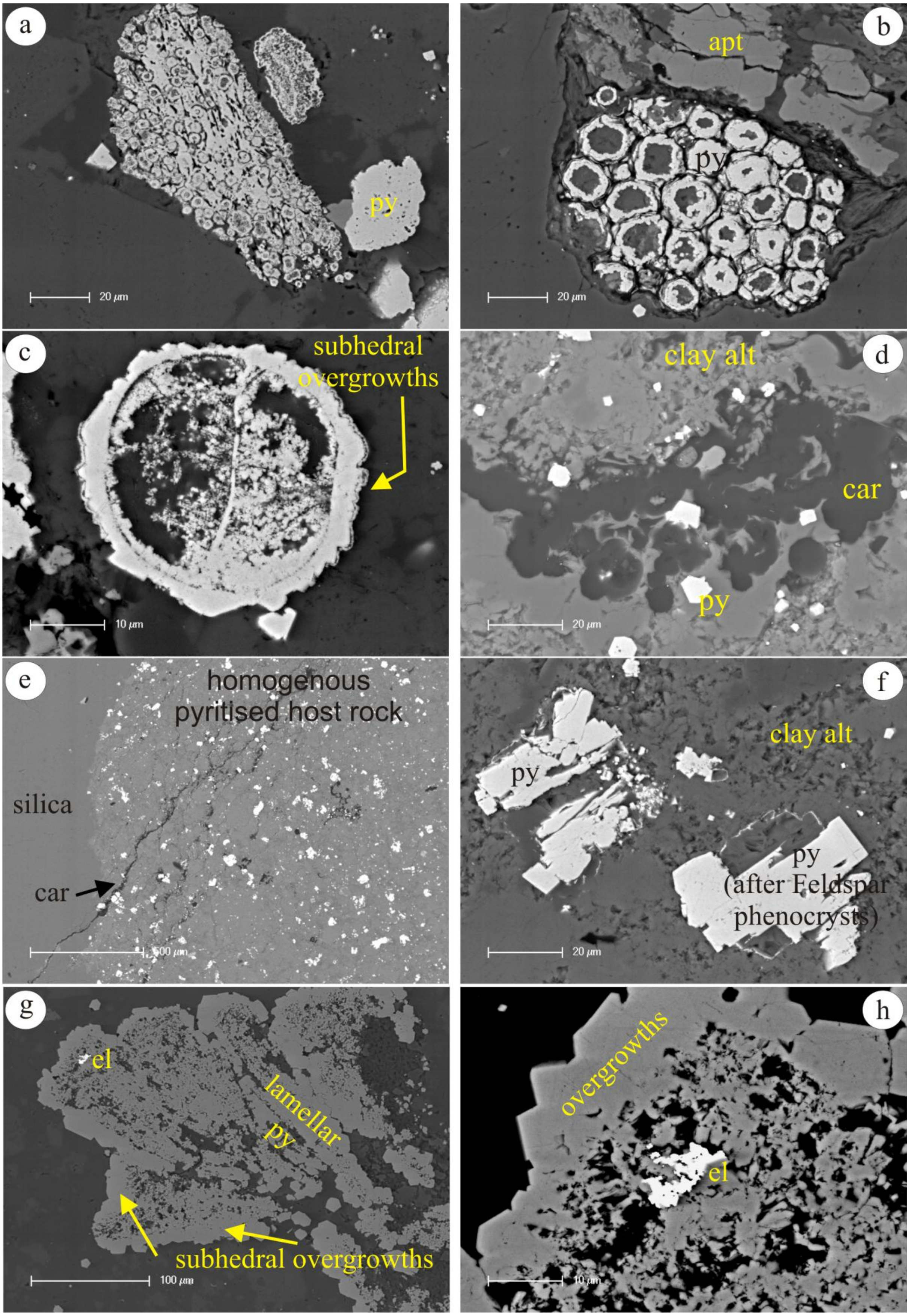
a
20 μm
py
b
apt
py
20 μm
c
subhedral overgrowths
10 μm
d
clay alt
car
py
20 μm
e
homogenous pyritised host rock
silica
car
100 μm
f
clay alt
py
py (after Feldspar phenocrysts)
20 μm
g
el
lamellar py
subhedral overgrowths
100 μm
h
overgrowths
el
10 μm

Figure Ten

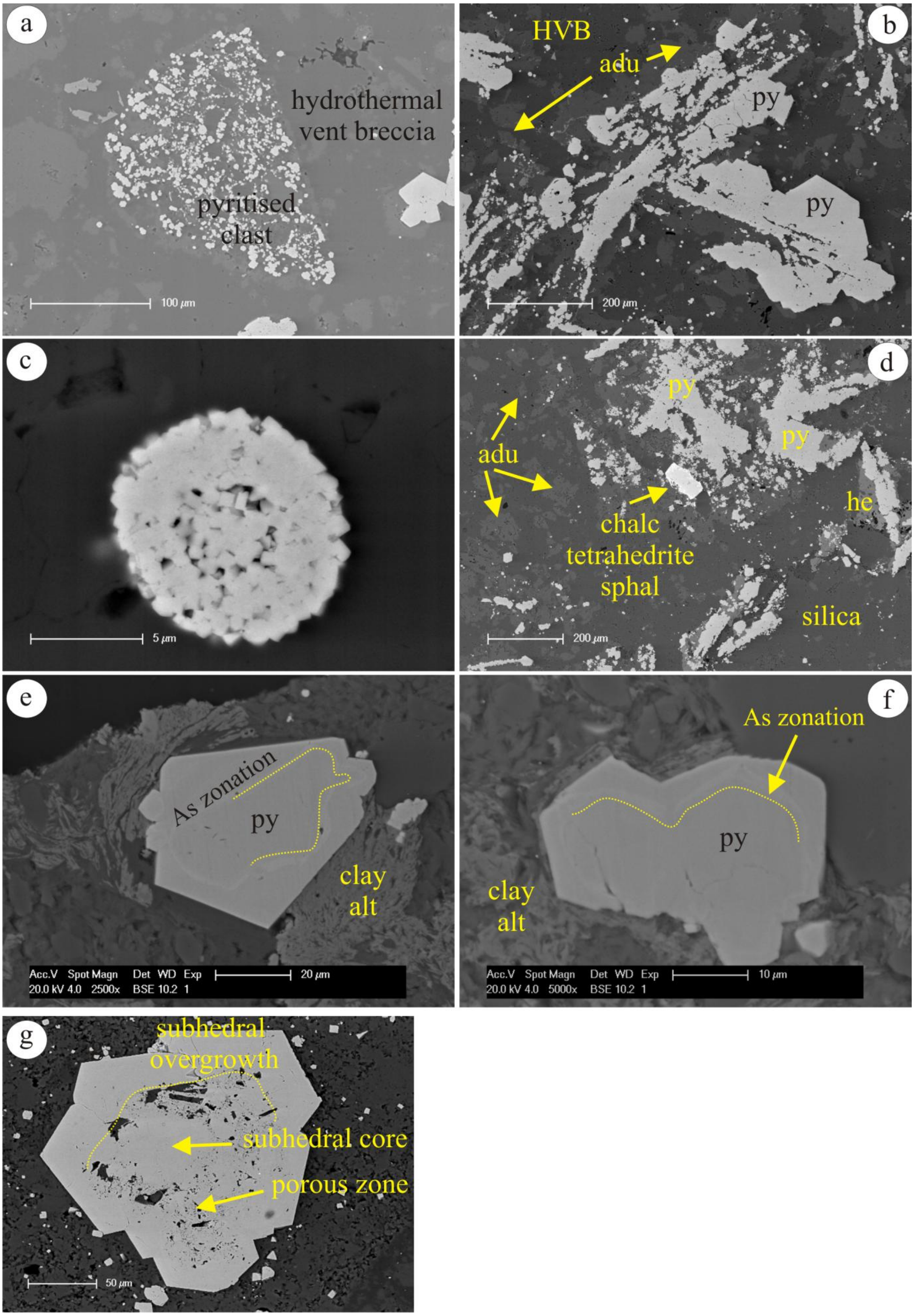

Figure Eleven

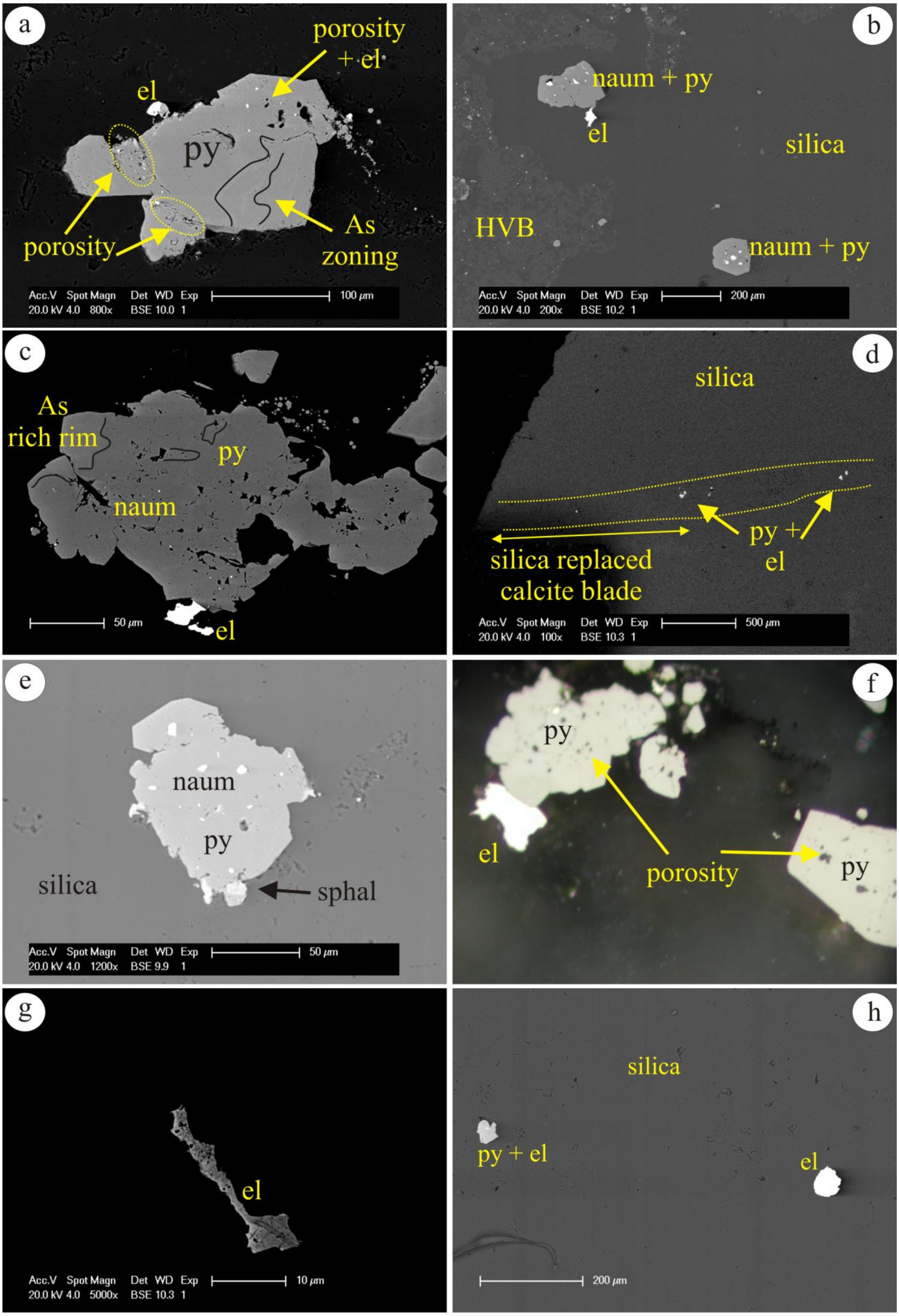

Figure Twelve

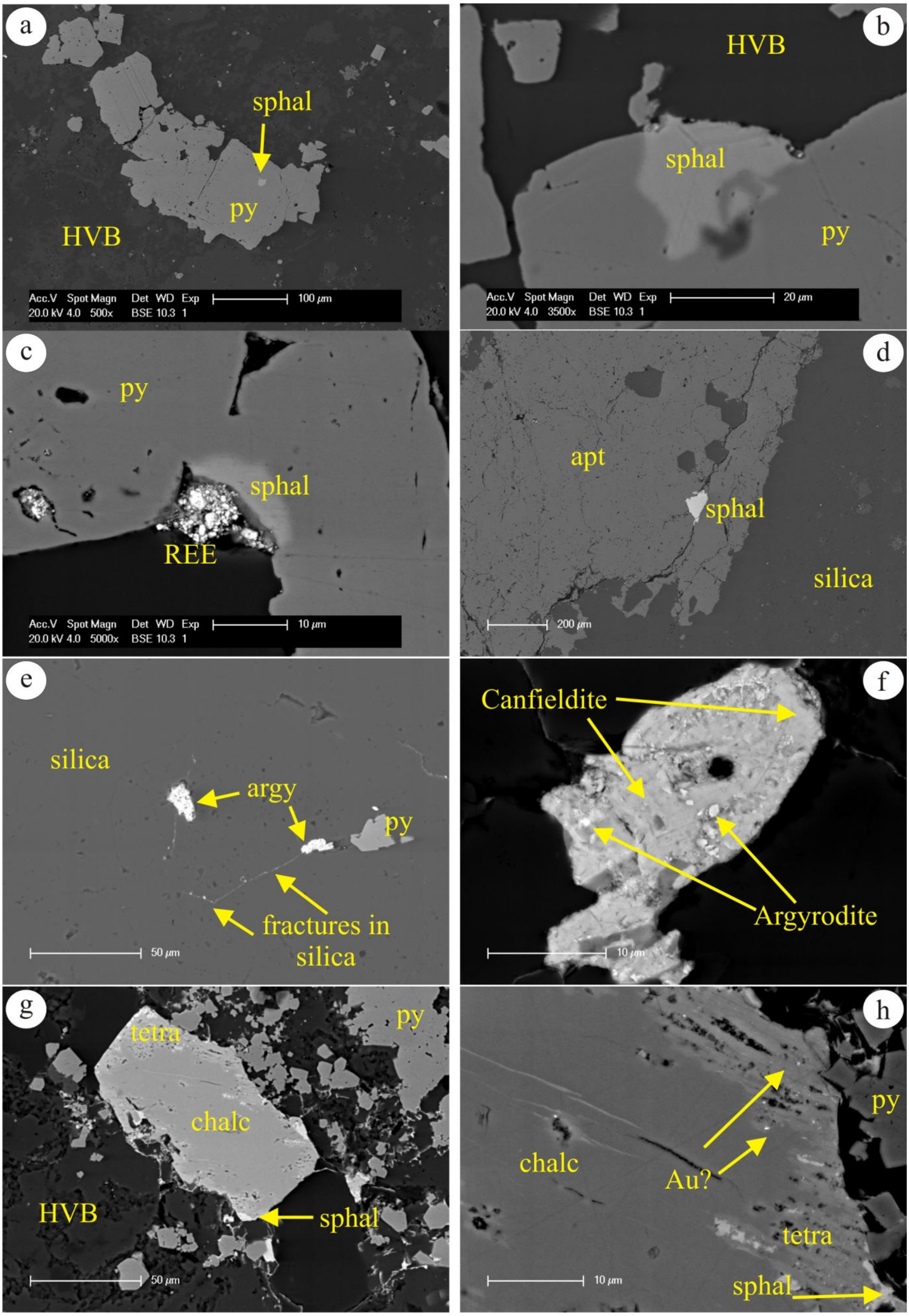

Figure Thirteen

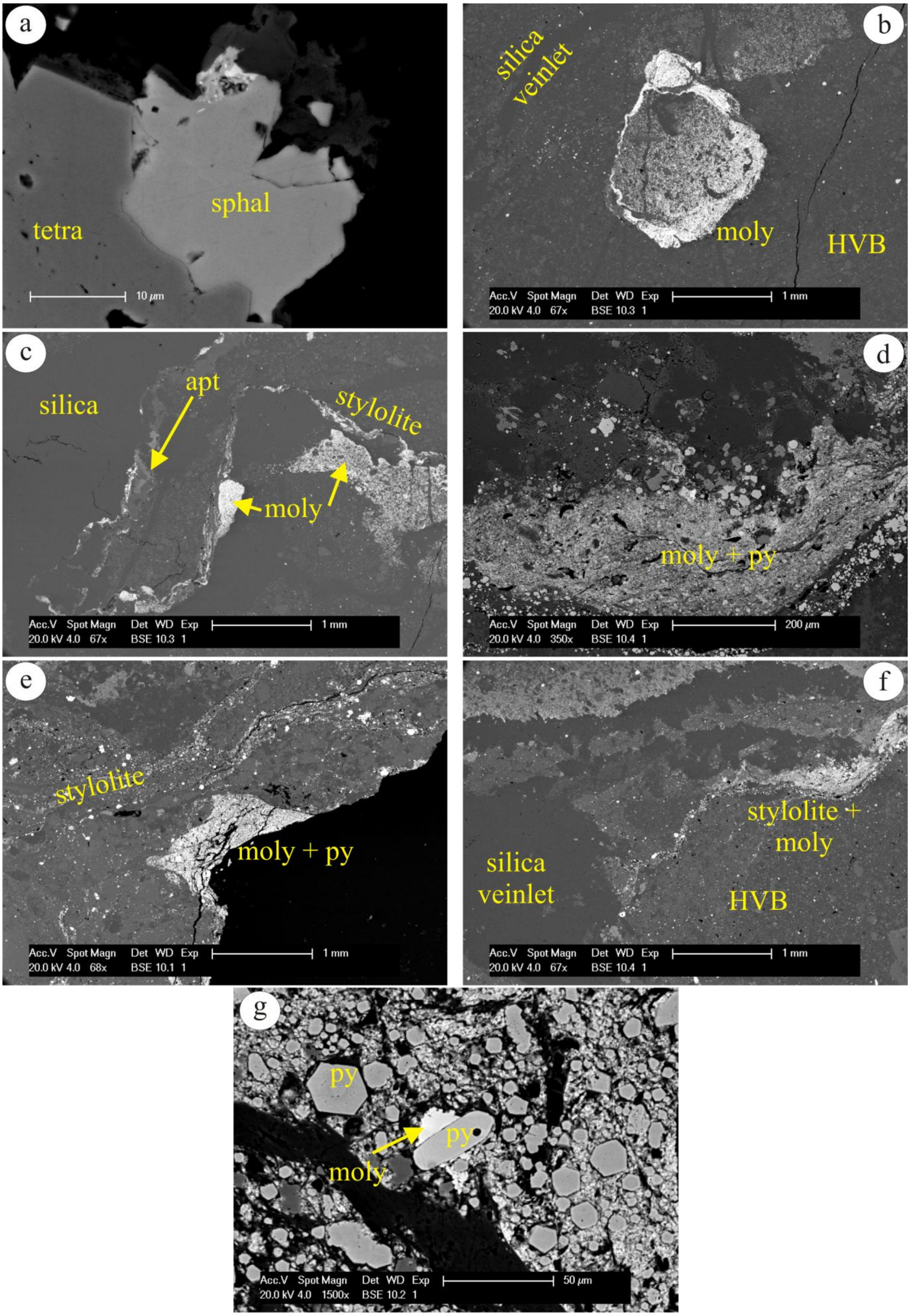

Figure Fourteen

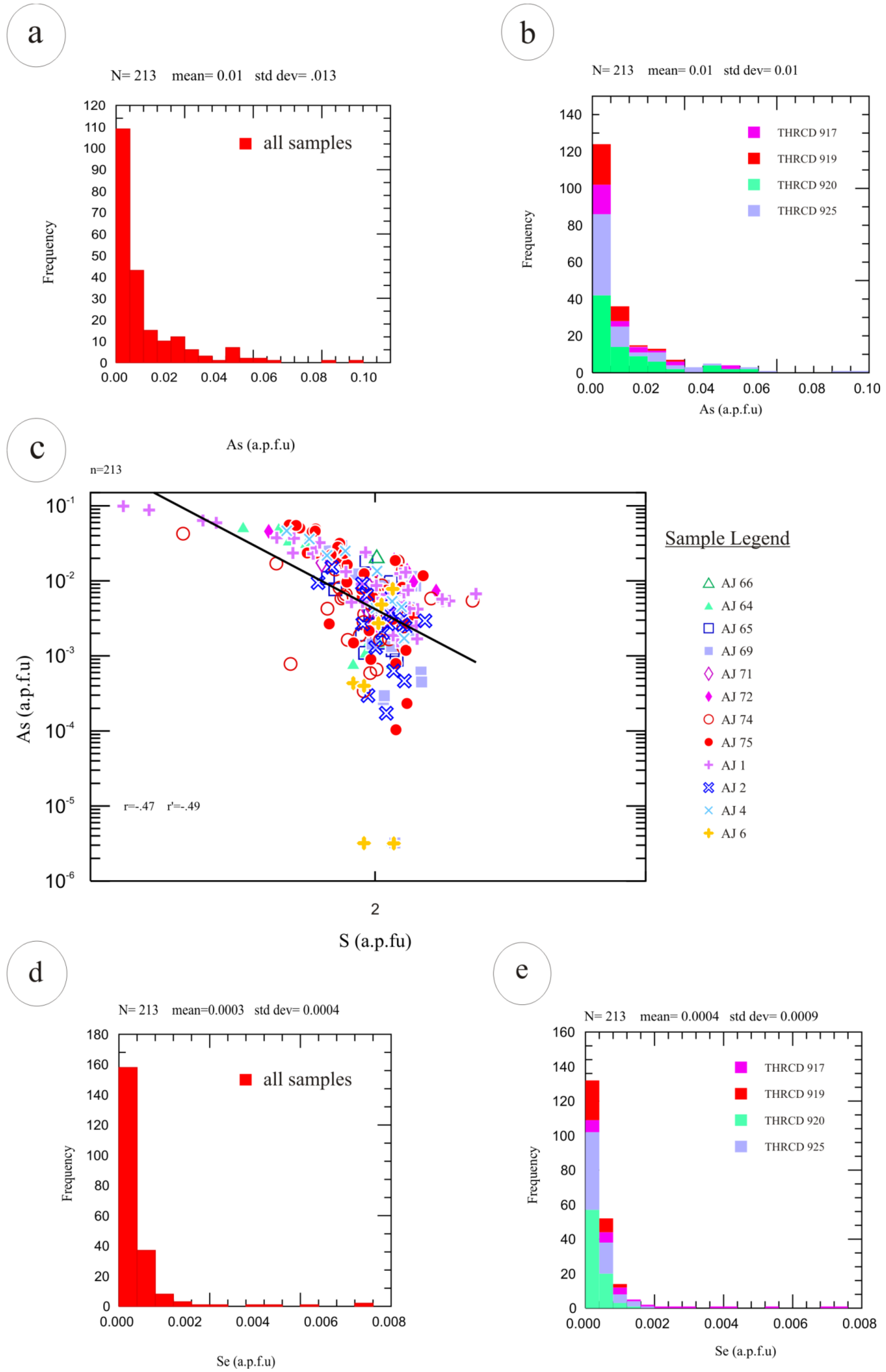

Figure Fifteen

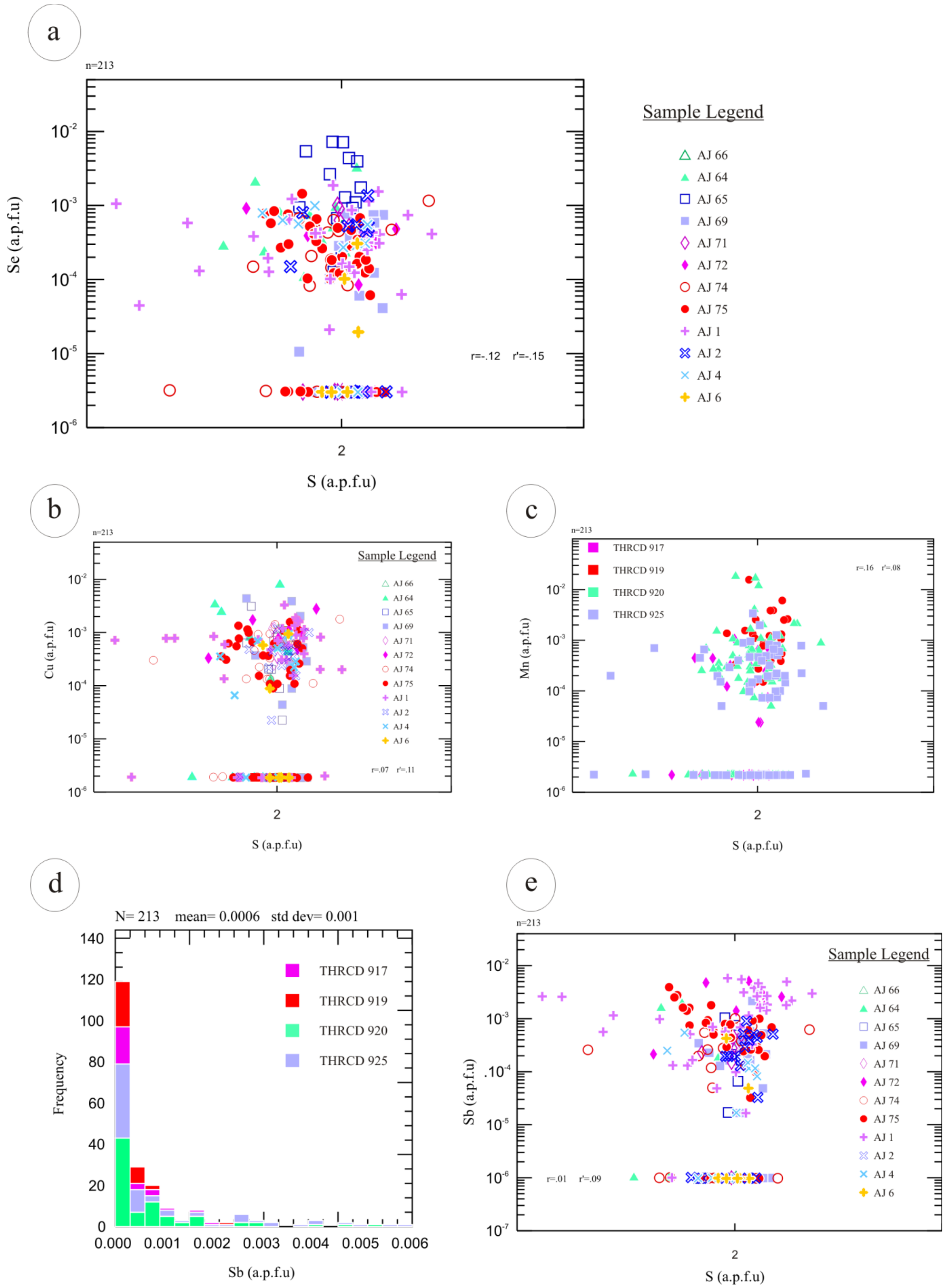

Figure Sixteen

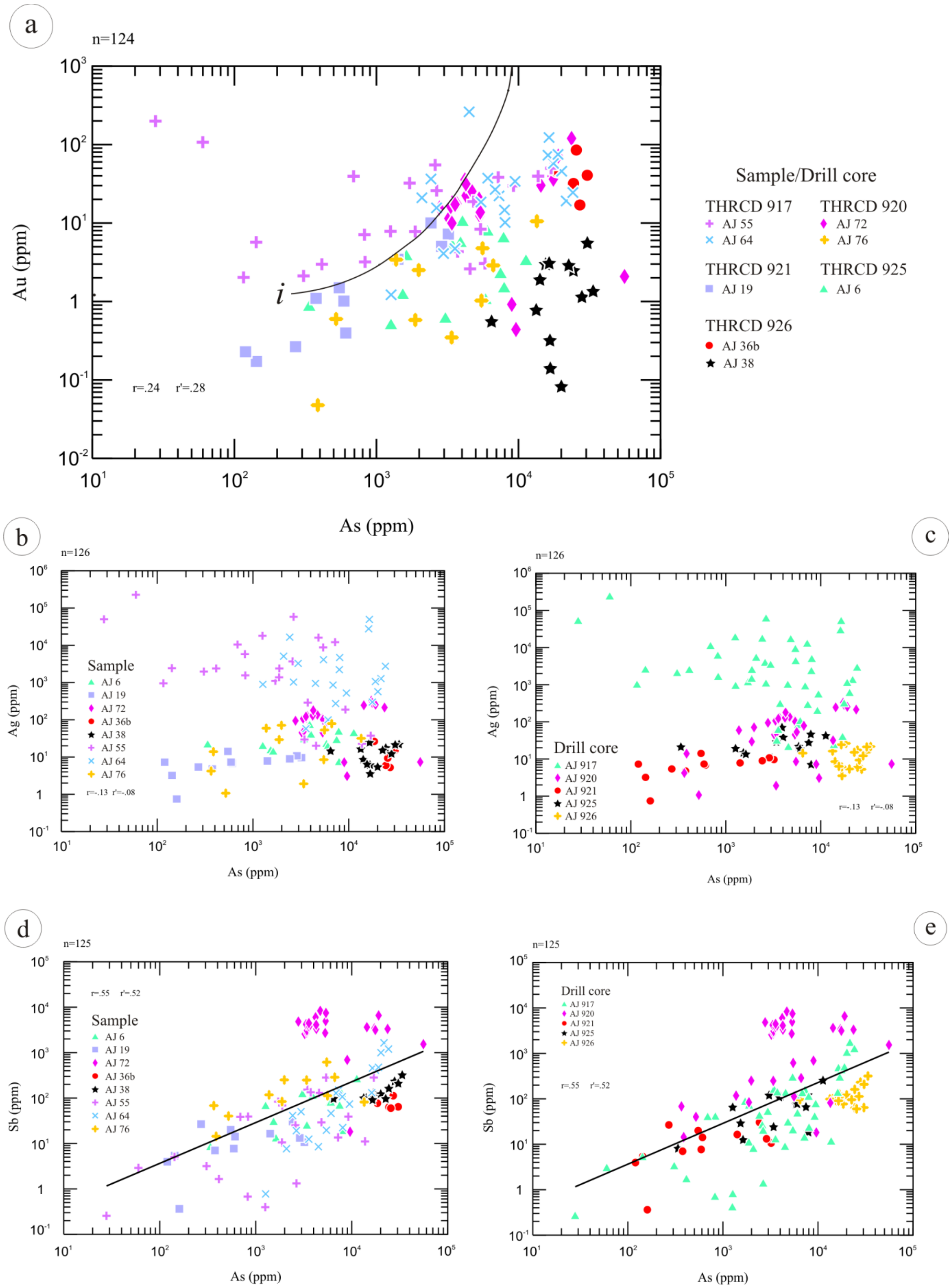

Figure Seventeen

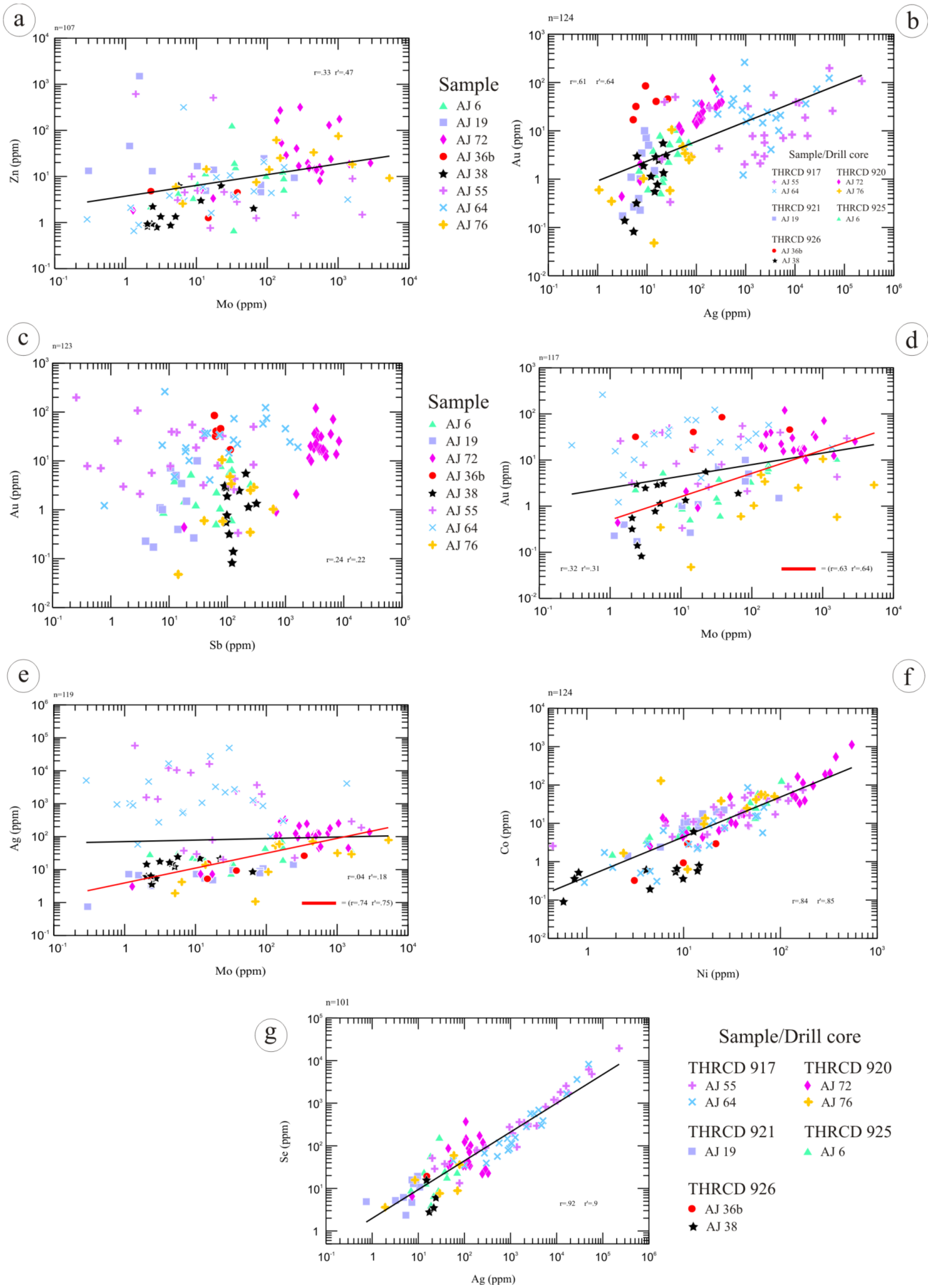

Figure Eighteen

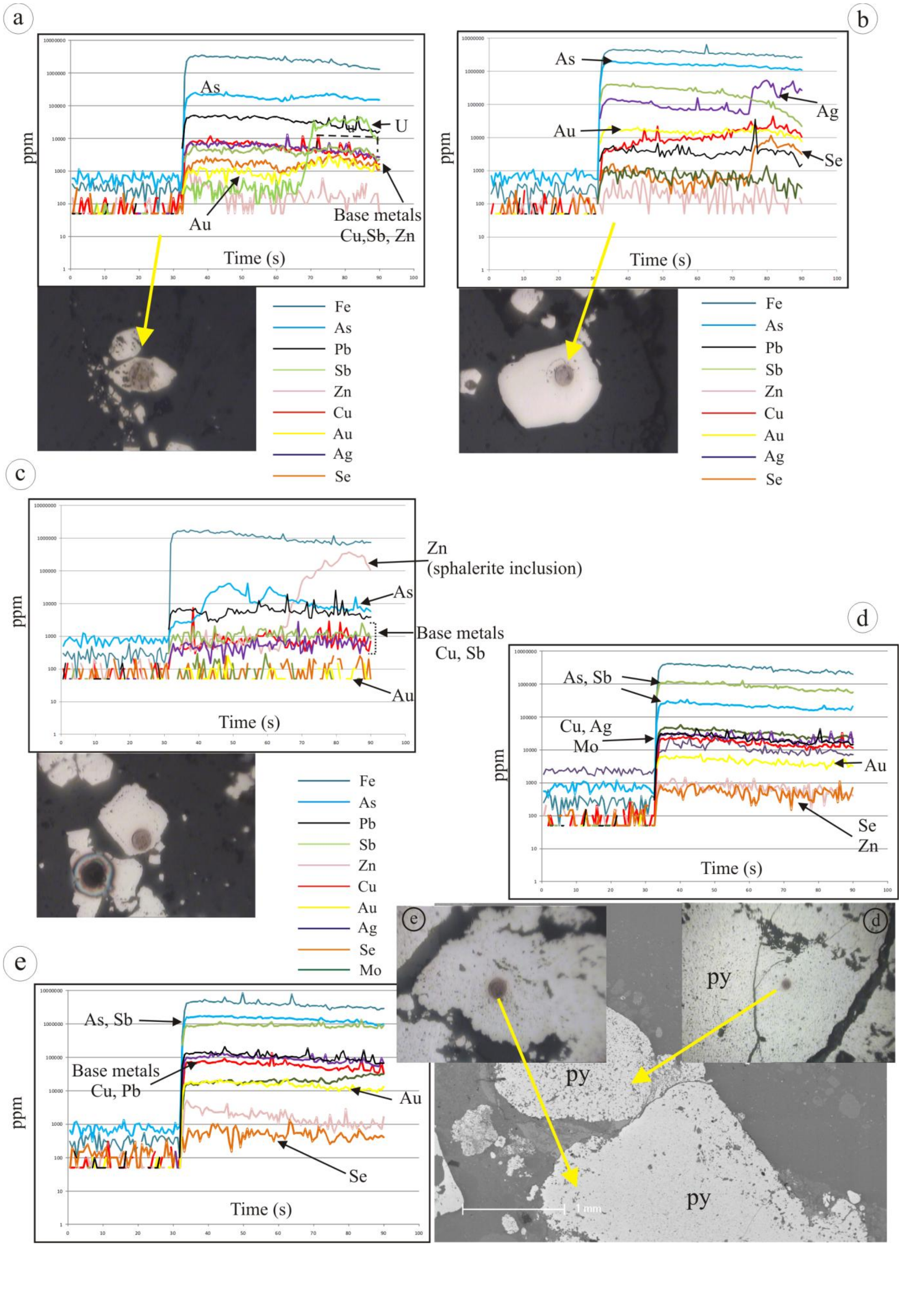

Figure Nineteen

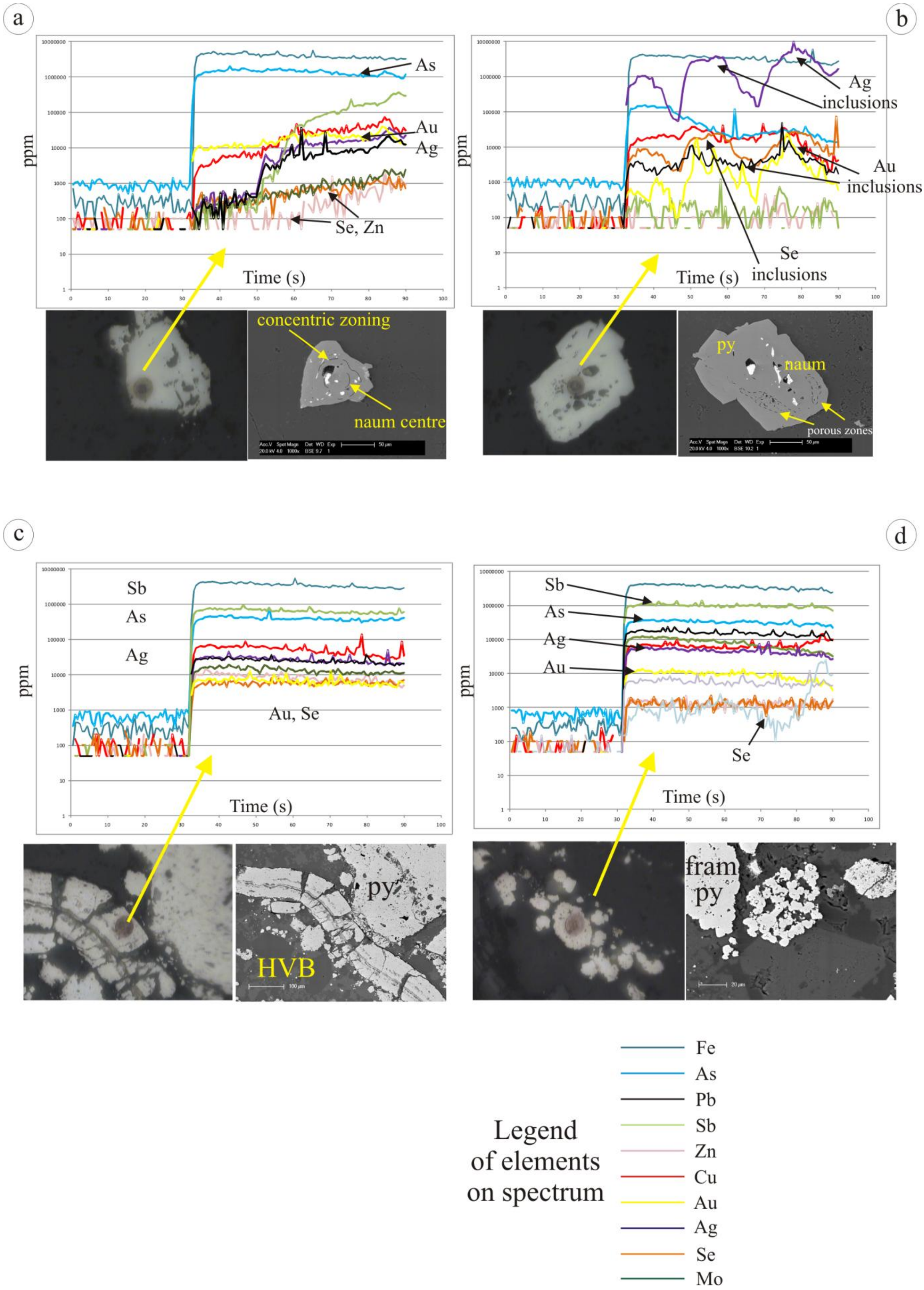

Figure Twenty

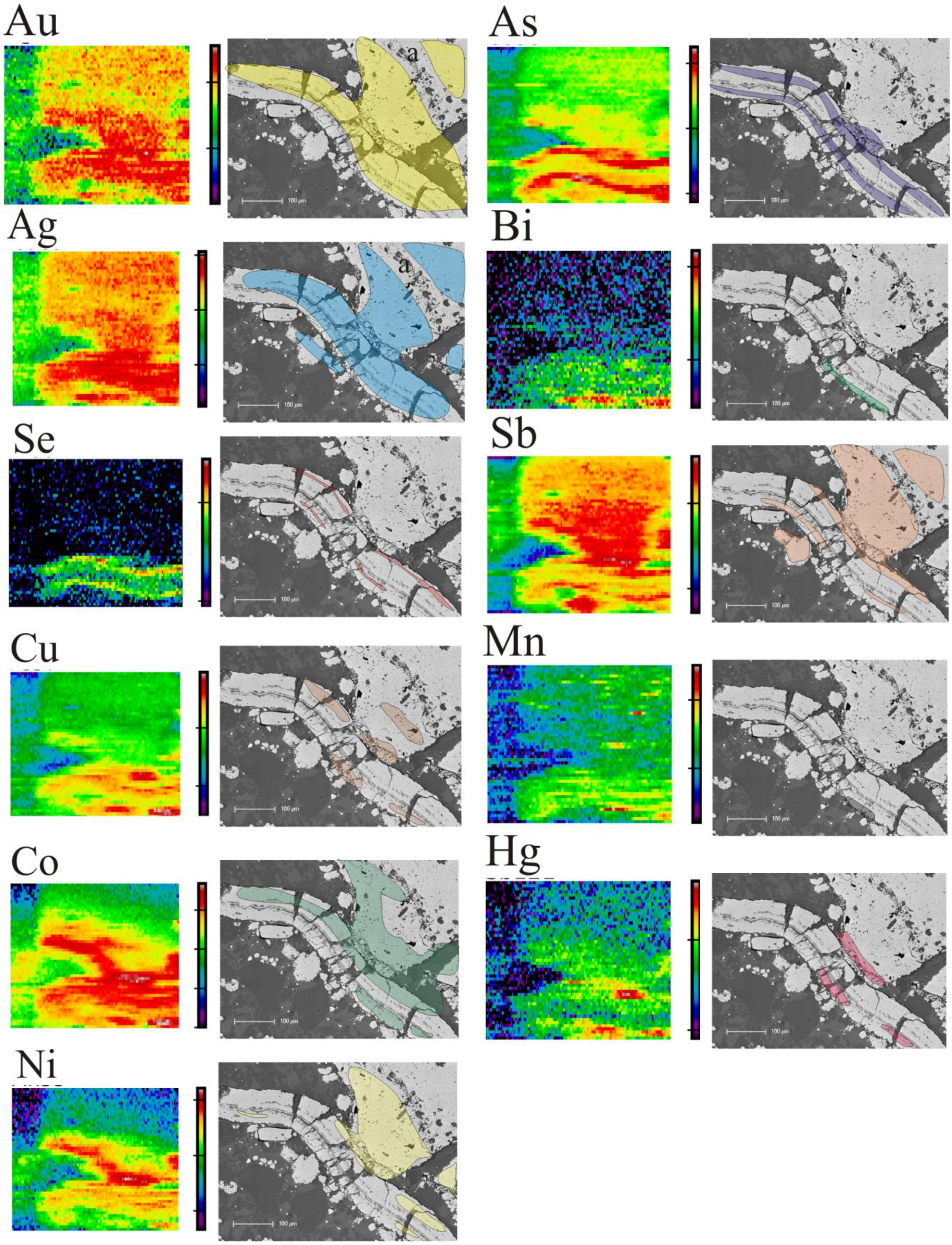

Figure Twenty One

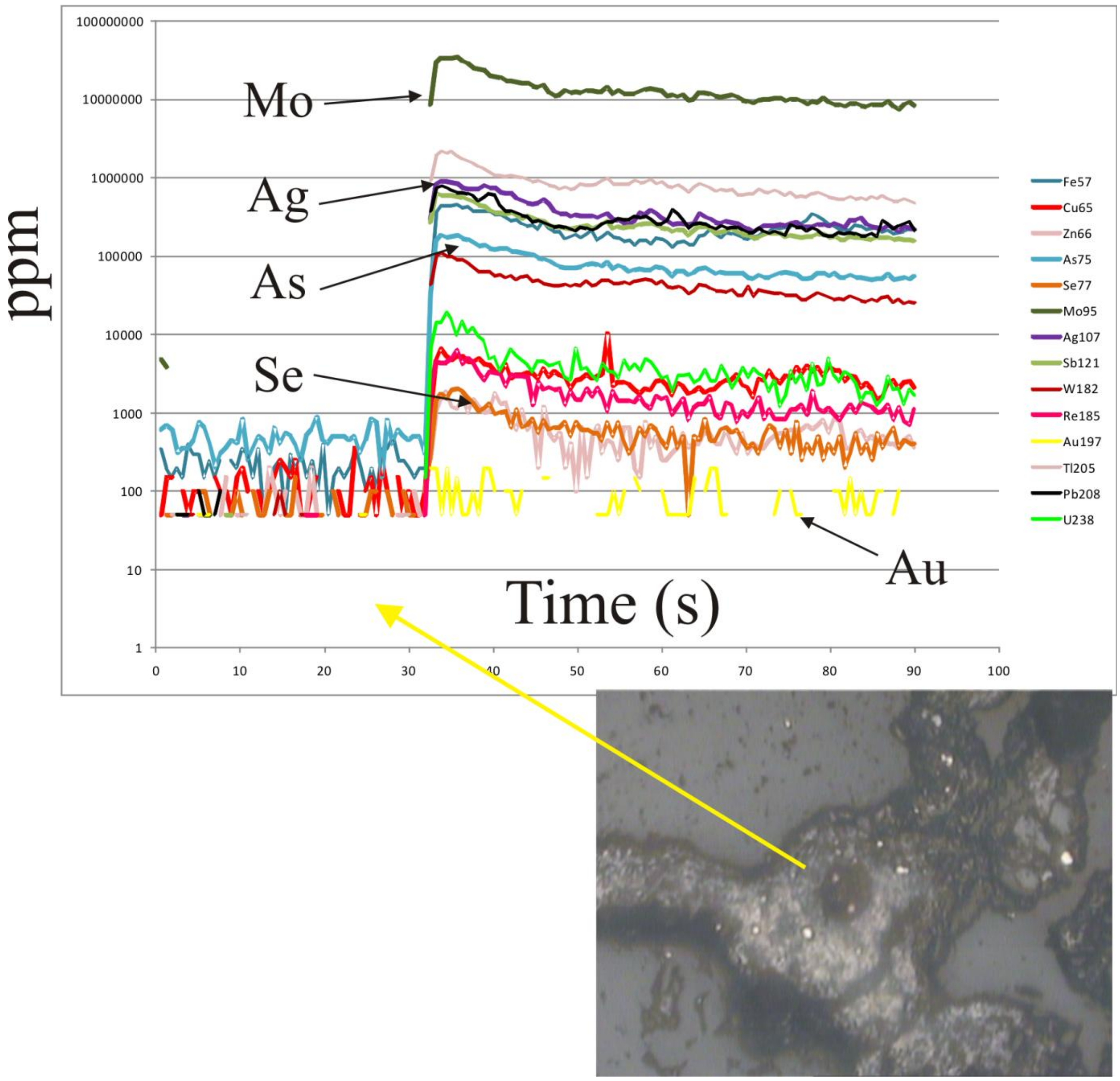

Figure Twenty Two

CAPTIONS TO FIGURES

Fig. 1. Regional epithermal deposits within the Drummond Basin, central north Queensland. Current NQM operations are located at Pajingo and Twin Hills (Cirlced in red).

Fig. 2. Simplified local geology showing the proposed Twin Hills sub basin (*after* Corbett 2006a). Recent drill cores used in this study have also been plotted. Cross section A-B (*inset)* shows current underground decline access to workings with relative positions of the 3 resource areas interpreted by BMA. Drill cores used in this study were primarily focussed around area 2.

Fig. 3. Regional geology of the Twin Hills epithermal region. *reproduced from* (Sennit 1991).

Fig. 4. Proposed paragenetic sequences of mineralisation present at the Twin Hills 309 epithermal deposit *after* (Sennit 1991).

Fig. 5. Representative mineralisation and veining styles within the Twin Hills 309 epithermal deposit. (a) High Tensile veining caused by local dilation with late stylolite and pyrite, *sample AJ 2*. (b) Calcite (carbonate) replacement by chalcedonic silica. (c) Silica replaced bladed calcite textures. (d) Chalcedonic silica with weak *ginguro* mineralisation. (e) Hydrothermal crackle breccia infill with angular brecciated wall rock clasts. (f) Stylolite as seen under hand lens. High tensile stringer veins terminate at stylolite contact; this is taken as evidence for pressure-solution mechanisms. (g) Underground view in area 2 of flat ramp veining (*yellow arrows).* Large anastomosing vertical veins act like 'pipes' and feeders to nearby veins, creating vein sets or packages. Junction of veins create hydrotermal crackle breccia infills.

Fig. 6. Representative mineralisation within the Twin Hills 309 epithermal deposit, core logging examples. (a) Anastomosing chalcedonic and comb quartz veinlets. (b) Late stage stylolites showing sutured contact and dissolution of clasts boundaries by stylolites. (c) Hydrothermal vent breccia host rock, showing cobble sized clasts (*at top).* Clasts consist of arenites, mudstones and previous brecciated fragments. (d) Dyke consisting of remobilised hydrothermal vent breccia. Note the roundness of remobilised pebbles. (e) Fluorite infill veins. (f) Local faulting *as marked* showing

comb quartz vein infills at dilation sites. A crackle breccia has also been faulted. The sharp contact suggests that the faults are post to the crackle breccia infilling. *Abbreviations;* HVB= Hydrothermal vent breccia.

Fig. 7. Gangue minerals in the Twin Hills 309 epithermal deposit. BSE images. (a) Spots of hydrothermal apatite overprinting clasts in breccia. (b) Silicification altering apatite edge showing sutured edge. (c) Fluorite overprinted by late pyrite and electrum stylolites. Fluorite line shows the original fluorite along the vein wall. (d) Apatite clasts within hydrothermal vent breccia host rock. Note overprinting quartz veinlets, these are associated with pyrite and electrum stylolites. (e) (f) Clay alteration (illites, kaolinite) within vughs in the silica. Sphalerite has later infilled vughs. *Abbreviations; apt= apatite; py= pyrite; flu= fluorite; el= electrum; sphal= sphalerite.*

Fig. 8. Distribution of ore textures within the Twin Hills 309 epithermal deposit; Pyrite and electrum stylolites. BSE images. (a) Pyrite and electrum late stylolites overprinting breccia host. Arsenopyrite is present, wedged between zoned pyrites. *AJ 6*(b) As-rich zoned pyrite stylolite in chalcedonic silica vein. *AJ 36B*(c) detail of (a), showing electrum precipitated between pyrite grains in stylolite. Note adjacent pyrite grain centres are outlined by porosity.and subeuhdral overgrowths displaying compositional zonation with respect to As. (d) Pyrite aggregate formed on edge of anastomosing vein. Late stylolite has caused the mass to brecciate. Stylolite follows edge of anastomsing vein. *AJ 72*(e) Late pyrite and electrum-rich stylolites with fluorite. *AJ 6*(f) Pyrite and electrum stylolite detail, showing porosity in pyrite centre.*AJ 6. Abbreviations: aspy= arsenopyrite; py= pyrite; adu= adularia; el= electrum; apt= apatite; flu= fluorite.*

Fig. 9. Distribution of ore textures within the Twin Hills 309 epithermal deposit; carbonaceous/titanium stylolites. BSE images. (a) Carbon at the hair pin of a stylolite. *AJ 60*(b) brecciation of the pyrite aggregate seen in (a). (c) Framboids and titanium dioxide is present within stylolite. Note wavy hair pin of stylolite course. *AJ 71*(d) Rutile undergoing alteration along crystal axes. *AJ 71*(e) contrasting pyrite morphology at the 'hair-pin' of a stylolite. Large subeuhedral pyrite in adjacent breccia, stylolite contains finer granular/euhedral pyrite. Note carbon and titanium dioxide. *AJ 69*(f) Carbonaceous stylolite taking advantage around a silica infill. Sphalerite mineralisation is associated. *AJ 69*(g) Manganese zonation in pyrites within stylolite shown in (e). *Abbreviations: py= pyrite; Mn= manganese; sphal= sphalerite; Ti= Rutile; Car= carbon.*

Fig. 10. BSE images of Pyrite morphology within the Twin Hills 309 epithermal deposit. (a) (b) (c) Pyritisation of organic matter (tree seeds, algae internal structures/attols); later subhedral pyrite appears as overgrowths. *AJ 72*(d) (e) (f) Bitumen-like material and pyrite pseudomorphing feldspar or adularia phenocrysts showing 'twinning' like crystals, adjacent to comb quartz vein. *AJ 1*(g) (h) marcasite with later granular/subhedral growth in lamellar fashion. Microscopic particle of gold within porous pyrite. *Abbreviations: py= pyrite; el= electrum; naum= naumannite; sphal= sphalerite; As= Arsenic-rich zonation;* CO^3*=calcium carbonate.*

Fig. 11. BSE images of Pyrite morphology within the Twin Hills 309 epithermal deposit (a) Pyritisation of a clast within the hydrothermal vent breccia, with associated silicification. Note the granular/euhedral pyrite growth. *AJ 6*(b) Lamellar overgrowths of subeuhedral pyrite on probable marcasite. (c) Framboidal pyrite. Commonly nucleate on organic matter. *AJ 2*(d) Laminates containing haematite. Chalcopyrite, tetrahedrite and sphalerite precipitated together with this granular/subhedral pyrite. *AJ 2* (e) (f) As rich zonations as brighter concentric rings within *ginguro* mineralised stylolites. *AJ 36b*(g) Pyrite showing different growth phases. A subhedral core has been preceded by porous development in the pyrite. Subhedral overgrowths are the final development stage of the pyrite grain. *Abbreviations: HVB= Hydrothermal vent breccia; adu= adularia; py= pyrite; chal= chalcopyrite; he= haematite; sphal= sphalerite; As= arsenic-rich zonations.*

Fig. 12. BSE images representing Gold mineralisation within the Twin Hills 309 epithermal deposit. (a) (b) (c) Naumannite-centred pyrite within silica vein; electrum rims the outside of pyrite and As-zonation is pronounced in the overgrowth. Note porosity in As zoned areas. *AJ 55*(d) Bladed calcite-silica replacement texture with naumannite and electrum along the length of the pyrite within a chalcedonic silica vein. *AJ 36A*(e) Naumannite-centred pyrite with later sphalerite. *AJ 55*(f) Reflected light image of pyrite with electrum; note the porosity seen in some pyrite. *AJ 6*(g) BSE image of elongate electrum grain within silica. (h) Freely disseminated electrum with minor pyrite and electrum within chalcedony silica vein. *Abbreviations: HVB= Hydrothermal vent breccia; py= pyrite; el= electrum; naum= naumannite; sphal= sphalerite; As= Arsenic rich zonations;* CO^3*= calcium carbonate.*

Fig. 13. BSE images of base metal sulphides and 'exotic' minerals within the Twin Hills 309 epithermal deposit. (a) (b) Sphalerite situated in zones of porosity in pyrite. *AJ 19*(c) Rare Earth Elements (REE) and sphalerite on pyrite rim suggesting a connection between Zn-bearing fluids and REE. *AJ 19*(d) Sphalerite overprinting apatite clast. *AJ 5*(e) Argyrodite within fractures in the silica groundmass. *AJ 60*(f) Argyrodite showing Ge-rich zones (brighter shade) and canfieldite (Sn)-rich zones (slightly darker). *AJ 60*(g) Chalcopyrite with tetrahedrite and sphalerite rims. *AJ 2*(h) Small particles of gold? (bright spots) at the contact between tetrahedrite and chalcopyrite. *AJ 2. Abbreviations: HVB= Hydrothermal vent breccia; py= pyrite; sphal= sphalerite; REE= rare earth elements; Au= gold; apt= apatite; argy= argyrodite; chalc= chalcopyrite; tetra=tetrahedrite; moly= molybdenum.*

Fig. 14. BSE images of base metal sulphides and 'exotic' minerals within the Twin Hills 309 epithermal deposit. (a) Paragenetic phases of base metals, tetrahedrite and sphalerite. Combined with Fig. 13g, h, this gives evidence a Fe-Cu rich fluid was proceeded by, Ag/Au, followed by Zn rich fluids forming sphalerite. *AJ 2*(b) (c) (d) (e) (f)'Dirty' molybdenite within stylolites, with associated pyrite and apatite. *AJ 76*(g) Pyrite within molybdenite-bearing stylolite shows more euhedral crystal faces. *AJ 76. Abbreviations: HVB= Hydrothermal vent breccia; py= pyrite; sphal= sphalerite; REE= rare earth elements; Au= gold; apt= apatite; argy= argyrodite; chalc= chalcopyrite; tetra=tetrahedrite; moly= molybdenum.*

Fig. 15. (a) (b) (c) Histograms and x y plots showing As variations in pyrite analysed by EPMA from Table 4, divided by sample and drill core. (c) shows a trend for the 2 atomic proportions of S in stoichiometry within the pyrite to be exchanged by higher concentrations of As, present as zonations as seen within the rims of the pyrite.(d) (e) show variations of Se concentration in pyrite by all samples and drill core. Higher Se in pyrite is probably due to ginguro related naumannite centered pyrite. Plots at 2 atomic unit per formula (FeS_2).

Fig. 16. Histograms and x y plots of EPMA analysis of elements within pyrite; by sample and drill core showing (a)Se by sample (b) Cu (c) and Mn. Se in pyrite is dominated by sample *AJ 65.* Part Se exchange for S at the atomic level is possible for naumannite centered pyrite of sample *AJ 64 (triangle).* Cu and Sb varies throughout the analysed pyrite.(d) (e) Plots showing Sb/S by drill core

and sample.showing strong trend to suggest S in sample AJ 75 (*circles)* to be substituting for Sb. Plots at 2 atomic unit per formula (FeS_2).

Fig. 17. Selected binary plots for elements in pyrite as measured by LA-ICPMS. Data are subdivided by sample and drill core. (a) As versus Au, showing the maximum solubility line (*i*)of Au in arsenian pyrite (*after* Reich *et al* 2005). Note that many of the data points plot below the line (i.e., Au is probably in solid solution, where as some plot above the line, reflecting submicro- to nanoscale inclusions. (b) and (c) As versus Ag, showing no correlation on the scale of the entire dataset, but two distinct sub-populations are seen, in which spots from AJ 55 and AJ 64 define a distinct higher-Ag population. (d) and (e) Sb versus As showing a broad correlation between the two elements, possibly indicating both are present in the pyrite lattice. Sb distribution in samples AJ 72, AJ 36b and AJ 38 may, however, be controlled by other factors.

Fig. 18. Selected binary plots for elements in pyrite as measured by LA-ICPMS. (a) Zn versus Mo, showing a weak correlation between the two elements. (b) Au versus Ag, showing two distinct sub-populations separated by low to high Ag values. (c) Sb versus Au, showing little correlation between the two elements. (d) Mo versus Au; there is a correlation between the two elements if the samples with naumannite inclusions (AJ 55 and AJ 64) are excluded. This excluded correlation line is shown in red. (e) Ag versus Mo – there is a pronounced correlation between the two elements if he naumannite inclusion samples are eliminated, the resulting correlation line in shown in red. (f) Co vs. Ni showing the excellent correlation between the two elements (equal Ni/Co concentrations). (g) Se versus Ag showing a near perfect correlation between the two elements. The upper end of the trend is dominated by samples AJ 55 and AJ 64 in which pyrite contains inclusions of naumannite.

Fig.19. Representative time-resolved LA-ICPMS depth profiles for pyrite showing the concentration of elements with depth. (a) Porous pyrite from a late-stage stylolite. The spectrum shows a large uranium peak with associated peaks in the profiles for Pb and Cu. (*U= uranium trend line);* Sample AJ 6. (b) Spectrum of more homogenous but less porous pyrite from late-stage stylolite; Note the high As and solid solution Au spectrum. Equal Se and Ag peaks show inclusions of naumannite. Sample AJ 6. (c) Base metal association with little Au. Sample AJ 19. Zn is present as nanoparticles of sphalerite as indicated by Zn peaks. Variation in the profile for As suggests micron-scale compositional zoning with respect to As. Note precious metals concentrations are low.

(d) (e) The profile shows high, and rather constant concentrations of Sb and As; the two elements are probably in solid solution; Sample AJ 72.

Fig 20. Representative time-resolved LA-ICPMS depth profiles for pyrite showing the concentration of elements with depth. (a) (b) The pronounced peaks on the spectra for Ag, Au and Se indicate the presence of sub-microscopic inclusions of electrum and naumannite.Samples AJ 55 and AJ 66. (c) (d) Spectrum for a spot in sample AJ 72 showing flat lines for Sb, Au and Ag, suggesting these elements are in solid solution within As-bearing pyrite.

Fig.21. (a)Distribution of selected elements throughout two different pyrite types in sample AJ 72. Analysis map by LAICPMS. Close trends are evident between Ag, Au and Sb distribution and between the distribution of As, Bi, Se and Cu distribution. Porosity development in the pyrite has some role on the remobilisation and distribution of elements. *a* in Au image marks zone of porosity in large pyrite mass. Note the depletion of high concentrations of Au and Ag with porosity development.

Fig. 22 (a) LAICPMS time-resolved depth profile of molybdenite in stylolite. Although the flat profiles suggest that most elements are in solid solution, it is suspected that these are actually present as very small nano-inclusions trapped within fractures and cleavage planes within the soft surface of molybdenite.

TABLES

TABLE ONE CATALOGUE OF SAMPLES FROM TWIN HILLS (309) USED IN THIS STUDY

Sample ID	Drill hole (THRCD)	Meter	NQM assay	Ore minerals	Gangue minerals	Ore host	Primary textures	Study methods			
								SEM	EPMA	LAICPMS	Assay
AJ 1	925	108.9	0.15		Clays	Cmb qtz	Silica	x	x		
AJ 1 (2)*	925	108.9	0.15	Sphal	Clays	Cmb qtz	Silica	x			
AJ 2	925	120.7	0.04	Tetra, Chal	REE	HTS	HTS, Py clast	x	x		
AJ 4	925	136.1	0.37	Sphal, Chal	TiO_2	HVB	Si Crackle Breccia	x	x		
AJ 5	925	139.1	0.62	Sphal	Apatite	HCB	HCB, Flu	x			
AJ 6	925	143.5	6.23	Elect, Aspy	Adul, Flu	HCB, Sty	HCB	x	x	x	
AJ 10	925						Chal qtz, Flu				x
AJ 16	925	179.9	781 (Moly)	Moly	Apatite	Sty	Si infill HVB, Spid	x		x	
AJ 17	925	178.4	2.69								x
AJ 19	921	191.3	2.15	Sphal		HVB	HCB	x		x	
AJ 21	921	192	0.85				Silicified HVB				x
AJ 32	926	137.4	5.79				Chal qtz, Cmb qtz				x
AJ 36a	926	140.6	3	Elect, Sphal, Naum	Flu	Diss silica, Sty	Cb repl, Chalc qtz	x			
AJ 36b	926	140.6	3	Elect	Flu	Diss silica, Sty	Cb repl, Chalc qtz	x		x	
AJ 37	926	140.2	3								x
AJ 38	926	141.2	10	Aspy	Apatite, Adul, Flu	Anas Silica, Sty	HCB, Anas qtz	x		x	
AJ 40	926	141.9	10				HCB				x
AJ 47	926	149.7	0.14				Remob Sediments				x
AJ 52	917	133.4	14.2			Anas Silica	HCB				x
AJ 54	917	134.6	14.2			Sty	HCB				x
AJ 55	917	139.4	25	Elect, Naum, Sphal	Adul	Sty, Chal qtz	Chal qtz, WGM	x		x	
AJ 56	917	139.7	25				Cb repl, Chalc qtz, HCB				x
AJ 59	917	143.2	2.25				Cb repl, Chalc qtz				x
AJ 60	917	145.4	3.3	Argyrodite	Car	Cmb qtz, Sty	Chalc qtz	x			
AJ 61	917	148.4	6				Cb repl, Chalc qtz				x
AJ 62	917	151.4	34	Elect, Naum	Clays	Cb repl, Chalc qtz	Cb repl, Chalc qtz	x		x	
AJ 63	917	152.5	34				Chal qtz				x
AJ 64	917	155.3	32.6	Elect, Naum	Apatite, Adul	Sty, Chal qtz	Chal qtz, WGM	x	x	x	
AJ 65	917	159.6	16.8	Aspy, Sphal, Chal	Clays, Adul	HVB	Cb repl, Chalc qtz	x	x		
AJ 66	917	163.5	3.98	Elect	Si	Diss silica	Cb repl, Chalc qtz	x	x		
AJ 67	919	130.2	19.9				HVB				x
AJ 68	919	131.5	1.24	Elect, Naum	Adul, Flu	Cb repl, Chalc qtz	Cb repl, Chalc qtz	x			
AJ 69	919	131.5	1.24	Sphal	Car, TiO_2	Sty	Chal qtz, Cmb qtz	x	x		
AJ 70	919	137.7	2.59								x
AJ 71	920	143.1	34.7	Py	Apatite, Adul, Car	Sty	Si infill HVB	x	x		
AJ 72	920	144.5	1.55	Py	Apatite, Adul, Car	Sty, Anas silica	Anas veins, Chalc qtz	x	x	x	
AJ 74	920	168.5	0.79	Elect	Hae, Apatite, Adul	Sty	HCB, Cmb qtz	x	x		
AJ 75	920	182.3	34.7	Elect, Aspy	Apatite, Adul	Sty, Comb qtz	HCB	x	x		
AJ 76	920	163.3	973 (Moly)	Moly	Hae, Car	Sty	Remob Sediments?	x		x	

Abbreviations: **Elect**=electrum, **Sphal**=sphalerite, **Tetra**=tetrahedrite, **Aspy**=arsenopyrite, **Moly**=molybdenite, **Naum**=naumannite, **Chal**=chalcopyrite, **Py**=pyrite. **Adul**=adularia, **Flu**=fluorite**, Car**=carbon, **Si**=silicification, **Hae**=haematite. **Cmb qtz**=comb quartz, **HTS**=high tensile stringer veins, **HVB**=hydrothermal vent breccia, **HCB**= hydrothermal crackle breccia, **Sty**=stylolite, **Chalc qtz**= chalcedonic quartz, **Spid**= spider veinlet, **Cb repl**=carbonate/silica replacement textures, **Anas qtz**= Anastomosing quartz veins, **Remob**=remobilised, **WGM**= weak ginguro mineralisation.

TABLE TWO

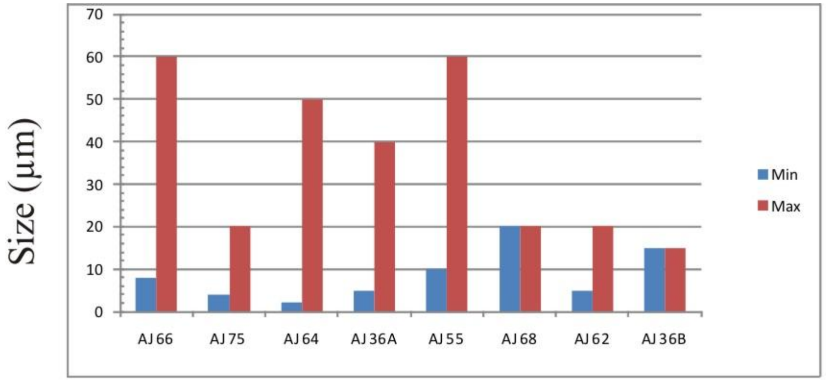

Sample	Au Grade (g/t)	Size Distribution (µm) min	max	Host	Host morphology	Macroscopic features of sample
AJ 66	3.98	8	60	Silica	Disseminated	Chalcedony with carbonate replacement textures
AJ 75	34.7	4	20		Styolitic	Hydrothermal crackle breccia with secondary brecciation textures
AJ 64	32.6	2	50	Naumannite centered Pyrite	Styolitic	chalcedonic silica vein with weak ginguro mineralisation
AJ 36A	3.0	5	40		Disseminated	chalcedonic silica vein with weak ginguro mineralisation
AJ 55	25	10	60		Disseminated	hydrothermal vent breccia chalcedonic infill with weak ginguro mineralisation
AJ 68	1.24	20	20		Disseminated	Chalcedony with carbonate replacement textures with fluorite infill
AJ 62	34	5	20		Styolitic	Chalcedonic silica vein with overprinting silica veinlets
AJ 36B	3.0	15	15	Silica	Disseminated	chalcedonic silica vein with weak ginguro mineralisation

TABLE THREE GEOCHEMICAL ASSAY RESULTS FOR SELECTED LITHOLOGIES/TEXTURES

Sample	Au (ppm)	Au rpt (ppm)	Ag (ppm)	As (ppm)	Cu (ppm)	Mo (ppm)	Pb (ppm)	Sb (ppm)	Se (ppm)	Te (ppm)	Zn (ppm)	Hand sample features
AJ 10	2.0		1.3	13	42	39	<mdl	1.1	<mdl	<mdl	21	Chalc qtz/Flu/Sty
AJ 17	0.54		1.5	143	8.0	81	8.0	6.1	<mdl	<mdl	37	SB, no quartz infill
AJ 21	1.3		1.4	142	8.0	121	8.0	6.8	<mdl	<mdl	47	SB, quartz fill, Sty
AJ 32	5.5		5.0	125	7.0	60	9.0	7.1	<mdl	<mdl	33	Chalc qtz/Comb quartz
AJ 37	0.49		1.8	103	8.0	21	10	7.2	<mdl	<mdl	33	HVB, Sty
AJ 40	15	14	10	91	6.0	110	6.0	4.6	<mdl	<mdl	35	HCB, Chalc qtz
AJ 47	0.12		1.3	212	8.0	13	11	14	<mdl	<mdl	32	FB, Sty, HTV
AJ 52	12		11	109	11	34	9.0	6.3	<mdl	<mdl	30	HVB, AV
AJ 54	0.10	0.12	3.0	108	6.0	59	9.0	6.7	2.0	<mdl	39	HVB, quartz infill, Sty
AJ 56	20	22	32	53	9.0	13	<mdl	4.7	3.0	<mdl	19	Cb, Chalc qtz, Sty,
AJ 59	5.5		31	46	7.0	7.0	<mdl	3.6	<mdl	<mdl	20	Cb, Chalc qtz
AJ 61	0.49		6.9	<mdl	5.0	x	<mdl	1.7	<mdl	<mdl	4.0	Comb quartz, Sty
AJ 63	16	16	8.7	<mdl	2.0	x	<mdl	1.8	<mdl	<mdl	3.0	Cb, Chalc qtz
AJ 67	0.76		1.3	217	9.0	13	<mdl	17	<mdl	<mdl	42	HVB
AJ 70	0.80		3.6	185	14	18	14	20	<mdl	<mdl	10	FB, quartz infill
Detection Limit	0.01	0.01	0.2	10	1.0	2	5	0.05	2	0.1	1	
Method	AAS	AAS	MS	OES	OES	OES	OES	MS	MS	MS	OES	

Abbreviations: Chalc=Chalcedony; Cb=carbonate replacement textures; Flu= fluorite; Sty= Stylolite; HVB= Hydrothermal vent breccia; HTV= High tensile veinlets; SB= Secondary breccia textures; AV= Anastomosing veins; Qtz= Quartz. Descriptions of samples are listed in (appendix I).

Repeats: Duplicate sample checks were made on samples AJ 40, AJ 54, AJ 56 and AJ 63.

Methods: AAS- 25gm lead collection fire assay, analysed by flame atomic absorption spectrometry. MS- Multi acid digest (HF, HNO3, HClO3, HCL), analysed by ICP-MS. OES- ICP (optic) atomic emission spectrometry of multi-acid digest. Genalysis Laboratory Services, Adelaide.

TABLE FOUR

TABLE FOUR SUMMARY OF EPMA RESULTS FOR PYRITE WITHIN SELECTED SAMPLES

	THRCD 917			THRCD 919	THRCD 920				THRCD 925			
	155.4 mts	159.6 mts	163.5 mts	131.5 mts	143.1 mts	144.5 mts	168.5 mts	182.3 mts	108.9 mts	120.7 mts	136.1 mts	143.5 mts
Wt.%	**AJ 64** (n=12)	**AJ 65** (n=14)	**AJ 66** (n=1)	**AJ 69** (n=24)	**AJ 71** (n=8)	**AJ 72** (n=9)	**AJ 74** (n=28)	**AJ 75** (n=44)	**AJ 1** (n=35)	**AJ 2** (n=18)	**AJ 4** (n=10)	**AJ 6** (n=7)
Cu	0.07	0.03	0.03	0.02	0.04	0.06	0.02	0.02	0.03	0.02	0.02	0.01
Mn	0.01	0.01	0.01	0.09	0.02	0.02	0.10	0.02	0.01	0.02	0.01	0.03
Fe	46.33	46.28	46.28	46.13	46.18	45.14	46.21	45.96	45.80	46.42	46.13	46.76
Co	0.00	0.00	0.00	0.00	0.00	0.00	0.00	0.00	0.00	0.00	0.00	0.00
Ni	0.01	0.02	0.02	0.01	0.01	0.02	0.03	0.02	0.02	0.02	0.02	0.02
Sb	0.05	0.02	0.02	0.03	0.03	0.24	0.02	0.07	0.18	0.02	0.01	0.01
As	1.08	0.31	0.31	0.33	0.40	0.89	0.41	0.96	1.17	0.25	1.02	0.15
S	53.19	53.55	53.55	53.95	53.29	53.05	53.19	53.36	53.25	53.78	53.53	53.90
Se	0.05	0.18	0.18	0.01	0.03	0.02	0.02	0.02	0.03	0.02	0.03	0.00
Total	100.80	100.41	100.41	100.58	100.01	99.44	99.99	100.42	100.49	100.55	100.78	100.88
a.p.f.u *												
Cu	**0.00**	**0.00**	**0.00**	**0.00**	**0.00**	**0.00**	**0.00**	**0.00**	**0.00**	**0.00**	**0.00**	**0.00**
Mn	**0.00**	**0.00**	**0.00**	**0.00**	**0.00**	**0.00**	**0.00**	**0.00**	**0.00**	**0.00**	**0.00**	**0.00**
Fe	**0.99**	**0.99**	**0.98**	**0.98**	**0.99**	**0.98**	**0.99**	**0.99**	**0.98**	**0.99**	**0.99**	**1.00**
Co	**0.00**	**0.00**	**0.00**	**0.00**	**0.00**	**0.00**	**0.00**	**0.00**	**0.00**	**0.00**	**0.00**	**0.00**
Ni	**0.00**	**0.00**	**0.00**	**0.00**	**0.00**	**0.00**	**0.00**	**0.00**	**0.00**	**0.00**	**0.00**	**0.00**
As	**0.02**	**0.01**	**0.02**	**0.01**	**0.01**	**0.01**	**0.01**	**0.02**	**0.02**	**0.00**	**0.02**	**0.00**
Sb	**0.00**	**0.00**	**0.00**	**0.00**	**0.00**	**0.00**	**0.00**	**0.00**	**0.00**	**0.00**	**0.00**	**0.00**
Se	**0.00**	**0.00**	**0.00**	**0.00**	**0.00**	**0.00**	**0.00**	**0.00**	**0.00**	**0.00**	**0.00**	**0.00**
S	**1.99**	**2.00**	**2.00**	**2.01**	**2.00**	**2.00**	**1.99**	**2.00**	**1.99**	**2.00**	**2.00**	**2.00**
Total M	**1.01**	**1.00**	**1.00**	**0.99**	**1.00**	**1.00**	**1.01**	**1.00**	**1.01**	**1.00**	**1.00**	**1.00**

TABLE FIVE

TABLE FIVE EPMA SUMMARY OF TETRAHEDRITE/TENNANTITE AND SPHALERITE GRAINS IN SELECTED SAMPLES

Tetrahedrite-tennantite

TH925: 120.7 AJ 2 — *Analysis (wt. %)*

	Ag	Cu	Pb	Fe	Mn	Zn	Cd	Sb	As	Te	Se	S	**Total**	
Mean (n=2)	0.11	34.53	0.33	1.74	<mdl	12.70	0.76	20.56	3.36	<mdl	<mdl	26.28	100.39	
													% Tetr	**% Tenn**
Formula a.p.f.u = 29	0.01	8.61	0.03	0.47	-	3.24	0.01	2.71	0.71	-	-	13.10	79.3	20.6

Sphalerite

TH917: 163.5 AJ 66 — *Analysis (wt. %)*

	Ag	Cu	Pb	Fe	Mn	Zn	Bi	Sb	As	Cd	Te	Se	S	**Total**
Mean (n=3)	<mdl	0.39	0.10	2.54	<mdl	62.4	0.09	<mdl	0.02	0.07	0.01	0.04	33.5	99.17
Formula a.p.f.u = 2*	-	0.01	0.00	0.04	-	0.93	0.00	-	0.00	0.00	0.00	0.01	1.02	2.01

TH919: 131.5 AJ 69 — *Analysis (wt. %)*

	Ag	Cu	Pb	Fe	Mn	Zn	Bi	Sb	As	Cd	Te	Se	S	**Total**
Mean (n=2)	<mdl	0.35	0.13	4.41	0.03	59.81	0.15	<mdl	<mdl	0.05	<mdl	0.06	33.30	98.32
Formula a.p.f.u = 2*	-	0.01	0.00	0.08	0.00	0.90	0.00	-	-	0.00	-	0.01	1.02	2.01

TH925: 108.9 AJ 1 — *Analysis (wt. %)*

	Ag	Cu	Pb	Fe	Mn	Zn	Bi	Sb	As	Cd	Te	Se	S	**Total**
Single analysis (n=1)	<mdl	0.07	0.13	3.06	0.00	61.55	0.25	0.02	0.04	0.12	0.02	<mdl	33.37	98.62
Formula a.p.f.u = 2*	-	0.00	0.00	0.05	0.00	0.92	0.00	0.00	0.00	0.00	0.00	-	1.02	2.00

TH925: 120.7 AJ 2 — *Analysis (wt. %)*

	Ag	Cu	Pb	Fe	Mn	Zn	Bi	Sb	As	Cd	Te	Se	S	**Total**
Mean (n=2)	0.13	5.41	0.92	3.98	<mdl	55.37	0.20	0.10	0.05	0.46	<mdl	<mdl	32.60	99.24
Formula a.p.f.u = 2*	0.00	0.08	0.00	0.07	-	0.83	0.00	0.00	0.00	0.00	-	-	1.00	2.00

# denotes calculated atomic proportion per formula unit at 29 a.p.f.u, solid solution series for tetrahedrite-tennantite $(Cu,Ag)_{10}$ $(Fe,Zn)_2$ $(Sb,As)_4$ S_{13}. * denotes calculated atomic proportion per formula unit at 2 a.p.f.u for sphalerite (ZnS).

TABLE SIX

TABLE SIX EPMA/SEM* ANALYTICAL RESULTS FOR SELECTED ELECTRUM GRAINS

	THRCD 917					**THRCD 920**			**THRCD 925**
	AJ 62	**AJ 64**		**AJ 66**		**AJ 74**	**AJ 75**		**AJ 6**
	151.4 mts* (n=1)	155.3 mts (n=5)	155.3 mts* (n=5)	163.5 mts (n=3)	163.5 mts* (n=1)	168.5 mts* (n=1)	182.3 mts (n=3)	182.3 mts* (n=3)	143.5 mts (n=2)
Au	64.99	58.02	61.50	59.82	64.99	62.30	70.37	76.21	66.25
Ag	35.01	43.68	36.33	41.65	35.01	29.13	30.73	23.79	34.78
Cu		0.03		0.00			0.02		0.01
Hg		0.40		0.27			0.28		0.12
Bi		0.20		0.18			0.17		0.14
Te		0.05		0.05			0.05		0.06
Total		**102.4**		**102.0**			**101.6**		**101.36**
MeanAu/(Ag+Au) 2 a.p.f.u		0.42		0.44			0.56		0.51
Host of Electrum	Sty, WGM	CS,Cb blade		CS,Cb blade		Sty, HCB	HQI, SB		Qtz, Sty, Fluorite

* Analysis results from Phillips XL30 SEM with EDAX

Abbreviations: **Sty**=stylolite, **WGM**=weak ginguro mineralsation, **CS**= chalcedonic silica, **Cb blade**= Carbonate/silica replacement textures, **HCB**= Hydrothermal crackle breccia, **HQI**= Hydrothermal quartz infill textures, **SB**= secondary breccia textures, **Qtz**= Quartz. .* indicates analysis by SEM EDAX, counts to 55 seconds.

TABLE SEVEN

TABLE SEVEN SUMMARY OF SEM (EDAX) ANALYSIS OF ARGYRODITE GRAINS

THRCD 917 145.4 mts					
AJ 60	**1**	**2**	**3**	**4**	**mean**
Wt.%	**canfieldite**		**argyrodite**		
Ag	64.4	72.7	73.6	73.6	**73.6**
Sn	6.2	2.0	3.7	1.5	**2.6**
Ge	2.1	6.9	5.7	6.9	**6.3**
Se	10.7	0.80	2.6	4.4	**3.5**
Te	6.1	<mdl	<mdl	<mdl	**<mdl**
S	10.4	17.7	14.4	13.6	**14.0**
Total	100.0	100.0	100.0	100.0	**100.0**
Formulae (calculated to 15 a.p.f.u.)					
Ag	**7.547**	**7.505**	**8.030**	**8.056**	**8.043**
Sn	0.658	0.186	0.370	0.149	**0.260**
Ge	0.372	1.059	0.920	1.119	**1.019**
sum Ge+Sn	**1.030**	**1.245**	**1.290**	**1.268**	**1.279**
Se	1.710	0.113	0.389	0.659	**0.524**
Te	0.607	0.000	0.000	0.000	**0.000**
S	4.106	6.137	5.292	5.016	**5.154**
sumS+Se+Te	**6.423**	**6.250**	**5.681**	**5.675**	**5.678**
% argyrodite	36.2	85.1	71.3	88.2	**79.8**
% canfieldite	63.8	14.9	28.7	11.8	**20.2**
%Ag8(Ge,Sn)S6	63.9	98.2	93.1	88.4	**90.8**
%Ag8(Ge,Sn)Se6	26.6	1.8	6.9	11.6	**9.2**
%Ag8(Ge,Sn)Te6	9.5	0.0	0.0	0.0	**0.0**

all analysis with Phillips XL30 with EDAX. Analysis @L 55secs

TABLE EIGHT

TABLE EIGHT Sample	Au(ppm)	Ag(ppm)	Se(ppm)	As(ppm)	Mo(ppm)	Te(ppm)	Bi(ppm)	Sb(ppm)	Zn(ppm)	Pb(ppm)	Tl (ppm)	Cu(ppm)	Co(ppm)	Ni(ppm)	Pyrite Morphology	Ore host	Spot Positions
	SUMMARY OF TRACE ELEMENTS WITHIN PYRITE (LA-ICPMS)																
THRCD 917 **AJ 55**																	
Mean (n=26)	28	16956	1700	3504	245	1.9	1.0	61	84	39	11	317	26	49	Granular/Subhedral (porous centres)	Silica	porous, OG,
S.D	43	46084	3992	4273	612	2.2	1.1	83	204	47	26	499	23	42			
Min	0.33	20	13	28	1.4	0.45	0.06	0.26	0.76	0.17	0.04	4.0	2.4	0.45			
Max	198	226575	19398	16974	2194	7.0	3.8	282	614	165	116	2026	91	171			
AJ 64																	
Mean (n=21)	44	5871	823	9809	94	4.8	0.33	285	24	33	31	202	10	22	Granular/Subhedral (porous centres)	As Sty	OG, Porous, CC
S.D	58	11901	1871	7389	296	7.4	0.30	451	75	21	54	238	19	23			
Min	1.2	58	35	1269	0.29	0.86	0.09	0.77	0.66	6.6	0.2	32	0.29	0.95			
Max	261	49286	8187	24172	1370	30	0.90	1638	316	62	192	1080	85	68			
THRCD 920 **AJ 72**																	
Mean (n=25)	25	128	76	9370	535	2.7	2.2	3861	57	142	545	538	113	122	Framboidal, Subhedral	HVB, Sty, Silica	OG, CR
S.D	25	85	77	11388	587	2.9	2.8	1867	86	178	244	567	239	139			
Min	0.44	3.1	6	2781	1.3	0.40	0.16	18	1.8	2.7	22	10	2.5	4.5			
Max	120	327	368	55820	2864	12	8.9	8309	317	771	1244	2293	1121	547			
AJ 76																	
Mean (n=11)	2.7	32	22	3737	805	0.63	1.4	175	24	123	34	127	38	36	Granular/ Euhedral/Subhedral	Mo Sty	OG, CC
S.D	3.2	29	22	3939	1578	0.19	1.1	173	24	101	35	85	37	29			
Min	0.05	1.1	3.6	366	5.2	0.41	0.05	14	2.6	8.3	0.87	17	0.63	2.4			
Max	11	79	59	13486	5312	0.91	3.1	617	75	350	94	274	129	87			
THRCD 921 **AJ 19**																	
Mean (n=12)	2.8	7.2	10	1062	48	-	0.44	13	138	39	11	43	11	13	Granular/ Subhedral (Sphalerite zoned grains)	HVB	CC, CR, OG
S.D	3.3	3.5	5.9	1138	70	-	0.19	9	429	16	10	18	6.4	6.4			
Min	0.17	0.75	2.3	120	0.30	0.00	0.05	0.36	3.9	5.6	2.3	4.9	1.4	2.6			
Max	10	14	19	3215	241	0.00	0.71	31	1501	71	38	66	22	26			
THRCD 925 **AJ 6**																	
Mean (n=14)	3.5	27	30	4693	168	1.4	1.5	77	17	90	8.5	128	39	65	Framboidal, Lamellar, Subhedral	HVB, As Sty, Silica	OG, Porous, CR
S.D	3.0	17	40	3172	409	-	1.1	64	31	53	7.7	62	52	82			
Min	0.49	7.0	3.8	337	2.3	1.4	0.17	8.0	0.64	21	1.0	23	1.4	1.8			
Max	10	70	148	11309	1570	1.4	3.9	251	121	225	28	227	182	311			
THRCD 926 **AJ 36b**																	
Mean (n=5)	44	12	19	25182	83	-	0.12	75	3.5	13	6.7	21	1.8	11	Granular/Subhedral (zoned grains, porous)	As/Elec Sty	OG, CR
S.D	25	8.7	-	4375	146	-	-	22	2.0	11	4.4	14	1.4	7.6			
Min	17	5.3	19	18500	2.3	0.00	0.12	60	1.3	2.8	2.9	4.1	0.32	3.1			
Max	85	26	19	30456	343	0.00	0.12	113	4.8	32	14	43	3.0	22			
AJ 38																	
Mean (n=13)	1.8	13	6.9	19890	10	-	0.25	142	2.2	11	11	16	0.91	6.7	Granular/Subhedral	As Sty	OG, CC
S.D	1.6	6.9	5.9	7644	17	-	0.14	70	2.0	7.1	3.1	11	1.6	5.3			
Min	0.08	3.5	2.8	6464	2.0	0.00	0.05	90	0.79	1.5	7.1	3.2	0.09	0.57			
Max	5.5	24	15	33596	64	0.00	0.47	317	6.2	25	17	38	6.0	14			

Abbreviations: As=arsenic; Mo=molybdenite; Elect=electrum; Sty=stylolite; HVB=hydrothermal vent breccia; OG= overgrowth, CC=central core of grain, CR=cluster rims (spot within clusters of minute pyrite); P=porous.

TABLE NINE

Molybdenum

AJ 16

THRCD 925

179.9 mts TABLE NINE SUMMARY OF LAICPMS ANALYSIS OF MOLYBDENITE

	Au(ppm)	Ag(ppm)	Se(ppm)	As(ppm)	Mo(ppm)	Te(ppm)	Bi(ppm)	Sb(ppm)	Zn(ppm)	Pb(ppm)	Cu(ppm)	Co(ppm)	Ni(ppm)	W (ppm)	Re (ppm)	Tl (ppm)	U (ppm)
Mean (n=15)	0.50	7988	229	5291	599400	8.2	7.8	4686	64	2210	166	15	22	759	15	5044	6.6
S.D	0.31	987	29	493	0.00	1.2	0.89	446	29	304	30	7.0	11	180	5.1	509	3.9
Min	0.29	5985	186	4934	599400	6.3	6.4	4116	31	1663	128	7.6	15	479	6.6	3632	2.0
Max	1.4	10175	295	6890	599400	11	10	5683	159	2772	258	33	55	1037	23	5676	13

CAPTIONS TO TABLES

Table 1. List of samples from Twin Hills investigated in this study. The table also gives drill core location, depth in drill core, the main ore minerals seen, the main macroscopic (hand sample) textures and the study methods used for each sample.

Table 2. Summary of minimum and maximum sizes of electrum seen in samples analysed. The table also shows NQM assay grades for the sampled interval, the host situation of electrum and macroscopic features often seen in hand sample.

Table 3. Results for geochemical assays of selected lithological targets. Hand sample features are stated.

Table 4. Summary of EPMA analytical results within selected pyrite grains. Sample numbers, associated drill core with depth (mts) are given. Arsenic results are highlighted in red. Analysis is given in wt.% and *atomic proportion per formula unit (a.p.f.u.) calculated for FeS_2.

Table 5. Summary of EPMA analysis of tetrahedrite and sphalerite in selected samples from the Twin Hills 309 epithermal deposit. Fe in sphalerite is at low to moderate concentrations.

Table 6. Summary of EPMA analysis for electrum. Drill core and depth given, along with textural setting situation of electrum as seen by SEM imagery. Au/(Ag+Au) indicates gold proportion of electrum.

Table 7. SEM-EDAX analyses of argyrodite within quartz vein wall of sample AJ 60. Results confirm the presence of compositions corresponding to both argyrodite and canfieldite.

Table 8. Summary of selected element concentrations within pyrite, as measured by LA-ICPMS. Concentrations are given in parts per million (ppm). A summary of pyrite morphology, pyrite host and pyrite LAICPMS analytical spot position is given in the last columns. Pyrite types have been described in section 4.2.2.

Table 9. LA-ICPMS analytical data for molybdenite in sample AJ 16. Remarkably high Ag levels are present. These are believed to be present as nano-inclusions rather than in the sulphide lattice. The Re content of the molybdenite is quite low.

APPENDIX I

LOCATION DESCRIPTIONS AND REASONS BEHIND SAMPLED ZONES.

- *Core photographs of samples are shown in adjoining figures relative to drill core I.D.*
- *Conclusions for the reasons behind the specific samples are written in italics.*

THRCD 917

AJ 52: 133.4 mts

This sample was taken for assay. Core logging is misleading if this zone is either the 4.26g/t Au interval or the 14.2 g/t Au interval. The sample is a matrix supported Hydrothermal pebble vent breccia, with overprinting tension stringer and anastomosing veins.

AJ 54: 134.6 mts

Textures featuring a poly breccia sample showing sub angular clast supported breccia. Brecciated clasts contain multiple lithologies, these include, medium grained arenites, mudstones and previous chalcedonic silicas that have been brecciated and now are part of the hydrothermal breccia host. Minor stylolitic contacts surround clast boundaries.

AJ 55: 139.4 mts

A section of banded silica textures are represented in this sample, and also contains good examples of the so called ‘spider veinlets’. Core logging describes these veins as being rebrecciated. Comb quartz textures suggest the silica has infiltrated a more open space. Argillic and Pervasive silica alteration are present, with also pyritisation, disseminated thoughout. This sample was taken from a zone of high grade and hence is of interest.

AJ 56: 139.7 mts

Chalcedonic silica has replaced bladed calcite. Minor stylolitic bands follow the replaced calcite blade boundaries. Assays show this interval contains up to 25 g/t Au within it, thus has been assayed.

AJ 59: 143.2 mts

This sample was assayed due to the chalcedonic silica infilling replacing calcite. This can be clearly seen on the back of the core.

AJ 60: 145.4 mts

This sample is of a chalcedonic silica vein showing no strong indications of replacement of bladed calcite textures. A black stylolitic band at the vein wall could be the reason why in this interval we see the Au grade jump to 3.3 g/t.

AJ 61: 148.4 mts

Sample shows a chalcedonic silica vein, replacing bladed calcite. Minor stylolitic mineralisation has developed at one end of the drill core. NQM’s original assay over meter intervals throughout this intersection of the drill core show it was carrying 6 g/t Au. This representative sample was taken from the silica vein from within this meter.

AJ 62: 151.4 mts

This sample represents all of the similar described textures as to AJ 61, with exception that weak ‘ginguro’mineralisation is present. A polished block was made to analyse sulphides seen within the chalcedonic silica where it replaces calcite. This was taken from within a high grade zone (34 g/t Au).

AJ 63: 152.5 mts

This sample was also taken from the same high grade interval as sample AJ 62. An assay was made to check the influence of weak ginguro mineralisation on grade. Textures present include bladed calcite,replaced by, chalcedony.

AJ 64: 155.3 mts

This marks the beginning of a massive silica vein in the drill core. This extends more or less over a distance of 5 meters. This also contains high grade Au zones (34g/t). Potassic alteration occurs in the clasts adjacent the vein. Silicification and pyritisation occurs throughout the matrix. The veining also displays weak ginguro mineralisation.

AJ 65: 159.6 mts

This interesting sample includes an angular fragment of a sub- rounded pebble quartz arenite. This is a foreign clast that has fallen in from the edge of the collapsing Twin Hills sub- basin. The silica is a dark chalcedony replacing calcite bladed textures. This sample is also from an interval of high grade (16.8 g/t Au).

AJ 66: 163.5 mts

This sample is also from a high grade Au zone. It is taken from near the end of the 5 metre section of the silica vein mentioned in AJ 64 above. This vein is more crystalline in texture with chalcedony replacing calcite.

THRCD 919

AJ 67: 130.2 mts

This sample is of the matrix supported hydrothermal vent breccia. Some of the fragments within the pyritised matrix are of previous silica veins. This sample was taken for assaying because of the nature of the fragments and the matrix relative to a high grade Au intersection of 19.9 g/t Au.

AJ 68: 131.5 mts

This sample is from 130.5 meters. It contains a large chalcedonic silica vein, showing a late minor fluorite infill. The silica displays crystalline, comb quartz textures. Stylolitic textures are also presented well. Assays from NQM show grade for this ore is high at 19.9 g/t Au. Specks of Au were observed on adjacent quartered drillcore. It was sampled based on the assumption adjacent core contained visible gold as well.

AJ 69: 131.5 mts

This sample, at 131.5 meters, was from within an interval that NQM assays show to contain Au grades to 1.24 g/t. Although being adjacent to the 19.9 g/t Au section of sample AJ 68, visible Au was present within this sample. It was of interest because of this observation and the similar nature of the adjacent richer Au grades.

AJ 70: 137.7 mts

This sample was for assaying the geochemistry within an intensly silicified zone of the hydrothermal vent breccia host and the relevance of this texture to Au grade.

THRCD 920

AJ 71: 143.1 mts

Pervasive silicification throughout and locally, chloritic alteration have affected the rims of the clasts situated within the matrix. The rims show sharp, sutured contacts, probably formed through the disequilibrium of fluids in the matrix to the clasts. This is also in an interval showing high grade Au at (34 g/t). This grade, however might be situated in an adjacent silica vein which were not sampled.

AJ 72: 144.5 mts

Sample AJ 72 is a part of tension stringer vein sets. Pyritisation adjacent and overprinting these quartz stringers has taken place. This core interval is low in Au, grade being only 1.55 g/t Au. The sample was taken from a fluidised, well bedded, very fine grained mudstone. Clearly, this is overprinted with chalcedony and a later comb quartz vein. These textures are in association with hydrothermal crackle infill breccias, which were present in the next interval (145-146 meters).

AJ 74: 168.5 mts

This sample is within an interval where Au grade drops to 0.79 g/t. stylolite development against a silica vein created enough interest to compare it with the stylolites within high grade zones of silica. Host lithology is a brecciated very fine grained siltstone. Adularisation is present. *The conclusions after this research confirmed the stylolites that developed parallel to the vein are barren in Au and commonly showed carbonaceous matter and titanium dioxides.*

AJ 75: 182.3 mts

This sample was taken from within the high grade interval of 34 g/t Au at 182.3 metres. Lithology is a brecciated very fine grained mudstone. Quartz textures were logged by NQM as ‘spider’ veinlets and blebs of Au were visible. *BSE imagery showed two stylolite present. 1) Carbonaceous/titanium stylolite. 2) Electrum rich stylolite with granular pyrite showing porosity. The latter was responsible for the high Au grades.*

AJ 76: 163.3 mts

NQM assays stated very high Mo (973 g/t) within this drillcore interval. Ag content is moderate (8.2 g/t) whilst Au concentrations are low. The trends for high Mo to Ag ratios lead to suggest there is reason to suspect a Mo-Ag correlation. *We conclude Molybdenum mineralisation within the breccia is locally developed nearby paleo-sinter blocks within the breccia. The pyrite within the sinter blocks is organic derived evident on the framboidal/attol textures and contain high amounts of Tl, Sb, Ag and Au in solid solution.*

THRCD 921

AJ 19: 191.3 mts

There is a jump in the Au grade (up to 2.15g/t) in this interval . It includes part of the hydrothermal crackle breccia silica infill. *The pyrite in this sample is hosted within the Hydrothermal vent breccia associated with sphalerite inclusions. Au concentrations within the pyrite average 2.8 ppm. The base metal associations with low Au concentrations are considered to be a late phase of mineralisation.*

AJ 21: 192.0 mts

This was taken for assaying. The hand specimen shows a probable fault boundary situated between adjacent sandstone lithologies, defined by well developed bedding. Sub angular fragments with post quartz infill are shown adjacent to the sandstone.

THRCD 925: 108.9mts

AJ 1

This was the first sample taken from the drillcore used in this study. Within the crystalline comb quartz an unknown silver mineral was observed whilst sampling. Two blocks made from this section were intended for further analysis of the unknown silver mineral. The host lithology is a very fine mudstone or tuff. *The unknown visible mineral was lost during transport of the samples. Sphalerite is common in vughs of the comb quartz. The host lithology was concluded to be a volcanic rock based on widespread pyritisation of alike size phenocrysts.*

AJ 2: 120.7 mts

Pyrite is shown to be present within the clasts of this sample. Fine, high tensile veinlets also with pyritisation are also observed and seem to have some connection to the clasts. *Pyrite with base metals of tetrahedrite and chalcopyrite overprint the high tensile veinlets.*

AJ 4: 136.1 mts

This sample was taken because of the relation between pyrite and high tensile veinlets. *Base metals of sphalerite and minor chalcopyrite were again observed with these type of veinlets.*

AJ 5: 139.1 mts

This sample represents a fluorite infilled hydrothermal crackle breccia. *Base metals of sphalerite and chalcopyrite were present with granular pyrite.*

AJ 6: 143.5 mts

This sample represents the fluorite rich hydrothermal crackle breccia. NQM assays state Au Grade was 6.23 g/t. Because of NQM's results it was sampled. *BSE images revealed the Au was situated in late generation stylolites with arsenopyrite.*

AJ 10

An assay was made of the fluorite infill overprinting the chalcedonic silica vein. Chalcedony has replaced calcite blades. A later stylolite has cut alongside the fluorite infill. *Assay returned a low 2.0 g/t Au. There likely is a common connection between stylolites that run parallel to veins and the carbonaceous/titanium dioxide stylolites.*

AJ 16: 179.9 mts

This sample from 179.9 meters, was taken because of NQM's high Molybdenum assay of 781 ppm. Molybdenite was clearly seen in a vugh in the back of the drill core within stylolitic banded textures. *LA-ICPMS spot analysis was undertaken on the molybdenite showing it contained high traces of Tl and Ag. The molybdenite is considered to be a collector of 'junk' passing fluids.*

AJ 17: 178.4 mts

Fine crosscutting veinlets with sulphides cut across the host rock. An assay of this was taken.

THRCD 926

AJ 32: 137.4 mts

An assay was taken of the chalcedony silica with later comb quartz where Au grades were stated by NQM to be 5.79 g/t Au. *Results show these silica veins to contain moderate Au levels of 5.5 g/t.*

AJ 36a AJ 36b: 140.6 mts

This sample represents a chalcedonic silica vein with calcite replacement textures. Weak ginguro mineralisation is portrayed on the downhole side of the vein. On the uphole side of are the silica replaced calcite blades. NQM assay results show Au grade from this point in the drillcore is rising

(3> g/t Au). To represent the differences between the ginguro mineralisation and the silica/chalcedonic vein, two blocks were prepared from this section labelled AJ 36a and AJ 36b. *Only sample AJ 36b was analysed by LA-ICPMS. These results show high Au concentrations in solid solution with As. BSE images for sample AJ36a revealed pyrite,electrum and minor naumannite were precipitated distinctly along the replaced bladed calcite.*

AJ 38: 141.2 mts

Crystalline anastomosing vertical /fluorite silica veins are present within the drill core sample, which represents a high grade interval of 10 g/t Au. Sample includes some high tensile veining. *LAIPCMS spot analysis results from pyrite within this sample showed a high As content buy a very low Au concentration.*

AJ 40: 141.89 mts

An assay has been made from this dirty grey mix of chalcedonic silica with minor calcite replacement textures. Adjacent wall rocks suggest a part of the hydrothermal crackle breccia. Sulphides are seen at the vein and clast edges. *Results from assay show these textures within the crackle breccia are indicative of high grade ore.*

AJ 47: 149.7 mts

An assay has been taken from this heavily silicified sample. The host rock has undergone intense immobilisation. Interest is in the type of geochemistry with these textures. *Assays returned very low Au values of 0.12 g/t.*

THRCD 917

AJ 52

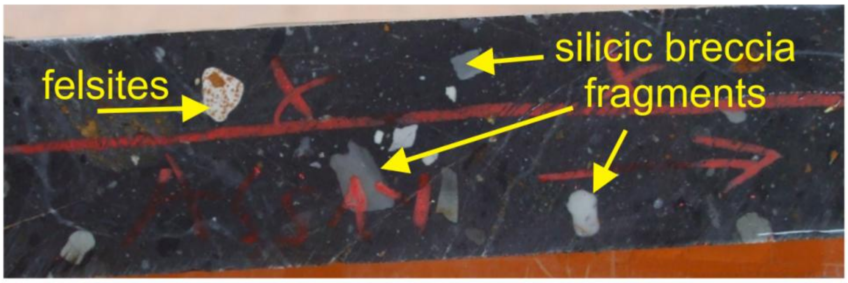

AJ 54

AJ 55

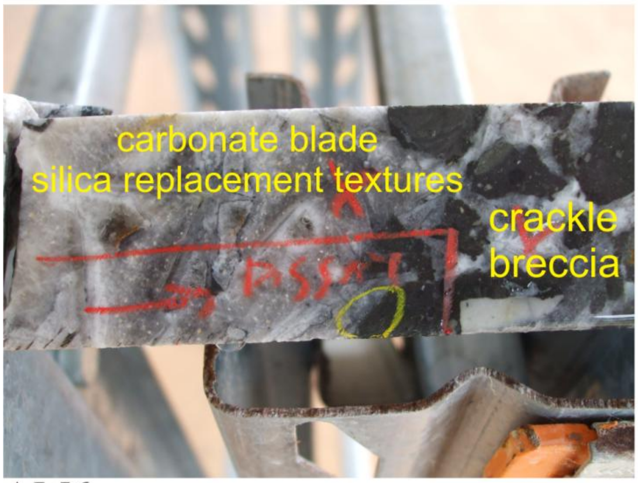

AJ 56

AJ 59

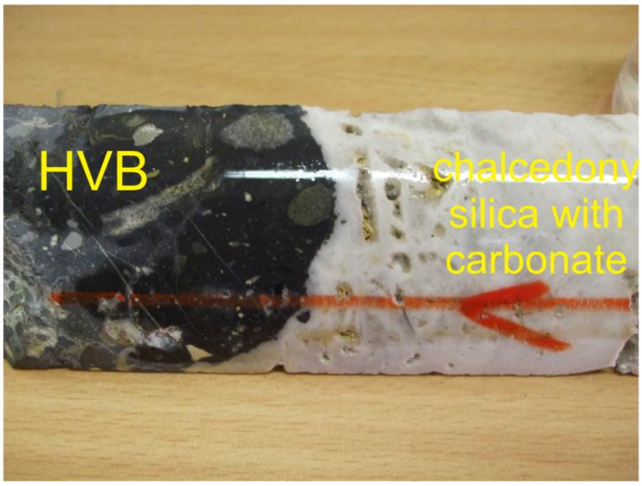

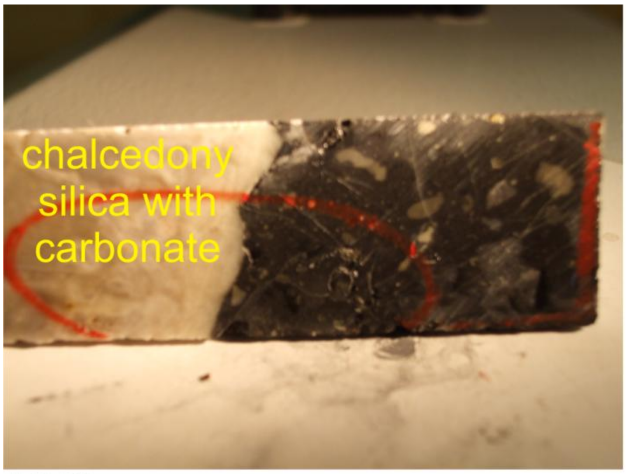

AJ 60

AJ 63

AJ 61

AJ 64

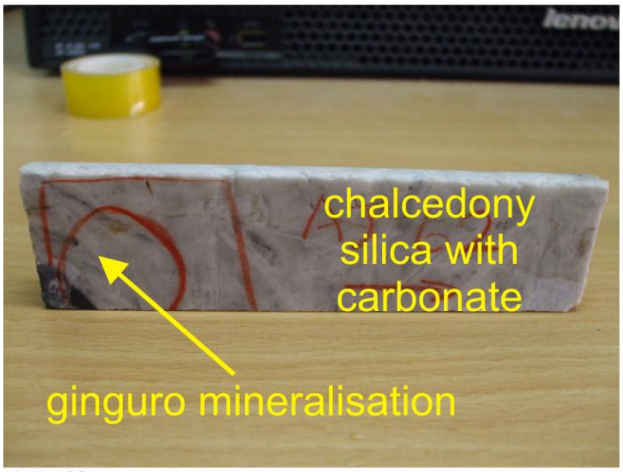

AJ 62

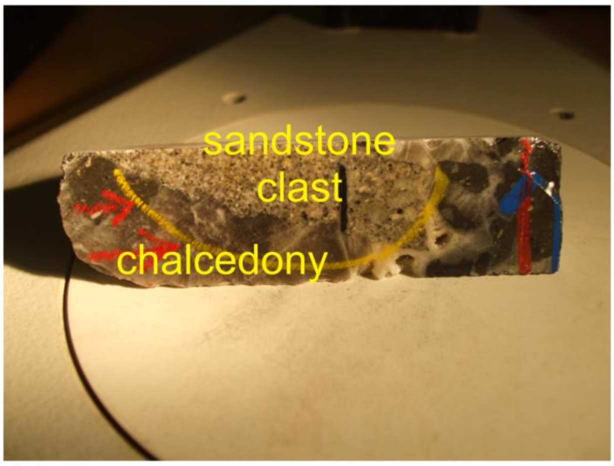

AJ 65

AJ 66

THRCD 919

AJ 67

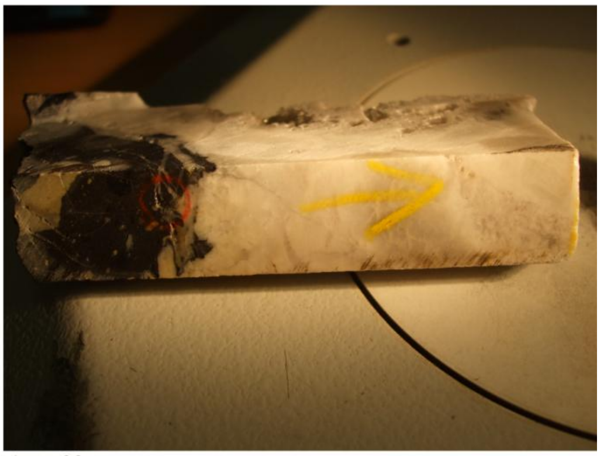

AJ 69

AJ 68

AJ 70

THRCD 920

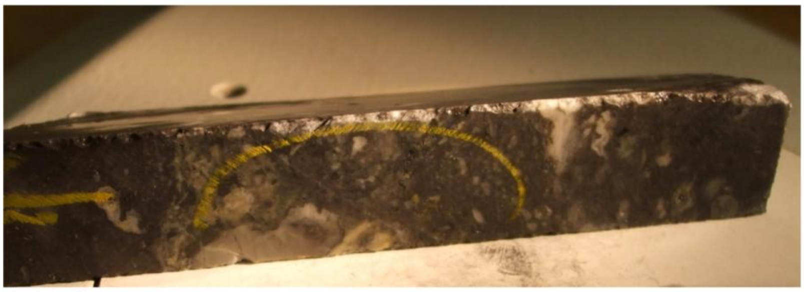

AJ 71

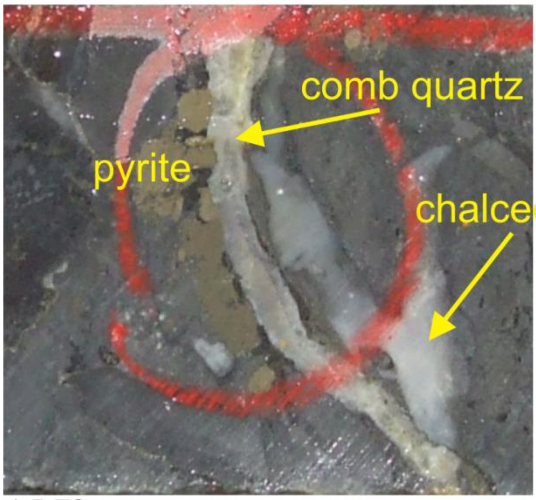

AJ 72

AJ 76

AJ 74

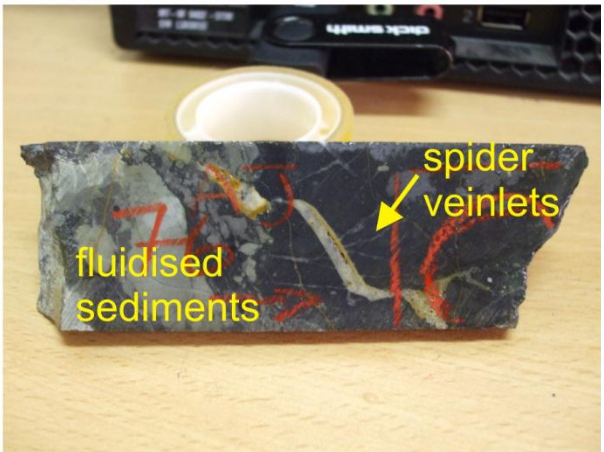

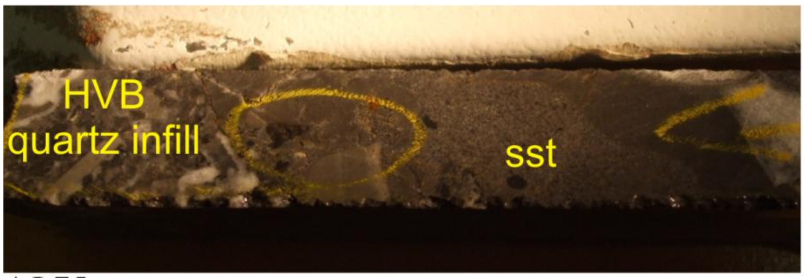

AJ 75

THRCD 921

AJ 19

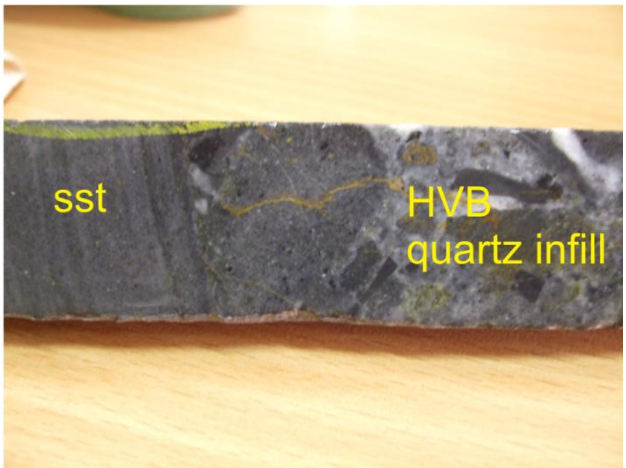

AJ 21

THRCD 925

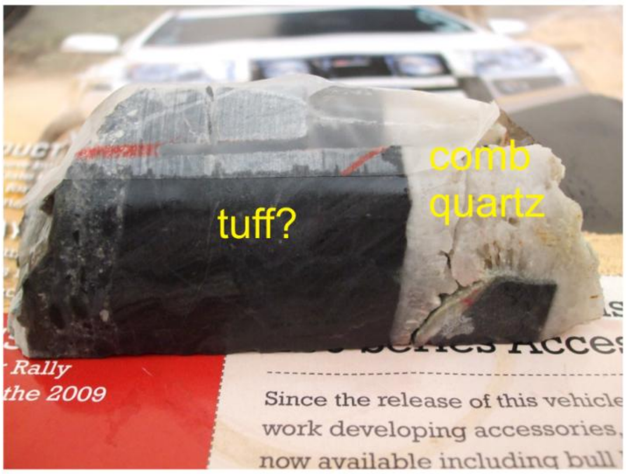

AJ 1

AJ 4

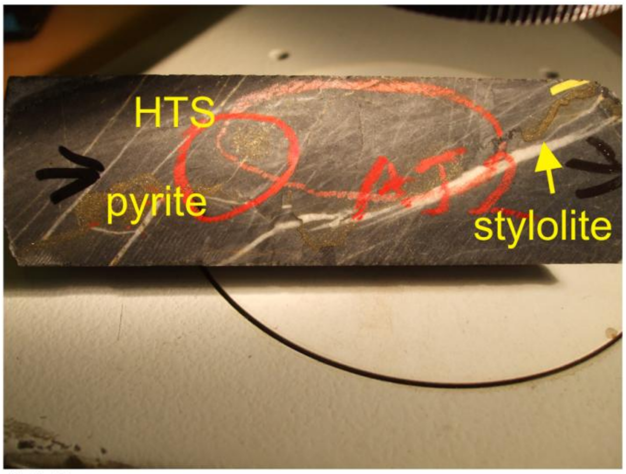

AJ 2

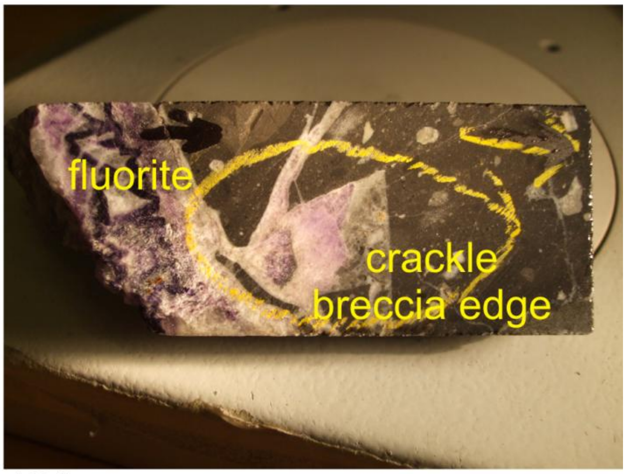

AJ 5

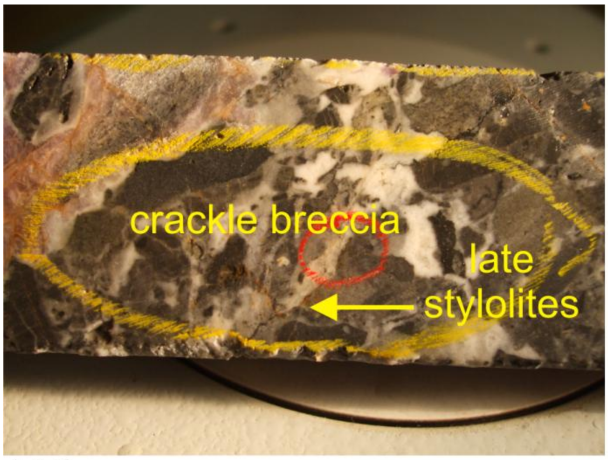

AJ 6

AJ 10

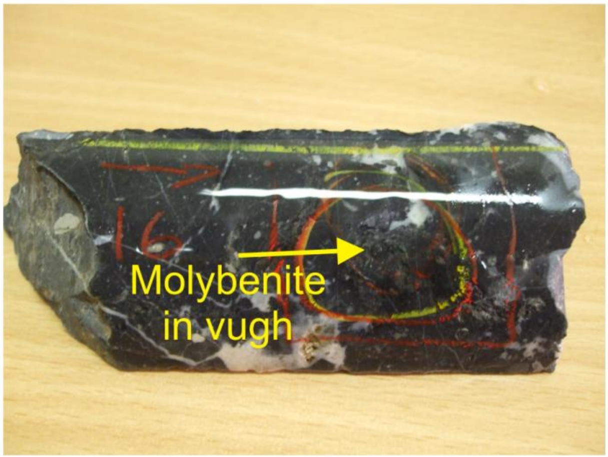

AJ 16

THRCD 926

AJ 32

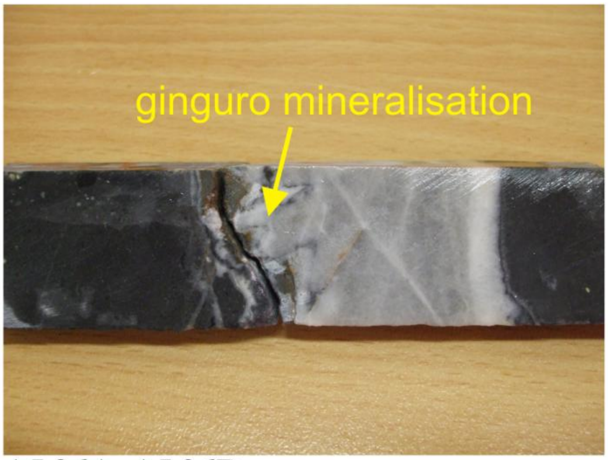

AJ 36A, AJ 36B

AJ 38

AJ 40

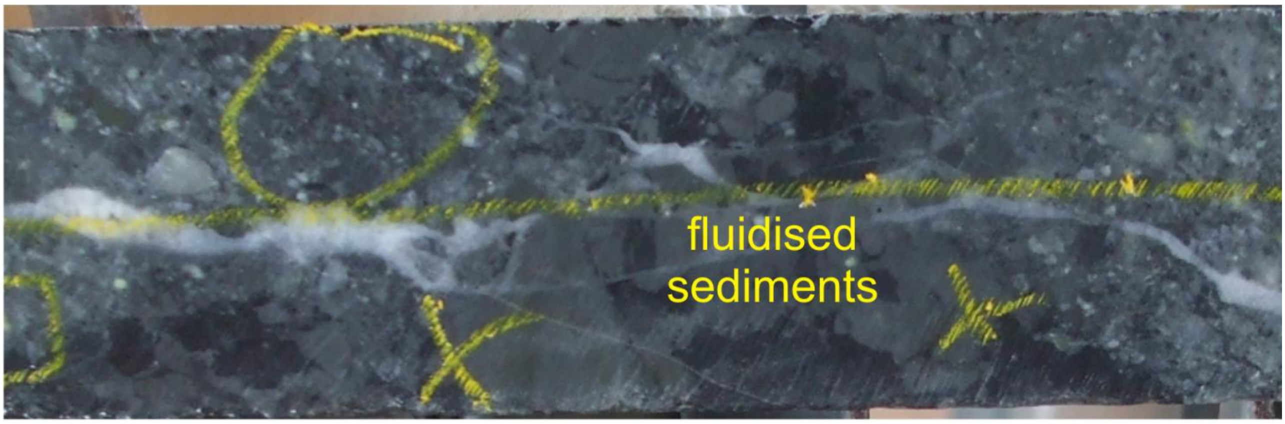

AJ 47

APPENDIX II

Drill logs of

sampled Drill cores

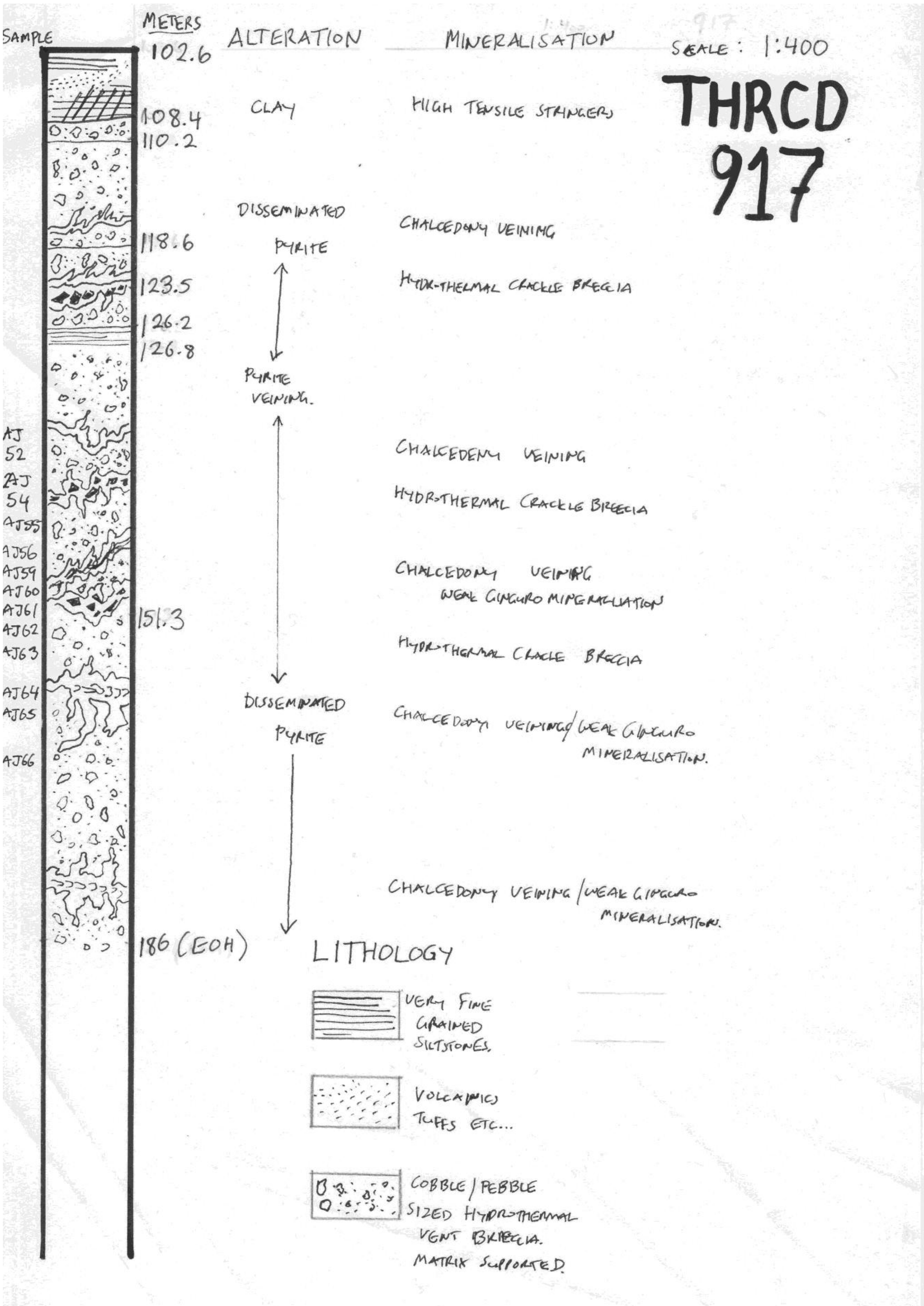
SAMPLE
METERS
ALTERATION
MINERALISATION
SCALE : 1:400
THRCD
917
102.6
108.4
110.2
118.6
123.5
126.2
126.8
151.3
186 (EOH)
CLAY
HIGH TENSILE STRINGERS
DISSEMINATED
PYRITE
CHALCEDONY VEINING
HYDR-THERMAL CRACKLE BRECCIA
PYRITE
VEINING.
AJ
52
AJ
54
AJ55
AJ56
AJ59
AJ60
AJ61
AJ62
AJ63
AJ64
AJ65
AJ66
CHALCEDONY VEINING
HYDROTHERMAL CRACKLE BRECCIA
CHALCEDONY VEINING
WEAK GINGURO MINERALISATION
HYDROTHERMAL CRACKLE BRECCIA
DISSEMINATED
PYRITE
CHALCEDONY VEINING/WEAK GINGURO
MINERALISATION.
CHALCEDONY VEINING / WEAK GINGURO
MINERALISATION.
LITHOLOGY
VERY FINE
GRAINED
SILTSTONES.
VOLCANICS
TUFFS ETC...
COBBLE / PEBBLE
SIZED HYDROTHERMAL
VENT BRECCIA.
MATRIX SUPPORTED.

SAMPLE | METERS | ALTERATION | MINERALISATION

SCALE 1: 400

THRCD 919

Sample	Meters	Alteration	Mineralisation
	113		
	117		
		FLUIDISED	HYDROTHERMAL CRACKLE BRECCIA
	129		
AJ 67		DISSEMINATED PYRITE	CHALCEDONY VEINING
AJ68			
AJ69			
AJ70	139		WEAK GINGURO MINERALISATION
			CHALCEDONY VEINING FLUORITE WEAK GINGURO MINERALISATION
			HYDROTHERMAL CRACKLE BRECCIA
			HIGH TENSILE STRINGER VEINS
	177.4 (EOH)		

LITHOLOGY

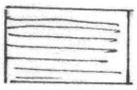

FINE GRAINED SILTSTONES

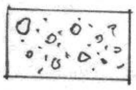

PEBBLE – COBBLE SIZED
MATRIX SUPPORTED
HYDROTHERMAL VENT BRECCIA

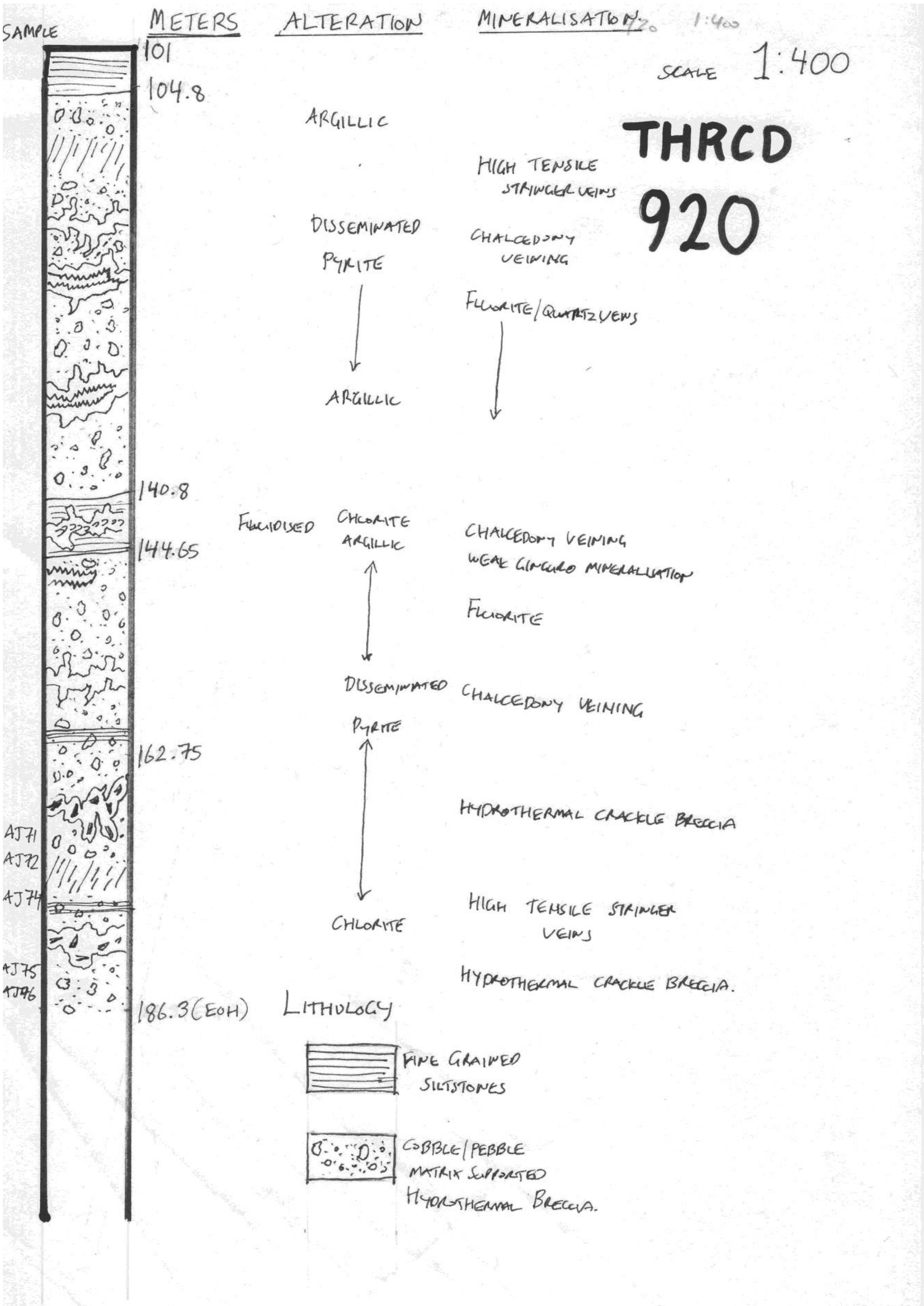
SAMPLE
METERS
ALTERATION
MINERALISATION
1:400
SCALE 1:400
THRCD 920
101
104.8
ARGILLIC
HIGH TENSILE STRINGER VEINS
DISSEMINATED PYRITE
CHALCEDONY VEINING
FLUORITE/QUARTZ VEINS
ARGILLIC
140.8
FLUIDISED
CHLORITE ARGILLIC
144.65
CHALCEDONY VEINING
WEAK GINGURO MINERALISATION
FLUORITE
DISSEMINATED PYRITE
CHALCEDONY VEINING
162.75
HYDROTHERMAL CRACKLE BRECCIA
AJ71
AJ72
AJ74
CHLORITE
HIGH TENSILE STRINGER VEINS
AJ75
AJ76
HYDROTHERMAL CRACKLE BRECCIA.
186.3 (EOH)
LITHOLOGY
FINE GRAINED SILTSTONES
COBBLE/PEBBLE MATRIX SUPPORTED HYDROTHERMAL BRECCIA.

SAMPLES | METERS | ALTERATION | MINERALISATION

AJ 19

AJ 21

204.2

213.6

222.53 (EOH)

FLUIDISED.

↑

DISSEMINATED PYRITE

↓

CHALCEDONY VEINING

HYDROTHERMAL CRACKLE BRECCIAS

HIGH TENSILE STRINGER VEINS.

SCALE 1:400

THRCD 921

LITHOLOGY

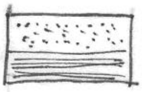

FINE GRAINED SANDSTONE / SILTSTONES

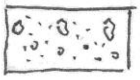

PEBBLE SIZED MATRIX SUPPORTED HYDROTHERMAL VENT BRECCIA

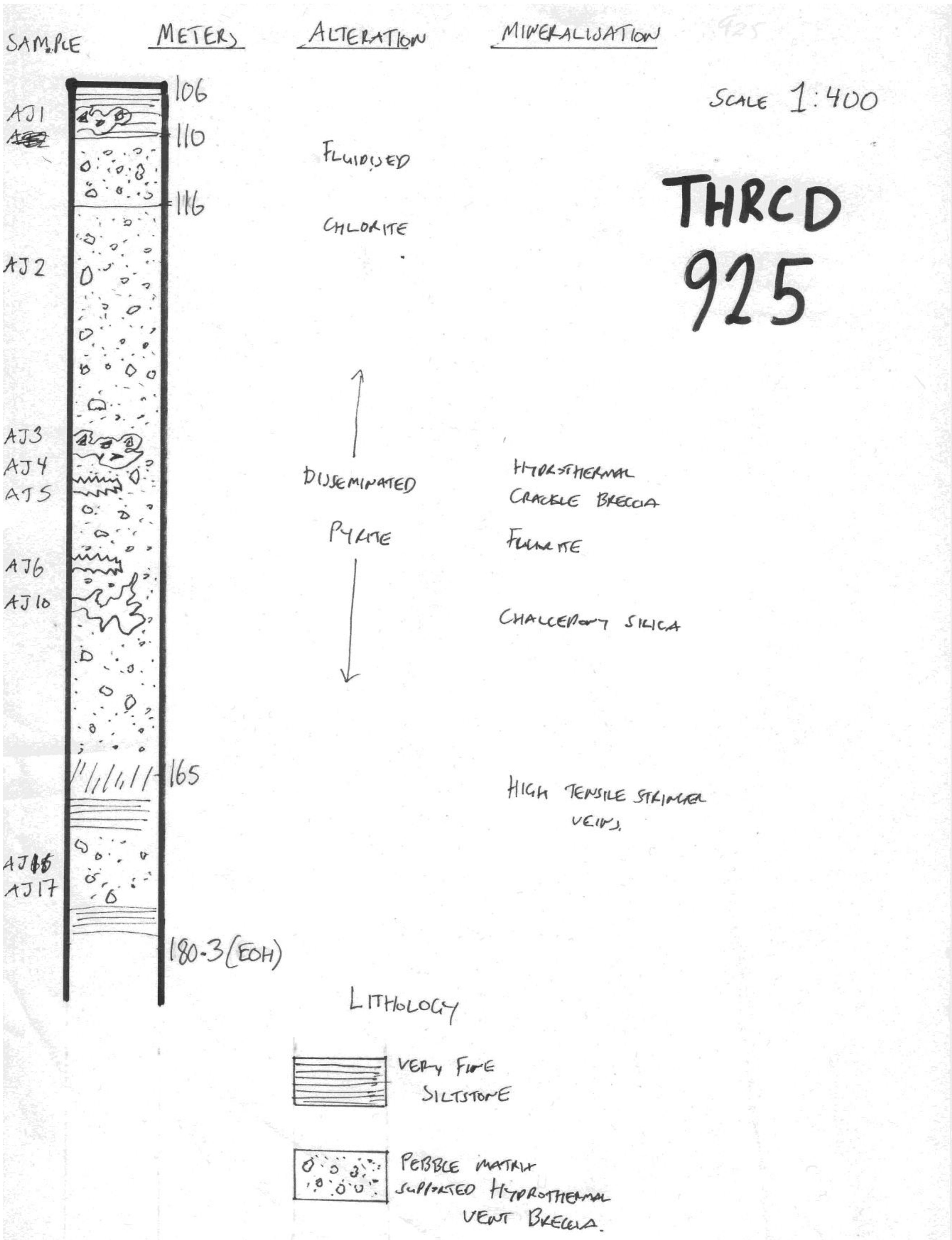
SAMPLE
METERS
ALTERATION
MINERALISATION
SCALE 1:400
THRCD
925
AJ1
AJ2
AJ3
AJ4
AJ5
AJ6
AJ10
AJ16
AJ17
106
110
116
165
180.3 (EOH)
FLUIDISED
CHLORITE
DISSEMINATED
PYRITE
HYDROTHERMAL
CRACKLE BRECCIA
FLUORITE
CHALCEDONY SILICA
HIGH TENSILE STRINGER
VEINS.
LITHOLOGY
VERY FINE
SILTSTONE
PEBBLE MATRIX
SUPPORTED HYDROTHERMAL
VENT BRECCIA.

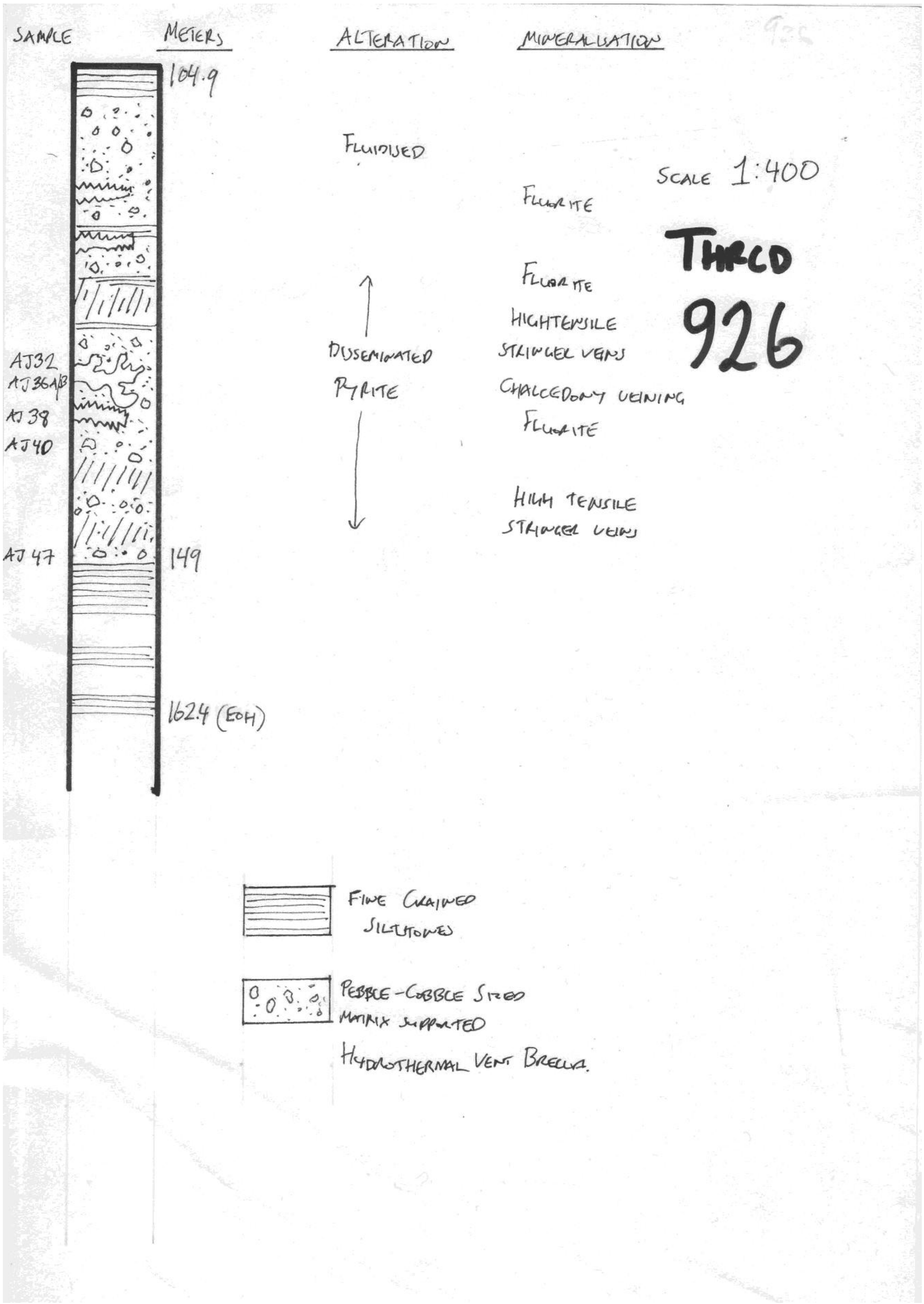
SAMPLE
METERS
ALTERATION
MINERALISATION
104.9
FLUIDISED
SCALE 1:400
FLUORITE
THRCD
926
FLUORITE
HIGHTENSILE
STRINGER VEINS
DISSEMINATED
PYRITE
CHALCEDONY VEINING
FLUORITE
HIGH TENSILE
STRINGER VEINS
AJ32
AJ36A/B
AJ38
AJ40
AJ47
149
162.4 (EOH)
FINE GRAINED
SILTSTONES
PEBBLE-COBBLE SIZED
MATRIX SUPPORTED
HYDROTHERMAL VENT BRECCIA.

APPENDIX III

EPMA analysis of Pyrite

(full dataset)

APPENDIX III ANALYSIS RESULTS FOR PYRITE (EPMA) *Total dataset*

Sample/EPMA spot position	Pyrite size (µm)	Morphology	Ore Textures	Quartz Texture	Associated Minerals	Host	Cu	Mn	Fe	Co	Ni	Sb	As	S	Se	Total
1aj2	30	Anhedral	Anhedral cluster	Comb Qtz	bitumen/carbon	Sediment/Tuff?	0.0165	0.0001	46.615	0.0001	0.0471	0.0017	0.2281	54.2158	0.0082	101.1326
1aj3	40	Anhedral	Anhedral cluster	Comb Qtz	bitumen/carbon	Sediment/Tuff?	0.0001	0.0001	46.8093	0.0001	0.0215	0.0336	0.0988	54.5388	0.0002	101.5025
1aj4	40	Anhedral	Anhedral cluster	Comb Qtz	bitumen/carbon	Sediment/Tuff?	0.0001	0.0001	46.9345	0.0001	0.0041	0.0001	0.571	53.9911	0.0014	101.5025
1aj5	70	Framboid	Fine grained cluster	Comb Qtz	bitumen/carbon	Sediment/Tuff?	0.0165	0.0034	46.8117	0.0001	0.0051	0.0705	0.3696	54.34	0.0002	101.6171
1ajl1_1	70	Anhedral	Homogenous	Comb Qtz			0.0001	0.0387	47.0583	0.0099	0.0051	0.0001	0.2774	54.8641	0.0002	102.2539
1ajl1_2	70	Anhedral	Homogenous	Comb Qtz			0.0445	0.0001	46.189	0.0001	0.0295	0.0987	2.3322	52.3711	0.0251	101.0903
1ajl1_3	70	Anhedral	Homogenous	Comb Qtz			0.0001	0.0057	47.3275	0.0001	0.0143	0.0588	0.3315	54.3182	0.0068	102.063
1ajpt23	80	Subhedral	Homogenous	Comb Qtz		QV	0.0377	0.0216	46.7974	0.0001	0.0205	0.0101	0.5499	54.3423	0.0109	101.7905
1ajpt24	80	Subhedral	Homogenous	Comb Qtz		QV	0.0001	0.0001	47.5526	0.0001	0.0174	0.005	0.3295	54.2368	0.0287	102.1703
1ajpt25	80	Subhedral	Homogenous	Comb Qtz		QV	0.0001	0.0091	46.9812	0.0001	0.0419	0.0134	1.4507	53.4826	0.0415	102.0206
1ajpt26	80	Subhedral	Homogenous	Comb Qtz		QV	0.0316	0.0001	46.2586	0.0001	0.0275	0.0134	2.308	52.8328	0.0084	101.4805
1ajpt27	60	Subhedral	Homogenous	Comb Qtz		QV	0.0001	0.0001	46.5696	0.0001	0.0001	0.052	1.7213	53.3067	0.0429	101.6929
2ajl1_1	200	Anhedral	Lamellar, overgrowth		Chalc, Tetra, Sphal	HTSV/Clast	0.0001	0.0215	47.0594	0.0001	0.0193	0.02	0.1684	53.8777	0.0002	101.1667
2ajl1_2	200	Anhedral	Lamellar, overgrowth		Chalc, Tetra, Sphal	HTSV/Clast	0.0117	0.0045	46.7443	0.0127	0.0203	0.0001	0.5753	53.8478	0.0002	101.2169
2ajl2_1	200	Anhedral	Lamellar, overgrowth		Chalc, Tetra, Sphal	HTSV/Clast	0.0246	0.0001	46.3948	0.0001	0.0071	0.0001	0.3838	54.1578	0.0365	101.0049
2ajl2_2	200	Anhedral	Lamellar, overgrowth		Chalc, Tetra, Sphal	HTSV/Clast	0.0632	0.0079	47.0558	0.0001	0.0285	0.02	0.0817	54.2304	0.0002	101.4878
2ajl3_1	200	Anhedral	Lamellar, overgrowth		Chalc, Tetra, Sphal	HTSV/Clast	0.0001	0.009	46.5155	0.0001	0.0326	0.0918	0.2355	54.151	0.0002	101.0358
2ajl3_2	200	Anhedral	Lamellar, overgrowth		Chalc, Tetra, Sphal	HTSV/Clast	0.0234	0.157	47.0949	0.0028	0.0193	0.0001	0.0187	54.1145	0.0002	101.4309
2ajl4_1	200	Anhedral	Lamellar, overgrowth		Chalc, Tetra, Sphal	HTSV/Clast	0.0129	0.0001	46.9365	0.0001	0.0001	0.0133	0.1286	54.2663	0.0351	101.393
2ajl4_2	200	Anhedral	Lamellar, overgrowth		Chalc, Tetra, Sphal	HTSV/Clast	0.0187	0.0001	46.7372	0.0001	0.0071	0.0401	0.0398	54.2912	0.0002	101.1345
2ajl5_1	200	Anhedral	Lamellar, overgrowth		Chalc, Tetra, Sphal	HTSV/Clast	0.0012	0.0068	46.787	0.0152	0.0336	0.02	0.4096	53.8977	0.0002	101.1713
2ajl5_2	200	Anhedral	Lamellar, overgrowth		Chalc, Tetra, Sphal	HTSV/Clast	0.0001	0.0068	45.8782	0.0065	0.0001	0.0001	0.576	51.5945	0.0096	98.0719
2ajl6_1	200	Anhedral	Lamellar, overgrowth		Chalc, Tetra, Sphal	HTSV/Clast	0.0257	0.0135	46.8694	0.0218	0.0001	0.0001	0.9557	53.4889	0.0532	101.4284
2ajl7	200	Anhedral	Lamellar, overgrowth		Chalc, Tetra, Sphal	HTSV/Clast	0.0526	0.0001	45.4682	0.0001	0.0001	0.0518	0.1828	53.8923	0.0002	99.6482
2ajpt2	40	Anhedral	Porous centre		Chalc, Tetra, Sphal	HTSV/Clast	0.0328	0.0034	45.787	0.0001	0.0001	0.0033	0.1497	53.6354	0.0337	99.6455
2ajpt3	40	Anhedral	Porous centre		Chalc, Tetra, Sphal	HTSV/Clast	0.028	0.0001	45.3367	0.0001	0.0001	0.0517	0.0105	52.4395	0.0002	97.8669
2ajpt4	40	Anhedral	Porous centre,overgrowth		Chalc, Tetra, Sphal	HTSV/Clast	0.0082	0.0102	46.2419	0.0001	0.0355	0.045	0.0291	54.1335	0.0901	100.5936
2ajpt5	40	Anhedral	Porous centre		Chalc, Tetra, Sphal	HTSV/Clast	0.0187	0.0305	46.0389	0.0073	0.0416	0.05	0.2552	53.9308	0.0002	100.3732
2ajpt6	40	Anhedral	Porous centre,overgrowth		Chalc, Tetra, Sphal	HTSV/Clast	0.0245	0.0226	46.4579	0.0001	0.0183	0.03	0.1691	53.9554	0.0002	100.6781
2ajpt7	40	Anhedral	Porous centre,overgrowth		Chalc, Tetra, Sphal	HTSV/Clast	0.0245	0.0045	46.1658	0.0001	0.0366	0.0001	0.164	54.0512	0.0296	100.4764
4ajl8_1	40	Subhedral	Porous centre overgrowth			HVB	0.0153	0.0001	46.3584	0.0001	0.0267	0.0084	0.1081	54.251	0.0366	100.8047
4ajl8_2	40	Subhedral	Porous centre overgrowth			HVB	0.0035	0.0001	46.1284	0.0001	0.0001	0.0554	2.267	53.0725	0.0417	101.5688
4ajl8_3	40	Subhedral	Porous centre overgrowth			HVB	0.0001	0.0001	46.7013	0.0047	0.0133	0.0001	1.3733	53.451	0.0373	101.5812
4ajl8_4	40	Subhedral	Porous centre overgrowth			HVB	0.0001	0.0001	45.7033	0.0001	0.0001	0.0017	0.8377	53.2656	0.0178	99.8265
4ajpt63	40	Subhedral	Porous centre overgrowth			HVB	0.0507	0.0148	46.4169	0.0001	0.0001	0.0118	0.3254	54.1863	0.0002	101.0063
4ajpt64	40	Subhedral	Porous centre overgrowth			HVB	0.0271	0.0001	46.8512	0.0001	0.0349	0.0001	0.2736	54.1207	0.0002	101.308
4ajpt65	40	Subhedral	Porous centre overgrowth			HVB	0.046	0.0001	46.1067	0.0001	0.0646	0.0151	0.3351	53.8639	0.0191	100.4507
4ajpt66	30	Anhedral	Anhedral cluster			HVB	0.0364	0.0182	45.4898	0.0001	0.0031	0.0001	1.5474	52.8165	0.0648	99.9764
4ajpt67	30	Anhedral	Anhedral cluster			HVB	0.0118	0.0001	46.0512	0.0001	0.0492	0.0118	0.2817	53.9784	0.0204	100.4047
4ajpt68	30	Anhedral	Anhedral cluster			HVB	0.0187	0.0204	45.5008	0.0001	0.0448	0.0251	2.8816	52.337	0.0518	100.8803

Sample/EPMA spot position	Pyrite size (µm)	Morphology	Ore Textures	Quartz Texture	Associated Minerals	Host	Cu	Mn	Fe	Co	Ni	Sb	As	S	Se	Total
64l1_1	60	Anhedral	Anhedral fractured			Stylolite	0.4231	0.0011	46.3727	0.0001	0.0457	0.035	0.09	53.9649	0.0149	100.9475
64l1_2	60	Anhedral	Anhedral fractured			Stylolite	0.175	0.0202	45.1271	0.0001	0.0141	0.1578	2.9408	52.0024	0.1321	100.5696
64l1_3	60	Anhedral	Anhedral fractured			Stylolite	0.1279	0.0001	46.2277	0.0001	0.0001	0.0001	2.0446	52.5023	0.0152	100.9181
64l2_1	120	Anhedral	Porous centre, overgrowth				0.0001	0.0485	46.479	0.0001	0.0001	0.0001	1.192	53.46	0.0478	101.2277
64l2_3	120	Anhedral	Porous centre, overgrowth				0.007	0.0282	46.7792	0.0001	0.0001	0.07	0.0659	53.5959	0.0324	100.5788
64pt1	120	Anhedral	Porous centre			Stylolite	0.0001	0.0001	47.296	0.0001	0.0001	0.0183	0.0468	53.7373	0.0217	101.1205
64pt2	120	Anhedral	Porous centre			Stylolite	0.0222	0.0305	46.4528	0.0001	0.0001	0.0701	0.0467	53.9954	0.0323	100.6502
64pt3_1	50	Subhedral	Porous centre, overgrowth			Stylolite	0.042	0.0147	46.0637	0.0001	0.0001	0.0001	1.4345	52.9772	0.0069	100.5393
64pt4	120	Subhedral	Porous centre, dark zoned centre			Stylolite	0.0269	0.0001	47.2814	0.0011	0.001	0.0001	0.0928	54.2633	0.0622	101.7289
64pt5	120	Subhedral	Porous centre, zoned edge			Stylolite	0.0001	0.0001	46.1206	0.0107	0.0394	0.0001	3.0659	51.9012	0.0182	101.1563
64pt6	120	Subhedral	Porous centre, zoned edge			Stylolite	0.0258	0.0001	45.4565	0.0001	0.0397	0.0001	0.0002	52.9165	0.2045	98.6435
64pt7	120	Subhedral	Porous centre, zoned edge			Stylolite	0.0001	0.0203	46.341	0.0001	0.0001	0.1946	1.9082	53.0224	0.0523	101.5391
65aj1	80	Anhedral	Anhedral cluster	Chalcedony, Comb Quartz	Arsenopyrite	HVB	0.0435	0.0295	47.0521	0.0001	0.0001	0.0772	0.2464	54.3808	0.0177	101.8474
65aj2	20	Anhedral	Anhedral cluster	Chalcedony, Comb Quartz	Arsenopyrite	HVB	0.0341	0.0057	47.4662	0.0001	0.0001	0.0001	0.6918	53.809	0.0631	102.0702
65aj4	40	Framboid	Fine grained cluster	Chalcedony, Comb Quartz	Arsenopyrite	HVB	0.0377	0.0068	46.9374	0.0001	0.0184	0.0218	0.2181	54.055	0.0449	101.3402
65ajl6_1	60	Anhedral	Anhedral cluster	Chalcedony, Comb Quartz	Arsenopyrite	HVB	0.0577	0.0034	45.6734	0.0001	0.0215	0.0421	0.6	53.5775	0.0723	100.048
65ajl6_2	60	Anhedral	Anhedral cluster	Chalcedony, Comb Quartz	Arsenopyrite	HVB	0.0047	0.0308	46.1627	0.0001	0.0287	0.0067	0.1918	53.4272	0.0844	99.9371
65ajpt47	60	Anhedral	Anhedral cluster	Chalcedony, Comb Quartz	Arsenopyrite	HVB	0.0106	0.0001	45.1869	0.0001	0.0297	0.1024	0.1166	51.8521	0.1688	97.4673
65ajpt48	60	Anhedral	Anhedral cluster	Chalcedony, Comb Quartz	Arsenopyrite	HVB	0.0106	0.0001	45.0779	0.0001	0.0594	0.0017	1.1342	52.5659	0.0082	98.8581
65ajpt49	60	Anhedral	Anhedral cluster	Chalcedony, Comb Quartz	Arsenopyrite	HVB	0.0012	0.041	46.3356	0.0001	0.0113	0.0168	0.0941	53.8315	0.289	100.6206
65ajpt50	60	Anhedral	Anhedral cluster	Chalcedony, Comb Quartz	Arsenopyrite	HVB	0.0001	0.0001	45.969	0.0001	0.0001	0.0001	0.1574	53.3426	0.4694	99.9389
65ajpt51	60	Anhedral	Anhedral cluster	Chalcedony, Comb Quartz	Arsenopyrite	HVB	0.0578	0.0114	46.3685	0.0001	0.0615	0.0505	0.2629	54.0395	0.0613	100.9135
65ajpt52	60	Anhedral	Anhedral cluster	Chalcedony, Comb Quartz	Arsenopyrite	HVB	0.0001	0.0137	46.6368	0.0001	0.0266	0.0001	0.069	53.7513	0.4792	100.9769
65ajpt53	60	Anhedral	Anhedral cluster	Chalcedony, Comb Quartz	Arsenopyrite	HVB	0.1648	0.0001	46.5184	0.0001	0.0184	0.0001	0.4831	53.1542	0.3558	100.695
65ajpt54	40	Anhedral	Anhedral cluster	Chalcedony, Comb Quartz	Arsenopyrite	HVB	0.0425	0.0182	46.2146	0.0001	0.0174	0.0001	0.0556	53.9148	0.1153	100.3786
65ajpt55	40	Anhedral	Anhedral cluster	Chalcedony, Comb Quartz	Arsenopyrite	HVB	0.0001	0.0001	46.317	0.0141	0.001	0.0001	0.0749	53.985	0.2616	100.6539
66ajpt1	15	Anhedral	Grain in silica	Comb Qtz	electrum	QV	0.0595	0.0011	45.3665	0.0001	0.0233	0.0001	1.2377	53.3123	0.0341	100.0347

Sample/EPMA spot position	Pyrite size (µm)	Morphology	Ore Textures	Quartz Texture	Associated Minerals	Host	Cu	Mn	Fe	Co	Ni	Sb	As	S	Se	Total
69aj1	120	Subhedral	Subhedral centre,porous pyrite			HVB	0.0374	0.0001	46.5937	0.0001	0.0142	0.0383	0.0164	53.8299	0.0002	100.5303
69aj2	25	Anhedral	Mn?core zoned			Stylolite	0.0105	0.1752	45.1128	0.0001	0.002	0.0001	0.1948	52.8685	0.0002	98.3642
69aj3	25	Anhedral	Mn?core zoned, overgrowth			Stylolite	0.0047	0.0001	46.2034	0.0001	0.0478	0.2201	0.0893	53.9851	0.0215	100.5721
69pt10	25	Anhedral	Subhedral centre,porous pyrite				0.0198	0.0158	46.0326	0.0037	0.0283	0.0233	1.8501	53.5526	0.0002	101.5264
69pt11	20	Subhedral	centre, Homogeneous				0.0526	0.2801	45.6529	0.0001	0.0001	0.0534	0.187	54.0926	0.0002	100.319
69pt12	20	Subhedral	Homogenous, rim				0.028	0.1164	45.8452	0.0001	0.0071	0.0217	0.5372	54.4759	0.0002	101.0318
69pt15	25	Anhedral	Porous centre		Sphalerite	Styolite/around silica	0.0001	0.0407	46.7515	0.0063	0.0001	0.0684	0.0186	54.084	0.0337	101.0034
69pt16	25	Anhedral	Porous centre		Sphalerite	Styolite/around silica	0.0001	0.0722	46.8695	0.0025	0.0081	0.0133	0.7818	54.0208	0.0002	101.7685
69pt18	40	Euhedral	Centre Mn core?		Sphalerite	Styolite/around silica	0.0001	0.009	46.071	0.0001	0.0203	0.0217	0.0829	53.4926	0.0002	99.6979
69pt19	40	Euhedral	Mn core? Overgrowth		Sphalerite	Styolite/around silica	0.1075	0.0486	45.628	0.0001	0.0173	0.0001	0.2761	53.868	0.0081	99.9538
69pt2	120	Subhedral	Porous centre, overgrowth			HVB	0.0001	0.7269	46.3582	0.0001	0.0001	0.0167	0.4994	54.1305	0.0068	101.7388
69pt20	40	Euhedral	Mn core? Overgrowth		Sphalerite	Styolite/around silica	0.2045	0.052	45.4399	0.0073	0.0396	0.0001	0.3386	53.4396	0.0002	99.5218
69pt22	40	Anhedral	Porous centre		Sphalerite	Styolite/around silica	0.0001	0.0001	46.639	0.0001	0.0274	0.0017	0.2723	54.0377	0.0513	101.0297
69pt23	40	Anhedral	Porous centre, rim		Sphalerite	Styolite/around silica	0.0315	0.0192	46.4063	0.0001	0.0001	0.0567	0.5496	54.1265	0.0244	101.2144
69pt26	40	Subhedral	Mn core?		Sphalerite	Styolite/around silica	0.0001	0.0181	46.7226	0.0001	0.0153	0.0001	0.1387	54.9024	0.0498	101.8472
69pt27	30	Subhedral	Mn core? Overgrowth		Sphalerite	Styolite/around silica	0.0001	0.0249	45.5387	0.0036	0.0001	0.0001	0.7147	54.0076	0.0002	100.29
69pt28	30	Subhedral	Mn core? Overgrowth		Sphalerite	Styolite/around silica	0.0001	0.061	46.2736	0.0001	0.0122	0.005	0.5407	54.7957	0.0391	101.7275
69pt3	120	Subhedral	Porous centre,overgrowth			Styolite/vein edge	0.0001	0.0565	46.6053	0.0331	0.0366	0.0001	0.219	54.3784	0.0002	101.3293
69pt4	120	Subhedral	Porous centre,overgrowth			Styolite/vein edge	0.0001	0.1185	46.8111	0.0251	0.0001	0.0001	0.0903	53.9228	0.0189	100.987
69pt5	120	Subhedral	Porous centre			Styolite/vein edge	0.0001	0.1762	45.9236	0.0001	0.0001	0.0584	0.0002	53.5371	0.0002	99.696
69pt6	120	Subhedral	Porous centre			Styolite/vein edge	0.0023	0.0068	45.5643	0.01	0.0091	0.0001	0.2871	52.862	0.0338	98.7755
69pt7	20	Anhedral	porous pyrite rim?		Sphalerite	Styolite/around silica	0.0129	0.0181	46.2103	0.0001	0.0091	0.0167	0.2874	53.9423	0.004	100.5009
69pt7	20	Anhedral	centre, porous pyrite		Sphalerite	Styolite/around silica	0.0152	0.1199	45.5194	0.0001	0.0163	0.0001	0.0379	53.8064	0.0027	99.518
69pt8	20	Anhedral	porous pyrite rim?		Sphalerite	Styolite/around silica	0.0001	0.0001	46.2996	0.0001	0.0001	0.0635	0.0284	54.6286	0.0497	101.0702
69pt9	25	Anhedral	centre, porous pyrite		Sphalerite	Styolite/around silica	0.0001	0.0034	46.7571	0.0001	0.0437	0.0001	0.0002	54.2901	0.0013	101.0961
6ajl1	50	Subhedral	Homogenous, adjacent FeAsS		Arsenopyrite/Electrum		0.0001	0.0441	47.394	0.0074	0.0489	0.0001	0.0253	54.2292	0.0002	101.7493
6ajpt15	50	Subhedral	Porous pyrite, overgrowth		Arsenopyrite/Electrum		0.0001	0.0916	46.813	0.0001	0.0001	0.0001	0.1718	54.1083	0.0068	101.1919
6ajpt16	50	Subhedral	Porous pyrite, overgrowth		Arsenopyrite/Electrum		0.0047	0.0001	46.986	0.0001	0.0102	0.0433	0.0002	53.6671	0.0002	100.7119
6ajpt17	50	Subhedral	Porous pyrite, overgrowth		Arsenopyrite/Electrum		0.0001	0.0181	46.3487	0.0001	0.0265	0.0001	0.3027	53.7179	0.0002	100.4144
6ajpt5	30	Anhedral	porous pyrite		Arsenopyrite/Electrum		0.0503	0.0001	46.2257	0.0001	0.0041	0.005	0.4912	54.0884	0.0203	100.8852
6ajpt8	30	Anhedral	porous pyrite rim		Arsenopyrite/Electrum		0.0507	0.0353	45.845	0.0001	0.0001	0.0488	0.1767	53.1803	0.034	99.371

Sample/EPMA spot position	Pyrite size (µm)	Morphology	Ore Textures	Quartz Texture	Associated Minerals	Host	Cu	Mn	Fe	Co	Ni	Sb	As	S	Se	Total
71ajl7_1	100	Anhedral	Fine grained cluster		titanium/carbon	Stylolite	0.0177	0.0125	46.318	0.0001	0.0001	0.0286	0.2425	53.4674	0.0002	100.0871
71ajl7_2	100	Anhedral	Fine grained cluster		titanium/carbon	Stylolite	0.0625	0.0603	45.9659	0.0001	0.0226	0.0319	0.2483	52.9496	0.0002	99.3414
71ajl7_3	100	Anhedral	Fine grained cluster		titanium/carbon	Stylolite	0.013	0.0501	45.784	0.0001	0.0318	0.0001	0.1427	52.7246	0.0654	98.8118
71ajl7_4	100	Anhedral	Fine grained cluster		titanium/carbon	Stylolite	0.0459	0.0001	46.8718	0.0001	0.0123	0.0235	0.9218	53.4272	0.0002	101.3029
71ajpt58	30	Anhedral	overgrowth		titanium/carbon	Stylolite	0.0483	0.025	46.8072	0.0183	0.0225	0.0286	0.4286	54.2047	0.0423	101.6255
71ajpt60	20	Anhedral	overgrowth		titanium/carbon	Stylolite	0.066	0.0001	46.5316	0.0001	0.001	0.0151	0.2746	53.6144	0.0002	100.5031
71ajpt61	100	Anhedral	Fine grained cluster		titanium/carbon	Stylolite	0.0471	0.0068	45.336	0.0001	0.0113	0.0471	0.7486	52.7678	0.0588	99.0236
71ajpt62	100	Anhedral	Fine grained cluster		titanium/carbon	Stylolite	0.0412	0.0295	47.0169	0.0001	0.0225	0.1443	0.1606	54.3504	0.0002	101.7657
72aj1	1000	Anhedral	Brecciated cluster		apatite	QV	0.053	0.008	45.766	0.0001	0.0205	0.2791	0.1715	54.0182	0.0002	100.3166
72aj2	1000	Anhedral	Brecciated cluster		apatite	QV	0.0576	0.0125	44.8137	0.0001	0.0001	0.5086	0.4004	52.6679	0.0109	98.4718
72aj3	1000	Anhedral	Brecciated cluster		apatite	QV	0.0175	0.0001	46.1715	0.0001	0.0001	0.0217	2.8552	52.4877	0.0602	101.6141
72aj5	60	Anhedral	Vein wall growth, zoned		Carbon	Stylolite, QV	0.0259	0.0001	44.8079	0.0001	0.042	0.1734	0.8538	53.2789	0.0191	99.2012
72ajl4_1	80	Anhedral	vein wall growth, fine grained cluster				0.0518	0.0308	44.8984	0.0001	0.0307	0.1735	0.5984	53.4026	0.0204	99.2067
72ajl4_2	80	Anhedral	vein wall growth, fine grained cluster				0.0576	0.0387	44.5613	0.0001	0.0286	0.0993	1.1699	52.9044	0.0055	98.8654
72ajl4_3	80	Anhedral	vein wall growth, fine grained cluster				0.145	0.0947	44.0943	0.0001	0.0001	0.2579	0.4483	53.1791	0.0312	98.2507
72ajl4_4	80	Anhedral	vein wall growth, fine grained cluster				0.0881	0.0001	44.1394	0.0273	0.0041	0.4663	1.3229	51.1545	0.0248	97.2275
72ajl5_3	200	Anhedral	Brecciated cluster		apatite	QV	0.0071	0.0068	47.0501	0.0001	0.0524	0.0286	0.1184	53.7877	0.0287	101.0799
74aj1	40	Euhedral	porous centre			Stylolite	0.0118	0.0001	46.7308	0.0001	0.0133	0.0001	0.1018	52.9849	0.0002	99.8431
74aj2	40	Euhedral	porous centre			Stylolite	0.0001	0.0001	46.8502	0.0001	0.0409	0.0001	1.0507	51.9453	0.0097	99.8972
74aj3	40	Euhedral	porous centre			Stylolite	0.0059	0.0979	45.4409	0.0327	0.0072	0.0001	0.3663	54.3165	0.0311	100.2986
74aj4	40	Euhedral	porous centre			Stylolite	0.0318	0.0001	46.3556	0.0001	0.044	0.0001	0.0824	54.2003	0.0002	100.7146
74aj6	40	subhedral	Subhedral cluster			Stylolite	0.0177	0.0353	45.9998	0.0001	0.0001	0.0286	0.1546	53.8439	0.0002	100.0803
74ajpt1	40	Euhedral	porous centre			Stylolite	0.0001	0.0318	46.8355	0.0001	0.0001	0.0001	0.39	53.9212	0.0423	101.2212
74ajpt10	60	Anhedral	Porous centre,overgrowth			Stylolite	0.0001	0.0001	46.5273	0.0001	0.0001	0.0001	0.0473	51.1084	0.0002	97.6837
74ajpt11	60	Anhedral	Porous centre,overgrowth			Stylolite	0.0931	0.0399	43.9425	0.0001	0.0001	0.0624	0.3364	53.7866	0.0754	98.3365
74ajpt12	10	Euhedral	Euhedral cluster			Stylolite	0.0001	0.0001	46.0486	0.0001	0.0113	0.1024	0.3901	53.2869	0.0082	99.8478
74ajpt13	10	Euhedral	Euhedral cluster			Stylolite	0.0152	0.0001	45.3921	0.0001	0.0427	0.025	2.5289	49.1649	0.0002	97.1692
74ajpt14	10	Euhedral	Euhedral cluster			Stylolite	0.0483	0.008	46.1746	0.0029	0.0491	0.005	0.4092	52.6705	0.0287	99.3963
74ajpt15	10	Euhedral	Euhedral cluster			Stylolite	0.0001	0.5475	46.3549	0.0001	0.0092	0.0001	0.0415	53.9541	0.0002	100.9077
74ajpt16	10	Euhedral	Euhedral cluster			Stylolite	0.0247	0.0001	47.2674	0.0001	0.0001	0.0268	0.5123	53.7178	0.0055	101.5548
74ajpt17	10	Euhedral	Euhedral cluster			Stylolite	0.0495	0.0751	45.8466	0.0001	0.0195	0.0001	0.2216	52.6778	0.0002	98.8905
74ajpt18	10	subhedral	Subhedral cluster			Stylolite	0.0001	0.0034	45.7785	0.0001	0.1137	0.0001	0.542	53.3536	0.0055	99.797
74ajpt19	30	Subhedral	Porous centre, rim			HVB	0.0177	0.0137	46.9205	0.0148	0.0001	0.0001	0.1772	53.7515	0.0123	100.9079
74ajpt2	40	Euhedral	Porous centre			HVB	0.0317	0.0068	44.6243	0.0001	0.137	0.0723	1.1264	53.0953	0.0273	99.1212
74ajpt20	30	subhedral	Porous centre			HVB	0.0071	0.0114	46.6128	0.0001	0.0646	0.0001	0.0211	53.3105	0.0095	100.0372
74ajpt21	30	subhedral	Subhedral cluster			HVB	0.0001	0.0102	46.4454	0.0001	0.0001	0.0134	0.1044	53.8388	0.0002	100.4127
74ajpt22	30	subhedral	Subhedral cluster			HVB	0.0001	0.8361	46.0733	0.0001	0.0236	0.0001	0.3661	53.254	0.0137	100.5671
74ajpt3	40	subhedral	Porous centre			Stylolite	0.0001	0.1878	46.8958	0.0052	0.0205	0.0001	0.0373	53.9826	0.0002	101.1296
74ajpt4	40	Euhedral	Porous centre			Stylolite	0.0001	0.0136	45.5189	0.0296	0.0205	0.0117	0.3736	51.8165	0.0328	97.8173
74ajpt5	25	Anhedral	Anhedral fractured			Stylolite	0.0753	0.7749	45.4683	0.0001	0.0001	0.0001	0.6049	53.6378	0.03	100.5915

Sample/EPMA spot position	Pyrite size (µm)	Morphology	Ore Textures	Quartz Texture	Associated Minerals	Host	Cu	Mn	Fe	Co	Ni	Sb	As	S	Se	Total
74ajpt6	10	Anhedral	Anhedral cluster			HVB	0.0295	0.0934	46.5266	0.0001	0.0174	0.0387	0.1804	53.9964	0.0002	100.8827
74ajpt7	10	subhedral	Subhedral cluster			Stylolite	0.0071	0.0136	46.9704	0.0001	0.0001	0.0201	0.265	52.8576	0.0438	100.1778
74ajpt8	50	Anhedral	Porous centre,overgrowth			Stylolite	0.0001	0.0001	46.3728	0.0001	0.0001	0.0553	0.882	52.9184	0.0398	100.2687
74ajpt9	50	Anhedral	Porous centre			Stylolite	0.0332	0.0503	46.7981	0.0232	0.0432	0.0001	0.1031	54.1316	0.0002	101.183
75aj10	130	subhedral	zoned rings,overgrowth			Stylolite/QV	0.035	0.0226	46.0508	0.0089	0.0528	0.0883	1.246	53.029	0.0068	100.5402
75aj11	130	subhedral	zoned rings,overgrowth			Stylolite/QV	0.0573	0.009	46.3818	0.0001	0.0001	0.025	0.4742	54.0838	0.0189	101.0502
75aj12	130	subhedral	zoned rings,overgrowth			Stylolite/QV	0.0082	0.0192	46.5758	0.0001	0.002	0.0516	1.0343	53.6473	0.0436	101.3821
75aj13	150	Anhedral	cluster zoned			Stylolite/QV	0.0001	0.017	46.3253	0.0001	0.0295	0.0001	0.1929	53.9444	0.0229	100.5323
75aj21	15	subhedral	gold?				0.0001	0.0159	44.7228	0.0084	0.0051	0.1613	3.0492	52.3849	0.0002	100.3479
75aj3	150	Anhedral	cluster zoned				0.0186	0.0113	44.3872	0.0001	0.0001	0.391	3.4063	51.7362	0.0504	100.0012
75aj4	100	subhedral	zoned rings,overgrowth				0.0325	0.0001	44.5326	0.0001	0.0243	0.2769	3.1137	51.9174	0.0544	99.952
75aj5	100	subhedral	zoned rings,overgrowth				0.0597	0.0001	45.2417	0.0001	0.0305	0.1003	0.1658	53.1572	0.004	98.7594
75aj6	10	Anhedral	cluster zoned			Py clast	0.0328	0.0001	46.5926	0.0001	0.0184	0.0001	0.0147	54.499	0.0002	101.158
75aj8	60	subhedral	overgrowth				0.0199	0.0045	47.4476	0.0001	0.0377	0.0001	0.0945	54.0083	0.0176	101.6303
75aj9	20	Anhedral	lamellar,cluster			Organic replacement/QV	0.029	0.0686	44.8528	0.0086	0.0363	0.1413	2.7752	52.3192	0.0002	100.2312
75l1_1	150	Anhedral	cluster zoned				0.0162	0.0315	44.7859	0.0001	0.0332	0.2542	3.4006	52.3341	0.0376	100.8934
75l1_2	150	Anhedral	cluster zoned				0.0001	0.0001	45.5013	0.0001	0.0001	0.0949	1.9693	52.9881	0.0343	100.5883
75l1_3	150	Anhedral	cluster zoned				0.0707	0.0124	44.9963	0.0001	0.0001	0.0765	2.8574	52.5651	0.0498	100.6284
75l1_4	150	Anhedral	cluster zoned				0.0839	0.0496	45.3693	0.0159	0.0001	0.05	1.1698	53.8666	0.0002	100.6054
75l2_3	100	Anhedral	cluster zoned				0.014	0.0565	46.262	0.0001	0.0001	0.0501	0.2666	54.4641	0.0002	101.1137
75l2_4	100	Anhedral	cluster zoned				0.0001	0.0001	45.447	0.0001	0.0193	0.0701	0.735	54.273	0.0002	100.5449
75l3_1	130	subhedral	zoned rings,porous			HVB	0.0001	0.0485	45.975	0.0001	0.0001	0.0849	1.561	53.1322	0.0002	100.8021
75l3_1	130	subhedral	zoned rings,porous			HVB	0.0269	0.0001	45.915	0.0066	0.0001	0.02	0.2192	54.0916	0.0002	100.2797
75l3_2	130	subhedral	zoned rings,porous			HVB	0.0001	0.0001	45.7483	0.0038	0.0407	0.0934	0.2543	53.544	0.0377	99.7224
75l3_3	130	subhedral	zoned rings,porous			HVB	0.0001	0.0001	46.7278	0.0001	0.0001	0.0267	0.0755	54.6469	0.0094	101.4867
75l3_4	130	subhedral	zoned rings,porous			HVB	0.0105	0.0023	46.2605	0.0001	0.0265	0.0267	0.0065	53.7923	0.0121	100.1375
75l4_1	130	subhedral	zoned rings,porous			HVB	0.0001	0.0147	45.9066	0.0001	0.0519	0.0001	0.0493	53.4614	0.0444	99.5286
75l4_2	130	subhedral	zoned rings,porous			HVB	0.0082	0.026	46.2485	0.0208	0.0234	0.0033	0.2542	54.0054	0.0135	100.6033
75l4_3	130	subhedral	zoned rings,porous			HVB	0.0001	0.0001	45.8112	0.0029	0.0628	0.0001	1.7627	53.1039	0.0002	100.744
75l4_4	130	subhedral	zoned rings,porous			HVB	0.0597	0.0001	46.4834	0.0001	0.0001	0.0001	0.1642	52.2696	0.0002	98.9775

Sample/EPMA spot position	Pyrite size (µm)	Morphology	Ore Textures	Quartz Texture	Associated Minerals	Host	Cu	Mn	Fe	Co	Ni	Sb	As	S	Se	Total
75l5_1	40	Anhedral	lamellar,cluster		electrum	Organic replacement	0.0328	0.0215	45.9033	0.0001	0.0305	0.0001	0.0554	52.7486	0.0324	98.8247
75l5_2	40	Anhedral	lamellar,cluster		electrum	Organic replacement	0.0491	0.0079	46.0476	0.0001	0.0001	0.0618	0.4444	53.8555	0.0108	100.4773
75l5_3	40	Anhedral	lamellar,cluster		electrum	Organic replacement	0.0001	0.0361	46.8087	0.0196	0.0193	0.0816	0.3852	53.8348	0.0068	101.1922
75l6_1	60	subhedral	zoned rings,overgrowth		electrum	Organic replacement	0.0058	0.0293	46.5624	0.0001	0.0203	0.03	0.7855	53.9041	0.0122	101.3497
75l6_2	60	subhedral	zoned rings,overgrowth		electrum	Organic replacement	0.0001	0.0124	46.6965	0.0001	0.0001	0.1645	1.4776	53.0369	0.0178	101.406
75l6_3	60	subhedral	zoned rings,overgrowth		electrum	Organic replacement	0.0001	0.0406	46.0168	0.0001	0.0375	0.183	1.4554	53.3913	0.0274	101.1522
75l6_4	60	subhedral	zoned rings,overgrowth		electrum	Organic replacement	0.0001	0.0304	46.5745	0.0001	0.0223	0.0649	0.5103	53.7595	0.0081	100.9702
75l6_5	60	subhedral	zoned rings,overgrowth		electrum	Organic replacement	0.0047	0.0001	46.2129	0.0001	0.0193	0.0783	0.1348	53.0721	0.0002	99.5225
75l7_1	150	Anhedral	overgrowth,porous centre		Arsenopyrite	Stylolite	0.0001	0.0034	46.8828	0.0001	0.0112	0.045	0.3456	54.0097	0.0002	101.2981
75l7_3	150	Anhedral	overgrowth,porous centre		Arsenopyrite	Stylolite	0.0001	0.0158	46.9013	0.0001	0.0001	0.0001	0.3816	54.1412	0.0081	101.4484
75l7_4	150	Anhedral	overgrowth,porous centre		Arsenopyrite	Stylolite	0.0524	0.0001	45.9253	0.0001	0.003	0.0001	1.3874	52.7911	0.0944	100.2539
75pt10	40	Anhedral	overgrowth,porous centre		Arsenopyrite	Stylolite	0.0524	0.0001	45.9253	0.0001	0.003	0.0001	1.3874	52.7911	0.0944	100.2539
75pt11	40	Anhedral	overgrowth,porous centre		Arsenopyrite	Stylolite	0.0058	0.009	45.7992	0.0001	0.0102	0.01	0.5138	53.8595	0.0122	100.2198
75pt2	150	Anhedral	cluster zoned		electrum	HVB	0.0001	0.0271	45.1786	0.0001	0.0061	0.01	0.8645	53.4256	0.0081	99.5202
75pt4	60	Anhedral	zoned rings,overgrowth		electrum	HVB	0.0058	0.0001	46.7383	0.0001	0.0001	0.0001	0.4505	54.0852	0.0135	101.2937
75pt6	10	Anhedral	lamellar,cluster		electrum	Organic replacement	0.0001	0.0001	46.6611	0.0001	0.0001	0.0001	0.3393	54.2108	0.0311	101.2428
75pt8	15	Anhedral	overgrowth		electrum	HVB	0.0187	0.0226	45.0087	0.0001	0.0112	0.055	0.4658	51.785	0.0002	97.3673
75pt9	60	Anhedral	Porous centre				0.0396	0.009	44.9136	0.0001	0.0243	0.0731	1.4125	51.2594	0.0192	97.7508

APPENDIX IV

LA-ICPMS analyis of Pyrite

(full dataset)

APPENDIX IV LA-ICPMS ANALYSIS OF PYRITE (*Total dataset)*

	Ti(ppm)	V(ppm)	Cr(ppm)	Mn(ppm)	Fe(ppm)	Co(ppm)	Ni(ppm)	Cu(ppm)	Zn(ppm)	Ga(ppm)	Ge(ppm)	As(ppm)	Se(ppm)	Nb(ppm)	Mo(ppm)	Ag(ppm)	Cd(ppm)	In(ppm)	Sn(ppm)	Sb(ppm)	Te(ppm)	W(ppm)	Re(ppm)	Au(ppm)	Tl(ppm)	Pb(ppm)	Bi(ppm)	U(ppm)
Sample/spot analysis																												
THRCD 917																												
139.4 mts																												
55aj1	<mdl	<mdl	<mdl	<mdl	465000	16	10	271	<mdl	<mdl	5.9	826	822	<mdl	<mdl	5758	0.35	<mdl	<mdl	0.7	<mdl	<mdl	<mdl	7.1	0.24	6.2	0.30	<mdl
55aj2	1.6	<mdl	<mdl	<mdl	465000	44	72	387	0.76	<mdl	5.8	4835	2539	<mdl	16	16056	<mdl	0.03	0.63	29	1.1	<mdl	<mdl	19	2.1	21	0.48	<mdl
55aj3	<mdl	<mdl	<mdl	<mdl	465000	2.6	0.45	2026	<mdl	<mdl	5.7	28	6176	<mdl	<mdl	49826	<mdl	<mdl	<mdl	0.26	5.9	<mdl	<mdl	198	0.12	4.5	0.45	<mdl
55aj4a	<mdl	<mdl	<mdl	3.2	465000	7.4	26	251	4.5	<mdl	6.3	16974	38	<mdl	6.9	37	<mdl	0.02	<mdl	282	0.52	0.40	0.03	50	68	8.8	0.07	<mdl
55aj4b	<mdl	<mdl	<mdl	<mdl	465000	8.5	47	4.0	<mdl	<mdl	7.4	729	69	<mdl	<mdl	<mdl	<mdl	<mdl	<mdl	<mdl	<mdl	<mdl	<mdl	<mdl	<mdl	0.17	<mdl	<mdl
55aj5	<mdl	<mdl	<mdl	<mdl	465000	16	37	36	<mdl	<mdl	6.5	142	299	<mdl	<mdl	2423	<mdl	<mdl	<mdl	5.0	<mdl	<mdl	<mdl	5.7	0.10	4.9	0.13	<mdl
55aj7	42	1.8	3.6	6.8	465000	74	171	190	1.2	0.38	5.4	1715	197	0.17	70	1111	<mdl	<mdl	<mdl	83	<mdl	0.12	<mdl	32	2.7	106	3.1	0.11
55aj8	38	0.40	<mdl	2.4	465000	48	87	232	2.8	0.36	6.9	1888	287	0.39	37	2386	<mdl	0.03	<mdl	68	0.70	<mdl	0.03	8.0	2.9	137	2.3	0.34
55aj9	4.0	0.68	<mdl	13	465000	27	21	51	4.6	0.47	7.0	4565	51	<mdl	25	20	<mdl	<mdl	0.78	129	0.74	<mdl	<mdl	2.6	6.4	21	0.78	<mdl
55aj10	2112	3.6	22	504	465000	47	43	112	511	0.91	6.8	5817	13	8.0	17	78	<mdl	0.19	2.6	115	<mdl	60	<mdl	3.0	7.0	126	3.6	8.0
55aj11	<mdl	<mdl	<mdl	<mdl	465000	8.7	6.5	31	<mdl	<mdl	5.9	307	349	<mdl	86	1967	<mdl	<mdl	<mdl	3.2	<mdl	<mdl	0.03	2.1	0.80	4.4	0.06	<mdl
55aj12	<mdl	<mdl	<mdl	<mdl	465000	39	121	1377	614	<mdl	6.3	2655	4828	<mdl	1.4	57888	0.59	0.39	<mdl	1.3	1.9	0.08	<mdl	26	0.09	3.0	0.23	<mdl
55aj13	<mdl	0.26	<mdl	1.6	465000	22	44	728	<mdl	<mdl	5.9	7209	1820	<mdl	4.2	12123	<mdl	<mdl	<mdl	14	0.87	<mdl	<mdl	38	0.61	8.3	0.20	<mdl
55aj14	<mdl	<mdl	<mdl	<mdl	465000	11	13	1319	0.76	<mdl	7.1	60	19398	<mdl	<mdl	226575	<mdl	<mdl	<mdl	2.9	7.0	<mdl	<mdl	107	0.16	20	0.85	<mdl
55aj15	132	0.77	<mdl	24	465000	30	31	95	4.9	0.40	6.4	3449	<mdl	1.1	10	30	<mdl	0.04	0.46	154	<mdl	1.6	<mdl	0.33	29	96	0.8	0.29
55aj16	22	1.4	<mdl	3.6	465000	17	24	64	<mdl	<mdl	6.4	1876	94	0.11	2.9	1378	<mdl	<mdl	0.25	11	<mdl	0.21	<mdl	7.8	1.1	42	0.53	0.05
55aj17	20	3.4	5.2	18	465000	91	120	229	8.9	0.56	6.0	3736	91	0.10	1598	289	<mdl	0.08	1.2	133	0.74	1.2	0.04	4.3	17	165	3.8	0.10
55aj18	4.6	<mdl	<mdl	4.9	465000	8.9	47	63	<mdl	<mdl	5.5	116	275	<mdl	<mdl	951	<mdl	<mdl	<mdl	<mdl	<mdl	<mdl	<mdl	2.0	0.06	1.5	<mdl	<mdl
55aj19	2.8	0.71	3.4	2.3	465000	16	48	162	1.5	<mdl	7.0	9222	79	<mdl	2194	187	<mdl	<mdl	<mdl	39	<mdl	0.66	<mdl	30	16	49	0.94	0.03
55aj20	1.3	<mdl	<mdl	<mdl	465000	5.1	18	51	<mdl	<mdl	6.2	1258	1742	<mdl	<mdl	18010	<mdl	<mdl	<mdl	0.40	0.62	<mdl	<mdl	7.8	0.04	2.3	0.29	<mdl
55aj21	499	14	<mdl	14	465000	17	24	136	<mdl	<mdl	<mdl	2593	294	2.5	74	3696	<mdl	<mdl	7.1	25	<mdl	10	<mdl	55	2.0	27	0.47	0.43
55aj22	15	<mdl	<mdl	3.2	465000	42	93	65	<mdl	<mdl	7.8	832	359	<mdl	2.0	1554	<mdl	<mdl	<mdl	39	1.8	<mdl	<mdl	3.2	1.5	55	1.6	<mdl
55aj23	295	0.76	3.8	7.5	465000	62	49	146	3.1	<mdl	6.7	691	1130	1.1	5.4	10426	<mdl	<mdl	<mdl	38	<mdl	2.5	<mdl	39	2.3	64	2.2	0.25
55aj24	7.9	1.8	11	5.3	465000	2.4	14	78	1.4	1.1	6.6	13755	29	<mdl	252	23	<mdl	<mdl	2.1	11	<mdl	0.25	<mdl	39	2.3	11	0.28	0.0
55aj25	17	8.6	12	11	465000	4.4	7.7	29	<mdl	<mdl	7.5	414	324	0.25	<mdl	2388	<mdl	<mdl	1.1	1.6	<mdl	0.37	<mdl	3.0	0.23	18	0.44	0.09
55aj26	<mdl	<mdl	<mdl	7.4	465000	17	89	109	10	<mdl	6.5	5408	1202	<mdl	8.6	8720	<mdl	<mdl	0.26	282	0.45	1.2	<mdl	8.3	116	24	0.23	<mdl
Mean	**201**	**2.9**	**8.7**	**37**	**465000**	**26**	**49**	**317**	**84**	**0.60**	**6.5**	**3504**	**1700**	**1.5**	**245**	**16956**	**0.47**	**0.11**	**1.7**	**61**	**1.9**	**6.0**	**0.03**	**28**	**11**	**39**	**1.0**	**0.88**
S.D	**527**	**4.0**	**6.9**	**120**	**0.00**	**23**	**42**	**499**	**204**	**0.30**	**0.63**	**4273**	**3992**	**2.5**	**612**	**46084**	**0.17**	**0.14**	**2.1**	**83**	**2.2**	**16**	**0.01**	**43**	**26**	**47**	**1.1**	**2.4**
Min	**1.3**	**0.26**	**3.4**	**1.6**	**465000**	**2.4**	**0.45**	**4.0**	**0.76**	**0.36**	**5.4**	**28**	**13**	**0.10**	**1.4**	**20**	**0.35**	**0.02**	**0.25**	**0.26**	**0.45**	**0.08**	**0.03**	**0.33**	**0.04**	**0.17**	**0.06**	**0.02**
Max	**2112**	**14**	**22**	**504**	**465000**	**91**	**171**	**2026**	**614**	**1.1**	**7.8**	**16974**	**19398**	**8.0**	**2194**	**226575**	**0.59**	**0.39**	**7.1**	**282**	**7.0**	**60**	**0.04**	**198**	**116**	**165**	**3.8**	**8.0**

	Ti(ppm)	V(ppm)	Cr(ppm)	Mn(ppm)	Fe(ppm)	Co(ppm)	Ni(ppm)	Cu(ppm)	Zn(ppm)	Ga(ppm)	Ge(ppm)	As(ppm)	Se(ppm)	Nb(ppm)	Mo(ppm)	Ag(ppm)	Cd(ppm)	In(ppm)	Sn(ppm)	Sb(ppm)	Te(ppm)	W(ppm)	Re(ppm)	Au(ppm)	Tl(ppm)	Pb(ppm)	Bi(ppm)	U(ppm)
155.3 mts																												
64aj1	1.1	<mdl	<mdl	7.8	465000	2.2	14	147	3.0	<mdl	6.0	20152	116	<mdl	6.8	568	0.29	0.21	<mdl	996	<mdl	<mdl	0.10	46	99	6.6	<mdl	<mdl
64aj2	0.82	0.03	1.8	11	465000	0.50	3.6	35	4.8	<mdl	6.5	21715	157	<mdl	65	1272	0.58	0.04	4.1	1638	13	<mdl	<mdl	19	192	16	0.09	<mdl
64aj3	<mdl	0.53	<mdl	<mdl	465000	7.7	27	111	3.1	<mdl	7.0	5447	690	<mdl	1370	4108	<mdl	0.02	<mdl	20	0.89	1.1	0.13	18	8.1	27	0.32	<mdl
64aj4	<mdl	0.10	<mdl	<mdl	465000	12	20	135	10	0.17	5.7	2968	564	0.02	19	3256	<mdl	0.21	10	50	3.1	<mdl	<mdl	4.1	1.5	59	0.90	<mdl
64aj5	<mdl	<mdl	<mdl	<mdl	465000	5.9	10	110	1.2	<mdl	5.4	2092	387	<mdl	0.3	5064	<mdl	0.01	<mdl	7.6	1.5	<mdl	<mdl	21	0.56	32	0.19	<mdl
64aj6	<mdl	<mdl	<mdl	0.80	465000	1.7	1.5	80	<mdl	<mdl	5.2	7303	67	<mdl	3.0	272	0.23	<mdl	<mdl	149	<mdl	<mdl	<mdl	22	14	28	0.13	<mdl
64aj7	<mdl	<mdl	<mdl	<mdl	465000	5.7	66	1080	316	1.1	7.3	9473	56	<mdl	6.6	521	0.29	2.7	46	74	1.5	<mdl	0.09	34	3.0	62	0.33	0.01
64aj8	1.9	1.4	<mdl	1.7	465000	26	68	202	21	0.56	7.1	6855	147	<mdl	90	858	<mdl	0.05	0.48	128	0.86	0.35	0.05	27	10	<mdl	<mdl	<mdl
64aj9	<mdl	<mdl	<mdl	<mdl	465000	2.8	11	73	2.1	<mdl	6.3	2653	119	<mdl	1.2	1026	<mdl	<mdl	<mdl	19	1.6	<mdl	<mdl	16	1.9	<mdl	<mdl	<mdl
64aj10	9.4	4.3	<mdl	4.7	465000	9.0	18	251	16	2.2	6.1	17668	39	0.03	173	299	<mdl	0.09	1.2	412	1.0	0.72	0.07	57	44	<mdl	<mdl	<mdl
64aj11	1.7	0.10	<mdl	5.66	465000	16	58	166	4.4	<mdl	5.5	6092	35	<mdl	114	99	<mdl	<mdl	<mdl	46	1.0	0.22	<mdl	37	4.5	<mdl	<mdl	<mdl
64aj12	<mdl	<mdl	<mdl	<mdl	465000	6.5	6.2	98	<mdl	<mdl	7.1	7986	281	<mdl	26	2215	<mdl	<mdl	<mdl	107	<mdl	<mdl	<mdl	15	12	<mdl	<mdl	<mdl
64aj13	1.4	0.27	<mdl	2.2	465000	2.9	4.2	320	11	<mdl	6.9	16420	8187	<mdl	30	49286	3.2	0.03	<mdl	456	4.1	0.34	<mdl	123	42	<mdl	<mdl	<mdl
64aj14	3.4	0.31	<mdl	10	465000	0.29	0.95	40	0.89	<mdl	6.4	3576	45	<mdl	1.5	58	<mdl	<mdl	0.32	12	<mdl	0.12	<mdl	4.7	0.85	<mdl	<mdl	<mdl
64aj15	<mdl	<mdl	<mdl	<mdl	465000	2.3	14	90	<mdl	<mdl	6.6	8049	301	<mdl	2.2	4694	<mdl	<mdl	<mdl	22	3.5	<mdl	<mdl	10	1.4	<mdl	<mdl	<mdl
64aj16	1.4	<mdl	<mdl	<mdl	465000	0.71	1.9	44	<mdl	<mdl	5.0	4499	85	<mdl	0.8	949	<mdl	<mdl	<mdl	8.5	<mdl	<mdl	<mdl	261	0.47	<mdl	<mdl	<mdl
64aj17	1.6	<mdl	<mdl	0.71	465000	0.56	4.5	552	1.6	<mdl	6.3	16173	3598	<mdl	16	27596	<mdl	0.02	0.47	131	7.7	<mdl	<mdl	73	12	<mdl	<mdl	<mdl
64aj18	<mdl	<mdl	<mdl	<mdl	465000	2.7	18	32	0.66	<mdl	6.5	1269	79	<mdl	1.3	887	<mdl	<mdl	<mdl	0.77	4.6	<mdl	<mdl	1.2	0.15	<mdl	<mdl	<mdl
64aj19	<mdl	<mdl	<mdl	7.2	465000	0.31	5.3	85	3.6	<mdl	7.1	24172	566	<mdl	36	2735	0.66	0.04	<mdl	1194	1.3	<mdl	<mdl	24	158	<mdl	<mdl	<mdl
64aj20	<mdl	0.07	<mdl	<mdl	465000	85	46	308	3.8	<mdl	5.2	2423	1652	<mdl	4.2	16468	0.88	0.03	<mdl	41	30	<mdl	<mdl	36	1.7	<mdl	<mdl	<mdl
64aj21	1.5	0.05	<mdl	2.6	465000	15	56	275	5.9	<mdl	6.5	18998	113	<mdl	12	1063	0.38	0.08	1.0	474	1.3	<mdl	<mdl	75	46	<mdl	<mdl	<mdl
Mean	**2.4**	**0.72**	**1.8**	**4.9**	**465000**	**10**	**22**	**202**	**24**	**1.0**	**6.3**	**9809**	**823**	**0.03**	**94**	**5871**	**0.81**	**0.27**	**7.9**	**285**	**4.8**	**0.47**	**0.09**	**44**	**31**	**33**	**0.33**	**0.01**
S.D	**2.5**	**1.3**	**-**	**3.6**	**0.00**	**19**	**23**	**238**	**75**	**0.90**	**0.71**	**7389**	**1871**	**0.00**	**296**	**11901**	**1.0**	**0.73**	**16**	**451**	**7.4**	**0.36**	**0.03**	**58**	**54**	**21**	**0.30**	**-**
Min	**0.82**	**0.03**	**1.8**	**0.71**	**465000**	**0.29**	**0.95**	**32**	**0.66**	**0.17**	**5.0**	**1269**	**35**	**0.02**	**0.29**	**58**	**0.23**	**0.01**	**0.32**	**0.77**	**0.86**	**0.12**	**0.05**	**1.2**	**0.15**	**6.6**	**0.09**	**0.01**
Max	**9.4**	**4.3**	**1.8**	**10.5**	**465000**	**85**	**68**	**1080**	**316**	**2.2**	**7.3**	**24172**	**8187**	**0.03**	**1370**	**49286**	**3.2**	**2.7**	**46**	**1638**	**30**	**1.1**	**0.13**	**261**	**192**	**62**	**0.90**	**0.01**

	Ti(ppm)	V(ppm)	Cr(ppm)	Mn(ppm)	Fe(ppm)	Co(ppm)	Ni(ppm)	Cu(ppm)	Zn(ppm)	Ga(ppm)	Ge(ppm)	As(ppm)	Se(ppm)	Nb(ppm)	Mo(ppm)	Ag(ppm)	Cd(ppm)	In(ppm)	Sn(ppm)	Sb(ppm)	Te(ppm)	W(ppm)	Re(ppm)	Au(ppm)	Tl(ppm)	Pb(ppm)	Bi(ppm)	U(ppm)
THRCD 920																												
144.5 mts																												
72aj1	1.3	0.38	2.8	15	465000	18	40	647	29	0.33	6.2	17241	23	<mdl	185	327	2.1	0.16	1.4	3402	1.6	0.35	0.06	40	710	161	1.1	0.08
72aj2	2.3	0.38	4.4	2.7	465000	55	135	143	8.1	0.61	5.0	3236	35	<mdl	556	45	2.4	0.05	0.24	2574	<mdl	0.15	0.07	11	478	92	0.16	0.02
72aj3	5.0	2.7	<mdl	21	465000	18	42	589	53	1.7	5.4	17621	28	<mdl	159	286	2.2	0.18	1.8	3147	1.4	0.36	0.05	36	696	137	1.3	0.05
72aj4	6.1	3.6	6.5	14	465000	11	31	492	19	2.1	5.9	14383	22	<mdl	374	245	2.2	0.17	0.85	3628	1.3	0.17	<mdl	30	587	124	1.3	0.04
72aj5	2.8	0.63	3.7	2.2	465000	47	144	154	12	0.69	6.4	3400	38	<mdl	584	50	2.7	0.05	0.55	2757	0.75	0.14	0.05	10	447	99	0.24	0.03
72aj6	1095	35	36	48	465000	190	290	633	270	26	6.3	3411	145	5.0	153	109	2.6	0.33	2.8	3081	1.3	61	0.05	18	464	31	1.3	1.6
72aj7	1298	2.5	3.8	46	465000	205	326	633	164	0.95	5.3	5289	368	6.8	137	107	2.6	0.45	0.23	2706	2.3	111	0.03	20	420	40	1.3	1.1
72aj8	155	1.8	15	26	465000	113	171	229	17	1.6	5.8	2781	34	0.82	279	94	1.4	0.05	0.42	4813	1.2	16	0.10	16	511	38	0.40	1.0
72aj9	363	6.5	17	30	465000	10	35	237	15	2.9	6.0	3340	34	1.9	390	107	1.3	0.07	0.60	4199	0.84	19	0.13	16	528	41	0.36	3.5
72aj10	294	1.6	8.8	88	465000	6.5	23	255	14	2.6	6.6	3644	40	1.7	470	113	1.4	0.07	<mdl	3831	1.4	18	0.15	17	589	45	0.26	0.93
72aj11	528	2.7	8.8	42	465000	4.5	10	259	15	2.4	6.6	3729	36	3.5	518	132	1.3	0.08	0.33	3874	1.5	17	0.11	18	543	46	0.27	1.2
72aj12	278	2.4	7.5	23	465000	2.5	4.5	274	16	2.8	6.0	3586	34	2.1	522	133	1.5	0.07	0.44	3779	1.4	15	0.12	18	508	46	0.28	1.7
72aj13	270	2.4	7.0	28	465000	4.4	16	287	15	2.0	7.0	3694	36	1.5	525	126	1.6	0.08	0.48	4057	1.5	15	0.12	17	575	52	0.28	1.4
72aj14	90	1.0	9.1	69	465000	52	61	283	16	1.9	6.5	3579	42	0.49	550	122	1.5	0.11	0.42	4442	1.4	10	0.24	17	616	60	0.69	3.0
72aj15	39	0.60	2.9	27	465000	163	151	1199	41	1.6	6.4	4285	87	0.19	260	124	5.5	0.11	0.40	3310	3.6	4.3	0.05	22	338	186	4.4	0.26
72aj16	269	56	25	136	465000	1121	547	2050	317	57	7.9	23662	172	0.43	291	213	1.5	0.30	7.1	3316	12	5.1	0.44	120	428	180	7.9	21
72aj17	142	34	21	82	465000	96	218	2293	175	29	6.2	19056	119	0.20	1046	253	2.3	0.21	4.4	6565	6.7	3.8	0.16	71	1244	228	8.9	3.1
72aj18	29	0.28	5.4	18	465000	39	179	618	20	1.0	6.7	4701	102	0.11	2864	136	2.5	0.12	0.65	8309	9.3	2.5	0.06	25	808	771	8.8	1.0
72aj19	54	0.59	5.6	61	465000	49	30	542	130	0.40	6.0	4202	71	0.16	747	128	1.7	0.15	0.47	5991	2.1	1.8	<mdl	35	719	146	2.8	0.10
72aj20	125	1.6	<mdl	20	465000	23	43	132	19	1.6	6.9	5348	87	0.75	1440	45	3.2	0.08	0.33	4957	0.65	6.0	<mdl	12	845	189	0.81	0.62
72aj21	<mdl	<mdl	<mdl	47	465000	14	6.1	47	3.3	<mdl	5.6	8979	<mdl	<mdl	17	7.2	<mdl	<mdl	<mdl	691	<mdl	0.83	<mdl	0.9	30	8.5	0.24	<mdl
72aj22	236	1.3	<mdl	35	465000	541	375	804	24	1.3	7.4	4269	77	1.5	794	179	2.7	0.15	0.38	4099	2.8	39	0.13	31	548	236	6.1	1.4
72aj23	43	0.11	<mdl	<mdl	465000	5.5	11	10	1.8	<mdl	5.2	9610	<mdl	0.25	1.3	3.1	0.59	<mdl	1.1	18	<mdl	0.20	<mdl	0.44	22	2.7	<mdl	0.16
72aj24	4.0	0.48	<mdl	7.5	465000	33	158	608	14	0.47	6.3	5394	122	0.02	497	101	3.9	0.12	0.26	7459	4.5	0.16	<mdl	14	651	586	2.6	0.12
72aj25	<mdl	0.39	<mdl	93	465000	11	6.6	25	5.2	0.12	6.9	55820	6.5	0.01	12	7.3	<mdl	0.08	<mdl	1532	0.40	<mdl	0.03	2.1	320	3	0.31	0.01
Mean	**232**	**6.6**	**11**	**41**	**465000**	**113**	**122**	**538**	**57**	**6.2**	**6.3**	**9370**	**76**	**1.4**	**535**	**128**	**2.2**	**0.14**	**1.2**	**3861**	**2.7**	**14**	**0.11**	**25**	**545**	**142**	**2.2**	**1.8**
S.D	**337**	**14**	**8.9**	**33**	**0.00**	**239**	**139**	**567**	**86**	**13**	**0.69**	**11388**	**77**	**1.8**	**587**	**85**	**1.0**	**0.10**	**1.7**	**1867**	**2.9**	**25**	**0.10**	**25**	**244**	**178**	**2.8**	**4.3**
Min	**1.3**	**0.11**	**2.8**	**2.2**	**465000**	**2.5**	**4.5**	**10**	**1.8**	**0.12**	**5.0**	**2781**	**6.5**	**0.01**	**1.3**	**3.1**	**0.59**	**0.05**	**0.23**	**18**	**0.40**	**0.14**	**0.03**	**0.44**	**22**	**3**	**0.16**	**0.01**
Max	**1298**	**56**	**36**	**136**	**465000**	**1121**	**547**	**2293**	**317**	**57**	**7.9**	**55820**	**368**	**6.8**	**2864**	**327**	**5.5**	**0.45**	**7.1**	**8309**	**12**	**111**	**0.44**	**120**	**1244**	**771**	**8.9**	**21**

	Ti(ppm)	V(ppm)	Cr(ppm)	Mn(ppm)	Fe(ppm)	Co(ppm)	Ni(ppm)	Cu(ppm)	Zn(ppm)	Ga(ppm)	Ge(ppm)	As(ppm)	Se(ppm)	Nb(ppm)	Mo(ppm)	Ag(ppm)	Cd(ppm)	In(ppm)	Sn(ppm)	Sb(ppm)	Te(ppm)	W(ppm)	Re(ppm)	Au(ppm)	Tl(ppm)	Pb(ppm)	Bi(ppm)	U(ppm)
163.3 mts																											
76aj1	22	6.5	13	115	465000	42	56	108	75	2.5	9.3	13486	<mdl	0.09	1011	32	<mdl	0.12	1.3	82	<mdl	2.6	<mdl	11	8.7	125	3.0	2.4
76aj2	105	11	12	24	465000	14	17	72	18	3.0	6.4	1879	7.6	0.64	1594	29	<mdl	0.13	9.1	83	0.43	4.5	0.11	0.58	26	156	1.2	13
76aj3	7.9	0.08	<mdl	46	465000	54	70	118	6.0	0.18	6.3	3391	3.6	0.02	5.2	1.9	<mdl	0.03	0.22	249	0.91	<mdl	<mdl	0.35	45	229	3.1	<mdl
76aj4	25	0.58	5.9	120	465000	10	16	238	62	0.13	10	5588	<mdl	0.12	135	53	<mdl	<mdl	0.42	112	0.54	12	<mdl	4.8	13	83	1.6	0.02
76aj5	<mdl	<mdl	<mdl	96	465000	1.7	2.4	22	7.5	<mdl	4.5	520	<mdl	0.06	70	1.1	<mdl	<mdl	<mdl	40	0.85	1.0	<mdl	0.60	93	54	0.31	0.07
76aj6	170	6.1	<mdl	328	465000	50	87	154	9.2	0.93	7.1	6645	36	0.28	5312	79	0.32	<mdl	0.53	287	0.41	6.5	0.19	2.9	60	87	1.0	0.5
76aj7	3.5	0.13	<mdl	135	465000	0.63	11	45	14	0.18	6.9	5487	16	<mdl	107	8.5	0.21	<mdl	0.29	617	<mdl	0.77	<mdl	1.0	94	10	0.05	<mdl
76aj8	577	0.09	<mdl	6.7	465000	129	5.8	17	2.6	0.12	6.5	366	<mdl	2.2	6.4	4.2	<mdl	<mdl	0.27	68	0.75	0.34	<mdl	<mdl	0.87	350	2.8	0.30
76aj9	18	3.9	12	220	465000	57	63	158	25	1.2	5.3	1375	59	0.06	153	59	0.24	0.03	1.5	117	0.48	1.3	<mdl	3.4	5.6	71	1.5	<mdl
76aj10	29	3.3	<mdl	36	465000	25	45	190	33	0.93	6.9	1986	8.8	0.38	453	71	0.65	0.04	1.7	251	0.63	1.2	<mdl	2.5	29	176	1.2	0.12
76aj11	65	0.39	3.8	511	465000	38	24	274	14	0.34	6.8	387	<mdl	0.20	14	14	<mdl	<mdl	<mdl	14	<mdl	0.07	<mdl	0.05	2.1	8.3	0.11	<mdl
Mean	**102**	**3.2**	**9.4**	**149**	**465000**	**38**	**36**	**127**	**24**	**1.0**	**6.9**	**3737**	**22**	**0.40**	**805**	**32**	**0.36**	**0.07**	**1.7**	**175**	**0.63**	**3.0**	**0.15**	**2.7**	**34**	**123**	**1.4**	**2.4**
S.D	**175**	**3.7**	**4.3**	**153**	**0.00**	**37**	**29**	**85**	**24**	**1.0**	**1.5**	**3939**	**22**	**0.66**	**1578**	**29**	**0.20**	**0.05**	**2.8**	**173**	**0.19**	**3.8**	**0.06**	**3.2**	**35**	**101**	**1.1**	**4.8**
Min	**3.5**	**0.08**	**3.8**	**6.7**	**465000**	**0.63**	**2.4**	**17**	**2.6**	**0.12**	**4.5**	**366**	**3.6**	**0.02**	**5.2**	**1.1**	**0.21**	**0.03**	**0.22**	**14**	**0.41**	**0.07**	**0.11**	**0.05**	**0.87**	**8.3**	**0.05**	**0.02**
Max	**577**	**11**	**13**	**511**	**465000**	**129**	**87**	**274**	**75**	**3.0**	**10**	**13486**	**59**	**2.2**	**5312**	**79**	**0.65**	**0.13**	**9.1**	**617**	**0.91**	**12**	**0.19**	**11**	**94**	**350**	**3.1**	**13**
THRCD 921																												
191.3 mts																												
19aj1	<mdl	0.07	<mdl	12	465000	1.4	2.6	4.9	13	0.05	5.9	160	4.9	0.01	0.30	0.75	<mdl	<mdl	<mdl	0.36	<mdl	0.27	<mdl	<mdl	17	5.6	0.05	<mdl
19aj2	1.8	0.10	<mdl	11	465000	2.4	5.8	60	4.9	<mdl	5.9	270	2.3	<mdl	14	5.4	<mdl	<mdl	0.57	27	<mdl	<mdl	<mdl	0.27	38	71	0.37	<mdl
19aj3	11	2.1	<mdl	25	465000	11	14	54	9.3	1.0	7.5	548	<mdl	0.07	241	14	<mdl	<mdl	<mdl	20	<mdl	0.31	<mdl	1.5	7.3	42	0.71	0.12
19aj4	<mdl	0.34	6.6	6.2	465000	8.4	14	63	3.9	0.29	8.1	3215	19	<mdl	34	10	<mdl	<mdl	<mdl	11	<mdl	0.19	<mdl	7.2	4.2	42	0.51	<mdl
19aj5	5.2	3.0	<mdl	47	465000	18	16	30	1501	0.94	8.4	609	<mdl	<mdl	1.6	6.8	1.3	2.5	3.6	14	<mdl	<mdl	<mdl	0.40	6.7	29	0.42	<mdl
19aj6	2.9	0.46	2.6	25	465000	10	15	53	25	0.19	6.6	2876	11	<mdl	90	11	<mdl	0.03	0.90	13	<mdl	0.41	<mdl	5.0	5.6	29	0.25	0.04
19aj7	<mdl	0.16	<mdl	2.8	465000	7.1	10	66	4.6	0.07	5.2	2423	16	<mdl	81	8.9	<mdl	<mdl	2.3	31	<mdl	0.27	<mdl	10	3.6	40	0.41	<mdl
19aj8	2.4	0.22	<mdl	14	465000	11	10	30	13	<mdl	6.3	143	5.2	<mdl	2.4	3.2	<mdl	0.06	7.4	5.4	<mdl	<mdl	<mdl	0.17	12	56	0.58	<mdl
19aj9	<mdl	0.26	<mdl	12	465000	10	10	27	14	0.06	6.2	377	6.1	<mdl	18	4.8	<mdl	<mdl	4.2	7.0	<mdl	<mdl	<mdl	1.1	8.8	42	0.65	<mdl
19aj10	3.3	0.68	2.9	34	465000	20	22	41	6.6	0.18	5.8	1414	13	<mdl	81	7.8	<mdl	<mdl	0.40	16	<mdl	0.10	<mdl	3.4	4.0	29	0.41	0.01
19aj11	2.7	0.79	<mdl	119	465000	11	11	50	46	0.24	6.5	120	4.7	<mdl	1.1	7.3	<mdl	0.03	3.4	4.0	<mdl	0.08	<mdl	0.23	18	36	0.28	<mdl
19aj12	2.3	0.56	<mdl	48	465000	22	26	33	17	0.10	6.0	591	16	<mdl	10	7.3	<mdl	<mdl	0.65	7.7	<mdl	0.14	<mdl	1.0	2.3	41	0.63	<mdl
Mean	**4.0**	**0.73**	**4.0**	**30**	**465000**	**11**	**13**	**43**	**138**	**0.31**	**6.5**	**1062**	**10**	**0.04**	**48**	**7.2**	**1.3**	**0.67**	**2.6**	**13**	**-**	**0.22**	**-**	**2.8**	**11**	**39**	**0.44**	**0.06**
S.D	**3.1**	**0.91**	**2.2**	**32**	**0.00**	**6.4**	**6.4**	**18**	**429**	**0.36**	**1.0**	**1138**	**5.9**	**0.04**	**70**	**3.5**	**-**	**1.3**	**2.3**	**9.2**	**-**	**0.11**	**-**	**3.3**	**10**	**16**	**0.19**	**0.06**
Min	**1.8**	**0.07**	**2.6**	**2.8**	**465000**	**1.4**	**2.6**	**4.9**	**3.9**	**0.05**	**5.2**	**120**	**2.3**	**0.01**	**0.30**	**0.75**	**1.3**	**0.03**	**0.40**	**0.36**	**0.00**	**0.08**	**0.00**	**0.17**	**2.3**	**5.6**	**0.05**	**0.01**
Max	**11**	**3.0**	**6.6**	**119**	**465000**	**22**	**26**	**66**	**1501**	**1.0**	**8.4**	**3215**	**19**	**0.07**	**241**	**14**	**1.3**	**2.5**	**7.4**	**31**	**0.00**	**0.41**	**0.00**	**10**	**38**	**71**	**0.71**	**0.12**

	Ti(ppm)	V(ppm)	Cr(ppm)	Mn(ppm)	Fe(ppm)	Co(ppm)	Ni(ppm)	Cu(ppm)	Zn(ppm)	Ga(ppm)	Ge(ppm)	As(ppm)	Se(ppm)	Nb(ppm)	Mo(ppm)	Ag(ppm)	Cd(ppm)	In(ppm)	Sn(ppm)	Sb(ppm)	Te(ppm)	W(ppm)	Re(ppm)	Au(ppm)	Tl(ppm)	Pb(ppm)	Bi(ppm)	U(ppm)
THRCD 925																											
143.5 mts																											
6aj1	11	1.2	<mdl	<mdl	465000	33	72	36	2.1	0.82	<mdl	7488	8.4	0.08	2.3	27	<mdl	<mdl	0.79	65	<mdl	0.51	<mdl	2.2	1.3	82	1.4	<mdl
6aj2	28	16	26	662	465000	122	103	152	17	1.4	6.1	4037	24	0.16	1570	38	<mdl	0.06	0.69	111	1.4	8.6	<mdl	10	11	225	3.9	3.2
6aj3	54	11	8.2	21	465000	7.3	11	130	3.2	6.5	6.8	5868	6.3	0.23	9.1	22	<mdl	<mdl	0.76	75	<mdl	8.5	<mdl	1.0	4.4	85	3.0	0.08
6aj4	39	0.83	<mdl	17	465000	12	30	227	10	1.3	8.3	11309	17	0.33	97	42	<mdl	<mdl	<mdl	251	<mdl	1.1	<mdl	3.2	28	135	1.7	0.16
6aj5	111	2.5	8.2	899	465000	3.4	4.1	131	12	1.7	6.0	3910	22	0.71	166	70	<mdl	0.07	2.6	108	<mdl	0.80	<mdl	5.5	13	102	1.6	0.55
6aj6	51	1.4	5.2	336	465000	1.4	1.8	73	4.9	0.90	6.3	6056	54	0.47	172	18	<mdl	0.04	2.0	77	<mdl	0.38	<mdl	7.6	8.1	53	0.84	0.92
6aj7	118	2.4	7.4	423	465000	4.2	4.5	121	8.6	1.1	5.9	7865	35	0.8	171	46	0.39	0.07	4.7	120	<mdl	1.0	0.05	6.3	10	85	1.6	2.0
6aj8	401	15	6.2	35	465000	47	138	97	4.1	0.20	5.9	3414	148	3.9	5.6	29	0.36	0.07	2.4	24	<mdl	21	<mdl	5.1	1.0	77	0.79	10
6aj9	73	0.63	<mdl	350	465000	57	59	203	15	0.28	8.8	3063	<mdl	0.41	36	11	<mdl	<mdl	2.9	118	<mdl	1.1	<mdl	0.59	7.6	129	2.6	0.13
6aj10	<mdl	<mdl	<mdl	0.68	465000	4.3	8.8	23	0.64	<mdl	6.3	1533	12	<mdl	34	15	<mdl	<mdl	<mdl	29	<mdl	<mdl	<mdl	1.2	1.9	26	0.60	<mdl
6aj11	457	1.0	<mdl	1245	465000	182	311	139	121	0.28	6.2	7933	8.5	1.6	32	7.0	<mdl	<mdl	<mdl	18	<mdl	1.3	<mdl	1.4	3.0	42	0.38	1.7
6aj12	3.1	0.11	6.5	63	465000	24	56	80	6.5	0.24	6.3	337	<mdl	<mdl	10	21	<mdl	<mdl	<mdl	8.0	<mdl	0.32	<mdl	0.84	3.6	67	0.17	<mdl
6aj13	134	3.4	6.9	97	465000	34	49	203	11	0.44	6.1	1266	3.8	0.69	13	19	<mdl	0.05	0.79	64	<mdl	2.8	<mdl	0.49	20	126	0.89	0.23
6aj14	1.9	0.15	<mdl	215	465000	13	55	170	19	<mdl	6.4	1628	23	<mdl	35	13	<mdl	0.05	1.3	12	<mdl	1.0	<mdl	3.7	5.8	21	0.92	<mdl
Mean	**114**	**4.2**	**9.3**	**336**	**465000**	**39**	**65**	**128**	**17**	**1.3**	**6.6**	**4693**	**30**	**0.85**	**168**	**27**	**0.38**	**0.06**	**1.9**	**77**	**1.4**	**3.7**	**0.05**	**3.5**	**8.5**	**90**	**1.5**	**1.9**
S.D	**147**	**5.7**	**6.7**	**388**	**0.00**	**52**	**82**	**62**	**31**	**1.7**	**0.93**	**3172**	**40**	**1.1**	**409**	**17**	**0.02**	**0.01**	**1.3**	**64**	**-**	**5.9**	**-**	**3.0**	**7.7**	**53**	**1.1**	**3.0**
Min	**1.9**	**0.11**	**5.2**	**0.68**	**465000**	**1.4**	**1.8**	**23**	**0.64**	**0.20**	**5.9**	**337**	**3.8**	**0.08**	**2.3**	**7.0**	**0.36**	**0.04**	**0.69**	**8.0**	**1.4**	**0.32**	**0.05**	**0.49**	**1.0**	**21**	**0.17**	**0.08**
Max	**457**	**16**	**26**	**1245**	**465000**	**182**	**311**	**227**	**121**	**6.5**	**8.8**	**11309**	**148**	**3.9**	**1570**	**70**	**0.39**	**0.07**	**4.7**	**251**	**1.4**	**21**	**0.05**	**10**	**28**	**225**	**3.9**	**10**
THRCD 926																											
140.6 mts																											
36baj1	<mdl	0.14	<mdl	11	465000	<mdl	<mdl	4.1	1.3	0.24	7.3	27027	<mdl	<mdl	15	5.3	<mdl	0.04	<mdl	113	<mdl	<mdl	<mdl	17	6.8	2.8	<mdl	<mdl
36baj2	<mdl	3.4	<mdl	282	465000	0.94	10	15	4.8	0.29	6.5	24411	<mdl	<mdl	2.3	6.0	<mdl	0.06	<mdl	63	<mdl	<mdl	<mdl	32	4.7	10	<mdl	<mdl
36baj3	<mdl	0.17	<mdl	31	465000	3.0	22	19	<mdl	<mdl	7.6	30456	19	<mdl	15	15	<mdl	<mdl	<mdl	64	<mdl	<mdl	<mdl	41	14	15	<mdl	<mdl
36baj4	<mdl	<mdl	<mdl	<mdl	465000	2.9	11	43	<mdl	<mdl	<mdl	18500	<mdl	<mdl	343	26	<mdl	<mdl	<mdl	77	<mdl	2.0	<mdl	46	5.0	32	<mdl	0.47
36baj5	8.1	5.5	<mdl	<mdl	465000	0.32	3.1	22	4.5	1.8	5.7	25517	<mdl	<mdl	38	9.3	<mdl	<mdl	<mdl	60	<mdl	<mdl	<mdl	85	2.9	6.9	0.12	0.08
Mean	**8.1**	**2.3**	**-**	**108**	**465000**	**1.8**	**11**	**21**	**3.5**	**0.79**	**6.8**	**25182**	**19**	**-**	**83**	**12**	**-**	**0.05**	**-**	**75**	**-**	**2.0**	**-**	**44**	**6.7**	**13**	**0.12**	**0.27**
S.D	**-**	**2.6**	**-**	**151**	**0.00**	**1.4**	**7.6**	**14**	**2.0**	**0.91**	**0.85**	**4375**	**-**	**-**	**146**	**8.7**	**-**	**0.02**	**-**	**22**	**-**	**#DIV/0!**	**-**	**25**	**4.4**	**11**	**-**	**0.28**
Min	**8.1**	**0.14**	**0.00**	**11**	**465000**	**0.32**	**3.1**	**4.1**	**1.3**	**0.24**	**5.7**	**18500**	**19**	**0.00**	**2.3**	**5.3**	**0.00**	**0.04**	**0.00**	**60**	**0.00**	**2.0**	**0.00**	**17**	**2.9**	**2.8**	**0.12**	**0.08**
Max	**8.1**	**5.5**	**0.00**	**282**	**465000**	**3.0**	**22**	**43**	**4.8**	**1.8**	**7.6**	**30456**	**19**	**0.00**	**343**	**26**	**0.00**	**0.06**	**0.00**	**113**	**0.00**	**2.0**	**0.00**	**85**	**14**	**32**	**0.12**	**0.47**

	Ti(ppm)	V(ppm)	Cr(ppm)	Mn(ppm)	Fe(ppm)	Co(ppm)	Ni(ppm)	Cu(ppm)	Zn(ppm)	Ga(ppm)	Ge(ppm)	As(ppm)	Se(ppm)	Nb(ppm)	Mo(ppm)	Ag(ppm)	Cd(ppm)	In(ppm)	Sn(ppm)	Sb(ppm)	Te(ppm)	W(ppm)	Re(ppm)	Au(ppm)	Tl(ppm)	Pb(ppm)	Bi(ppm)	U(ppm)
141.2 mts																												
38aj1	1.5	2.3	3.0	351	465000	0.09	0.57	4.1	2.2	0.29	5.9	16765	<mdl	<mdl	2.4	3.5	<mdl	0.03	<mdl	127	<mdl	0.33	<mdl	0.14	12	1.5	<mdl	0.03
38aj2	1.4	0.10	<mdl	6.0	465000	0.61	4.1	10	2.0	<mdl	5.7	14169	<mdl	<mdl	64	8.5	<mdl	0.03	<mdl	100	<mdl	<mdl	<mdl	1.9	10	8.6	0.23	0.03
38aj3	<mdl	0.35	<mdl	49	465000	0.25	<mdl	3.2	0.79	<mdl	5.7	20061	<mdl	<mdl	2.8	5.4	<mdl	0.03	<mdl	121	<mdl	0.12	<mdl	0.08	7.7	2.8	0.05	<mdl
38aj3b	1.7	0.21	<mdl	13	465000	<mdl	1.9	5.8	0.82	<mdl	6.2	16673	<mdl	<mdl	2.0	6.1	<mdl	0.03	<mdl	108	<mdl	<mdl	<mdl	0.32	8.0	6.2	0.17	<mdl
38aj4	1.5	0.43	2.8	34	465000	0.54	8.3	14	1.3	<mdl	5.9	24386	2.8	<mdl	3.1	17	<mdl	0.04	<mdl	161	<mdl	0.08	<mdl	2.5	10	11	0.26	0.04
38aj4b	2.6	0.43	<mdl	1.8	465000	0.52	0.82	7.4	0.92	0.10	5.5	15544	<mdl	<mdl	2.4	6.3	<mdl	<mdl	0.24	91	<mdl	<mdl	<mdl	3.0	7.3	3.8	0.08	<mdl
38aj5	2.3	0.10	<mdl	14	465000	0.36	0.75	16	0.93	<mdl	5.3	6464	<mdl	<mdl	2.0	14	<mdl	<mdl	<mdl	96	<mdl	0.12	<mdl	0.55	17	17	0.42	<mdl
38aj6	13	1.0	<mdl	67	465000	0.36	10	13	1.3	<mdl	5.9	27954	<mdl	0.03	5.1	12	<mdl	0.03	<mdl	231	<mdl	0.17	<mdl	1.1	14	7.2	0.11	0.03
38aj7	5.2	0.19	<mdl	10	465000	0.79	14	23	3.0	<mdl	5.8	33596	3.5	0.02	12	22	<mdl	0.03	<mdl	317	<mdl	0.14	<mdl	1.3	15	14	0.32	0.12
38aj8	111	0.68	<mdl	1.8	465000	6.0	13	17	<mdl	0.21	7.4	22610	15	1.8	4.7	15	<mdl	<mdl	<mdl	96	<mdl	1.2	<mdl	2.9	10	12	<mdl	0.30
38aj9	<mdl	9.4	15	286	465000	0.57	14	38	6.2	<mdl	<mdl	30558	<mdl	<mdl	22	21	<mdl	<mdl	<mdl	208	<mdl	0.66	<mdl	5.5	12	19	0.34	0.71
38aj10	29	0.11	2.8	4.9	465000	0.19	4.5	18	0.86	0.06	6.6	13332	<mdl	2.2	4.3	16	<mdl	0.03	<mdl	99	<mdl	0.21	<mdl	0.77	12	18	0.35	<mdl
38aj11	9.3	4.0	10	51	465000	0.66	8.5	38	6.2	3.1	6.6	16454	6.0	0.02	5.6	24	<mdl	0.04	1.0	90	<mdl	0.12	<mdl	3.0	7.1	25	0.47	<mdl
Mean	**16**	**1.5**	**6.6**	**68**	**465000**	**0.91**	**6.7**	**16**	**2.2**	**0.75**	**6.0**	**19890**	**6.9**	**0.81**	**10**	**13**	**-**	**0.03**	**0.62**	**142**	**-**	**0.31**	**-**	**1.8**	**11**	**11**	**0.25**	**0.18**
S.D	**32**	**2.6**	**5.4**	**114**	**-**	**1.6**	**5.3**	**11**	**2.0**	**1.3**	**0.57**	**7644**	**5.9**	**1.1**	**17**	**6.9**	**-**	**0.00**	**0.54**	**70**	**-**	**0.36**	**-**	**1.6**	**3.1**	**7.1**	**0.14**	**0.25**
Min	**1.4**	**0.10**	**2.8**	**1.8**	**465000**	**0.09**	**0.57**	**3.2**	**0.79**	**0.06**	**5.3**	**6464**	**2.8**	**0.02**	**2.0**	**3.5**	**0.00**	**0.03**	**0.24**	**90**	**0.00**	**0.08**	**0.00**	**0.08**	**7.1**	**1.5**	**0.05**	**0.03**
Max	**111**	**9.4**	**15**	**351**	**465000**	**6.0**	**14**	**38**	**6.2**	**3.1**	**7.4**	**33596**	**15**	**2.2**	**64**	**24**	**0.00**	**0.04**	**1.0**	**317**	**0.00**	**1.2**	**0.00**	**5.5**	**17**	**25**	**0.47**	**0.71**

APPENDIX V

Electrum analysis

(full dataset)

APPENDIX V ELECTRUM ANALYSIS (EPMA) *Total Dataset*

Sample/EPMA point		Au	Ag	Cu	Hg	Bi	Te	Total	Au/(Ag+Au)2 a.p.f.u	Host of Electrum	Size (µm)
64aj3		58.17	44.01	0.00	0.30	0.30	0.03	**102.8**	0.42		50
64aj4		58.03	43.12	0.00	0.59	0.17	0.07	**102.0**	0.42	Stylolites, Weak ginguro mineralisation	60
64aj5	TH 917: 155.3	57.54	43.83	0.03	0.17	0.36	0.03	**102.0**	0.42		60
64aj6		58.10	43.93	0.00	0.33	0.19	0.10	**102.6**	0.42		25
64aj11		58.25	43.51	0.12	0.62	0.00	0.04	**102.5**	0.42		25
Mean		***58.02***	***43.68***	***0.03***	***0.40***	***0.20***	***0.05***	***102.39***	0.42		
66aj2		61.26	40.56	0.00	0.00	0.22	0.08	**102.1**	0.45	Chalcedonic silica, carbonate blade replacement	
66aj3	TH 917: 163.5	58.67	42.73	0.00	0.21	0.21	0.03	**101.8**	0.43		
66aj4		59.52	41.66	0.00	0.61	0.11	0.04	**101.9**	0.44		
Mean		***59.82***	***41.648***	***0.00143***	***0.2707***	***0.1803***	***0.05123***	***101.969***	0.44		
75aj14		68.51	30.75	0.02	0.47	0.28	0.02	**100.0**	0.55		25
75aj15		70.71	31.66	0.00	0.00	0.00	0.00	**102.4**	0.55	With Pyrite, in quartz infill,secondary breccia	25
75aj16	TH 920: 182.3	69.28	31.87	0.00	0.23	0.25	0.10	**101.7**	0.54		25
75aj17		73.97	27.41	0.04	0.32	0.15	0.05	**101.9**	0.60		25
75aj19		69.44	31.24	0.00	0.28	0.07	0.00	**101.0**	0.55		25
75aj20		70.33	31.45	0.03	0.39	0.28	0.11	**102.6**	0.55		25
Mean		***70.37***	***30.73***	***0.02***	***0.28***	***0.17***	***0.05***	***101.62***	0.56		
6aj1	TH 925: 143.5	66.16	34.24	0.00	0.00	0.14	0.09	**100.6**	0.51	In silica, fluorite rich hydrothermal crackle breccia	30
6aj2		66.35	35.32	0.02	0.24	0.15	0.04	**102.1**	0.51		30
Mean		***66.25***	***34.78***	***0.01***	***0.12***	***0.14***	***0.06***	***101.36***	0.51		
62aj(5)*		65.51	34.49					100.00		Silica band, calcite blade replacement	10
64aj(20)*		63.95	36.05					100.00			30
64aj(50)*		62.01	37.99					100.00		Stylolites, Weak ginguro mineralisation	25
64aj(54)*		59.28	38.31			1.6		100.00			5
64aj(58)*		61.90	36.50			1.61		100.00			15
64aj(62)*		60.35	32.82			5.53		100.00			20
66aj(2)*		64.99	35.01					100.00		Chalcedonic silica, calcite blade replacement	50
74aj(13)*		62.3	29.13					100.00		Stylolite, hydrothermal crackle breccia	15
75aj(13)*		75.25	24.75					100.00		With Pyrite, in quartz infill,secondary breccia	20
75aj(15)*		77.13	22.87					100.00			10
75aj(17)*		76.24	23.76					100.00			6

* denotes electrum analysis by SEM with EDAX. Phillips XL30-counts @ 55 Lsecs.

APPENDIX VI

LA-ICPMS analysis of Molybdenite

(full dataset)

APPENDIX VI LAICPMS MOLYBDENUM *total dataset*

Molybdenum

AJ 16

THRCD 925

179.9 mts

Analysis Spot	Ti (ppm)	V (ppm)	Cr (ppm)	Mn (ppm)	Fe (ppm)	Co (ppm)	Ni (ppm)	Cu (ppm)	Zn (ppm)	Ga (ppm)	Ge (ppm)	As (ppm)	Se (ppm)	Nb (ppm)	Mo (ppm)	Ag (ppm)	Cd (ppm)	In (ppm)	Sn (ppm)	Sb (ppm)	Te (ppm)	W (ppm)	Re (ppm)	Au (ppm)	Tl (ppm)	Pb (ppm)	Bi (ppm)	U (ppm)
16aj1	472	444	69	81	128122	19	30	188	52	40	18	6890	295	0.52	599400	9552	<mdl	0.33	15	5101	10	688	18	1.4	5163	2134	8.2	13
16aj2	527	470	140	29	83494	9.1	20	145	50	47	<mdl	5134	253	0.79	599400	7878	<mdl	0.38	16	5002	7.8	605	17	0.49	4792	2070	6.9	7.1
16aj3	11838	466	136	37	86289	10	21	156	50	51	<mdl	5121	265	51	599400	7875	<mdl	0.62	26	4984	6.3	629	17	<mdl	4691	1946	6.9	10
16aj4	112	384	31	20	71862	7.6	16	128	31	9.5	6.1	4934	254	0.23	599400	7888	3.4	0.13	4.4	4445	6.6	967	14	0.45	5385	2086	7.8	7.0
16aj5	2314	437	51	32	82255	13	17	158	56	20	4.9	5019	238	11	599400	8378	2.4	0.25	13	4470	8.2	937	15	0.43	5427	1953	7.5	8.1
16aj6	2206	591	151	56	87421	12	19	156	73	84	<mdl	5117	225	7.0	599400	7724	3.6	0.66	25	5173	7.1	506	15	<mdl	4793	2187	6.4	5.2
16aj7	2119	793	252	48	99084	12	<mdl	161	88	149	<mdl	4974	226	1.8	599400	8331	<mdl	<mdl	29	5683	<mdl	479	23	<mdl	4540	1663	6.9	12
16aj8	387	379	23	20	67161	13	17	178	63	8.1	6.4	5590	236	0.56	599400	8374	1.9	0.15	3.7	4631	8.8	746	7.2	0.29	5349	2772	8.7	3.3
16aj9	112	386	15	15	66567	12	17	159	64	5.9	5.0	5359	225	0.26	599400	8120	3.1	0.10	3.3	4362	9.2	782	6.6	0.34	5260	2648	8.2	2.8
16aj10	203	448	44	31	70018	12	17	155	62	18	4.9	5344	216	0.31	599400	7769	3.6	0.20	6.8	4518	8.3	618	8.1	0.35	4969	2487	7.8	2.7
16aj11	105	339	15	14	61446	11	15	149	43	9.2	4.3	4969	218	0.23	599400	7439	2.6	0.12	3.3	4116	7.9	934	10	0.34	5330	2460	7.7	2.6
16aj12	1124	381	50	25	73969	29	30	258	159	8.3	5.6	5643	198	4.3	599400	5985	3.6	0.13	4.7	4550	11	643	23	0.41	3632	2013	10	5.5
16aj13	5504	382	203	246	144974	33	55	175	53	47	10	5099	186	22	599400	6895	1.6	0.35	12	4929	8.1	1037	17	0.68	5676	2046	8.9	13
16aj14	81	303	24	13	61935	15	15	185	66	5.1	5.0	5009	213	0.16	599400	7433	2.3	0.07	3.1	4132	8.0	964	15	0.42	5499	2151	7.7	2.0
16aj15	150	388	37	24	63388	11	17	146	54	12	4.3	5167	191	0.24	599400	10175	4.2	0.21	4.5	4195	7.7	852	12	0.43	5152	2530	7.9	4.0
Mean	**1817**	**439**	**83**	**46**	**83199**	**15**	**22**	**166**	**64**	**34**	**6.7**	**5291**	**229**	**6.8**	**599400**	**7988**	**2.9**	**0.26**	**11**	**4686**	**8.2**	**759**	**15**	**0.50**	**5044**	**2210**	**7.8**	**6.6**
S.D	**3135.72**	**119**	**75**	**58**	**24428**	**7.0**	**11**	**30**	**29**	**39**	**3.9**	**493**	**29**	**14**	**0.00**	**987**	**0.81**	**0.19**	**9.2**	**446**	**1.2**	**180**	**5.1**	**0.31**	**509**	**304**	**0.89**	**3.9**
Min	**81**	**303**	**15**	**13**	**61446**	**7.6**	**15**	**128**	**31**	**5.1**	**4.3**	**4934**	**186**	**0.16**	**599400**	**5985**	**1.6**	**0.07**	**3.1**	**4116**	**6.3**	**479**	**6.6**	**0.29**	**3632**	**1663**	**6.4**	**2.0**
Max	**11838**	**793**	**252**	**246**	**144974**	**33**	**55**	**258**	**159**	**149**	**18**	**6890**	**295**	**51**	**599400**	**10175**	**4.2**	**0.66**	**29**	**5683**	**11**	**1037**	**23**	**1.4**	**5676**	**2772**	**10**	**13**